AD-772 103

CORRELATION OF MICROSTRUCTURES WITH FRACTURE TOUGHNESS
PROPERTIES IN METALS

LOCKHEED MISSILES AND SPACE COMPANY, INCORPORATED

PREPARED FOR
NAVAL AIR SYSTEMS COMMAND

SEPTEMBER 1973

SECURITY CLASSIFICATION OF THIS PAGE (When Data Entered)

REPORT DOCUMENTATION PAGE		READ INSTRUCTIONS BEFORE COMPLETING FORM
1. REPORT NUMBER	2. GOVT ACCESSION NO	3. RECIPIENT'S CATALOG NUMBER
4. TITLE (and Subtitle) CORRELATION OF MICROSTRUCTURES WITH FRACTURE TOUGHNESS PROPERTIES IN METALS		5. TYPE OF REPORT & PERIOD COVERED Final Report 1 Jun 1972 – 30 Sep 1973
		6. PERFORMING ORG. REPORT NUMBER LMSC-D356114
7. AUTHOR(s) Frank A. Crossley Richard E. Lewis		8. CONTRACT OR GRANT NUMBER(s) N00019-72-C-0545
9. PERFORMING ORGANIZATION NAME AND ADDRESS Lockheed Missiles & Space Co., Inc. 3251 Hanover St., Palo Alto, Ca. 94304		10. PROGRAM ELEMENT, PROJECT, TASK AREA & WORK UNIT NUMBERS
11. CONTROLLING OFFICE NAME AND ADDRESS Naval Air Systems Command Department of the Navy		12. REPORT DATE September 1973
		13. NUMBER OF PAGES 133
14. MONITORING AGENCY NAME & ADDRESS(if different from Controlling Office)		15. SECURITY CLASS (of this report) Unclassified
		15a. DECLASSIFICATION DOWNGRADING SCHEDULE

16. DISTRIBUTION STATEMENT (of this Report)

Approved for public release; distribution unlimited

17. DISTRIBUTION STATEMENT (of the abstract entered in Block 20, if different from Report)

18. SUPPLEMENTARY NOTES

19. KEY WORDS (Continue on reverse side if necessary and identify by block number)

Titanium alloy	Microstructures of Ti-6Al-4V
Ti-6Al-4V	Crack growth rate
Fracture toughness	Mechanical properties

20. ABSTRACT (Continue on reverse side if necessary and identify by block number)
Ti-6Al-4V alloy was studied in three mill product forms for the purpose of establishing a correlation between microstructures and fracture toughness. The mill products were: 1- and 2.4-in. plates and 4 × 4-in. forged billets. Mill product, processing and heat treatment variables produced 28 microstructural conditions. Tension test, fracture toughness, and crack growth rate properties were determined. Light

DD FORM 1473 EDITION OF 1 NOV 65 IS OBSOLETE

Unclassified   130

microscopy, scanning electron microfractography, and transmission electron microscopy were the metallographic means employed.

A key factor in the microstructural and fracture toughness differences is cooling rate. Annealing high in the α-β phase field followed by air cooling results in high fracture toughness, associated with partially acicular structures, when applied to a volume of 50 cu in. (i.e., a $1 \times 4 \times 12$-in. piece); but results in relatively low fracture toughness, associated with an equiaxed structure, when applied to a volume of 5000 cu in. (i.e., a $1 \times 48 \times 96$-in. plate).

The fatigue crack propagation rate was found to vary widely among the different microstructures. For example, at a stress intensity range of 30 ksi-in$^{1/2}$, the crack propagation rate was 3×10^{-6} in/cycle for as-quenched martensite, 3×10^{-5} to 10^{-4} in/cycle for coarse equiaxed α, and 3×10^{-5} to 8×10^{-4} in/cycle for Widmanstätten, fine equiaxed α or worked Widmanstätten structures.

There was some correlation between microfractographic modes and fracture toughness. All conditions exhibiting low toughness had at least 5 to 10 pct quasi-cleavage present; this quasi-cleavage appears to occur in equiaxed α All conditions exhibiting high toughness were free of any cleavage. Also, all conditions containing coarse acicular α exhibited high fracture toughness associated with large (over 20 μm diameter or width) void cavities.

PREFACE

This report is an account of the work performed at the Lockheed Palo Alto Research Laboratory on the Correlation of Microstructure with Fracture Toughness Properties in Metals for the U.S. Naval Air Systems Command, Contract N00019-72-C-0545, from 1 June 1972 to 30 September 1973. The work was performed in the Metallurgy and Composites Laboratory, managed by Dr. T. E. Tietz. The co-investigators were Dr. F. A. Crossley and Mr. R. E. Lewis, assisted by A. T. Davinroy, R. W. Lindberg, A. R. Hansen, and A. S. Gleason. The project monitor was Mr. Theodore Highberger, Code Air – 52031D, Naval Air Systems Command, Washington, D.C.

CONTENTS

PRECE

TABLES

ILLUSTRATIONS

x

1.0 INTRODUCTION

1.1 DEFINITION OF THE PROBLEM

High performance naval aircraft use a variety of metallic materials, in both tension-critical and compression-critical structures. Particularly in tension-critical applications, the materials are used at a large fraction of their yield strength. Such structures periodically incur premature failure, usually by growth to critical size of a subcritical crack originating from an incipient flaw or a fatigue-induced crack. The fracture of key structural components often results in catastrophic loss of the aircraft and sometimes the crew.

Analyses of these failures usually discloses one or more of the following conditions: (1) the service loads (including fatigue) were higher than predicted; (2) an undetected incipient flaw was present that acted as a primary site of fracture origin; (3) the microstructure was lower in subcritical crack growth resistance and/or fracture toughness K_{Ic} than assumed.

The first discrepancy is solved when the service conditions are accurately identified and an appropriate stress analysis is performed for the subject parts. The development of computerized finite element and finite difference techniques, employing nonlinear elastic-plastic analyses, is greatly alleviating this problem.

The second discrepancy is solved if appropriate materials processing conditions and nondestructive inspection (NDI) techniques are developed. Many improvements continue to be needed in NDI, especially as higher strength materials are used at higher stresses and more severe environmental conditions.

The third discrepancy is possibly the most commonly incurred and least understood. Wide variations in microstructure occur in complex-shape, heavy-section forgings and

and fabricated components. Typical examples are wing pivots, wing box support structures, and other primary loaded structures in high-performance aircraft.

Fracture and fatigue behavior of high-strength titanium alloys, steels, and aluminum alloys used in these aircraft are influenced by variations of "normal" microstructural features, as well as the presence of abnormal features. For example, grain size and solute distribution can affect fracture behavior in all high-strength materials. In a multiphase alloy, the type, amount, and morphology of one or more phases typically affect fracture behavior. Abnormal features may include the presence of an embrittling element (such as excessive hydrogen in steel) or an embrittling compound, e.g., (Ti_3Al in titanium alloys) which occurs as such small particles that they are discernible only by transmission electron microscopy. Much research is needed to relate inherent and abnormal microstructural features to fracture behavior for these complex components that do not lend themselves to direct evaluation by laboratory or engineering tests. It is a valid goal to develop useful corrleations between microstructures and fracture toughness parameters so that more comprehensive analyses can be performed for predicting the useful service life of various highly stressed structures in high-performance aircraft.

1.2 CONSIDERATIONS FOR MATERIAL SELECTION

The superiority of titanium-base alloys in strength-to-density ratio and their resistance to heat at moderately elevated temperatures has earned them preference as construction materials for supersonic airciaft of Mach 3 or greater speed. However, it is not only in supersonic aircraft that titanium can be used to advantage for airframes. The use of titanium will increase with the trend to larger commercial aircraft. The longer sections and spars of the larger aircraft have rigidity requirements beyond the capacity of aluminum alloys. Titanium alloys with elastic modulus values 40 to 80 pct higher than aluminum alloys and possessing increased strength and corrosion resistance represent optimum materials for airframe construction. The C5 A military transport, the world's largest airplane, has 12,000 lb of titanium in the airframe, including titanium

2

fasteners. Lockheed's L-1011 air bus has more titanium than the C5 A in terms of absolute weight of titanium and as a percentage of the total structural weight of the airframe. The Boeing 747 has four through-wing spars that are 20 ft long by up to 11 in. in thickness. Each spar is produced from a 4000-lb Ti-6Al-4V forging to a finished wieght of 1700 lb. New figher aircraft such as the Navy F-14 and the Air Force F-15 will have airframes of 15 to 20 pct titanium. On the basis of the structural advantages of titanium alloys, it is reasonable to expect that they will be used in increasing amounts in commercial and military airframes. Furthermore, it is certain the alloy development and fabrication development efforts will lower the costs of installed titanium. As the cost of installed titanium goes down, its use will increase at a greater than linear rate.

In the last decade we have learned that structural design criteria are different depending upon whether the stress state of the structural element is described as plane stress or plane strain. In the former case, plastic instability is the mode of failure and the traditional method of designing at a fraction of yield strength is valid. However, in the latter case, catastrophic crack propagation under an elastic stress state is the failure mode. In the plane strain case, all materials are considered to contain flaws either inherent or as a result of processing which under certain conditions of loading provide sites for crack initiation. The cracks experience a period of slow (i.e., stable) growth until they reach a critical size, at which point they become unstable and propagate catastrophically to failure. Under these conditions a useful parameter to consider is the square of the ratio of plane strain fracture toughness to the yield strength $(K_{Ic}/F_{ty})^2$ for this quantity is proportional to the critical crack size. The ideal structural material for applications involving plane strain conditions has a critical crack size sufficiently large that it can be readily detected by nondestructive testing techniques.

In the plane strain regime, increasing the yield strength of the material is counterproductive if by such change the fracture toughness-to-yield strength ratio is decreased. Maximum structural efficiency results when the material is heat-treated to a yield

strength such that the probability of failure by plastic instability is equal to the probability of failure by brittle crack propagation. The applied stress is then set just below that which produces the stress intensity given by the plane strain fracture toughness index. Figure 1 shows yield strength-to-density ratio versus the critical crack size criterion $(K_{Ic}/F_{fy})^2$ for several high-strength, high-toughness steels and some titanium alloys.

It is clear that for a given flaw size (ordinate) titanium alloys offer greater structural efficiency (abscissa) than do steels. A further consideration is the susceptibility of the material to slow crack growth at lower stress intensity levels in the presence of water or sea water, i.e., threshold fracture toughness, K_{Iscc}, rather than plane strain fracture toughness, K_{Ic}. With the exception of the newly developed 10-Ni-2Cr-1 Mo-8Co-0.1C steel,* steels are notoriously susceptible to this type of stress corrosion while titanium alloys show variable susceptibility depending upon alloy composition and processing and thermal history. Titanium alloys show marked superiority over steels when the environmental influences of sea water are taken into consideration as demonstrated by Fig. 2.

It is desirable that critical parts, the failure of which would result in loss of the aircraft, be designed "fail-safe." That is, the flaw size associated with failure is sufficiently large that the probability that it would escape detection is negligible. If performance specifications dó not permit this degree of design conservatism, then it is prudent to use the material providing the largest critical flaw size for a given structural efficiency index. These considerations lead to the selection of titanium alloys over steels for use in aircraft structures involving heavy sections.

The titanium alloys shown in Figs. 1 and 2 are Ti-6Al-4V, the "workhorse" of the industry: Ti-6Al-6V-2Sn, the candidate replacement for Ti-6Al-4V when higher hardenability is desired; Beta III (Ti-11.5Mo-4.5Sn-6Zr), the new metastable beta' alloy; and Transage 129 (Ti-2Al-11.5V-2Sn-11Zr), a new type of martensitic titanium

---

*All alloy compositions and all additions to alloys are expressed in wt pct.

alloy developed at LMSC (1-3) having exceptional promise for applications across-the-board in airframes in the near future.

While Ti-6Al-4V alloy has been applied in aircraft for some 15 years, its use has been predominantly in engines where plane strain conditions do not generally apply. This may explain why there is a paucity of valid plane strain fracture toughness data on this, the most used titanium alloy. Data on the stress intensity required for slow crack growth in the presence of sea water are even more rare. There has been no systematic study of the relationship of microstructure to plane-strain fracture toughness involving Ti-6Al-4V. In general, it is recognized that the Widmanstätten structure is superior in plane-strain fracture toughness to the equiaxed structure. Beta-forged compressor wheels have been reported to have 40 to 70 pct higher fracture toughness (K_Q) than α-β-forged wheels.[4]

Resistance to slow crack growth under plane strain conditions and notched bar resistance to high cycle fatigue would appear to be related in similarity of microstructural dependance. That is, structures which produce relatively higher notched fatigue strength at 10^6 to 10^7 cycles are associated with relatively higher plane strain fracture toughness. In this regard it is interesting to note that β-forged Ti-6Al-4V was found to have the same fatigue strength at 10^7 cycles for $K_t = 3.0$ and $R = +0.1$ as α-β-forged Ti-6Al-4V. Beta forging results in worked Widmanstätten structures compared with equiaxed structures produced by α-β forging. However, castings of Ti-6Al-4V, representing as-transformed Widmanstätten structure, were found to have 80 pct higher fatigue strength under these conditions compared with equiaxed sheet and plate products, and twice the fatigue strength of β-forged material representing worked Widmanstätten structures at 10^6 cycles.[5] Comparisons between β-worked and α-β-worked Ti-6Al-4V alloy may appear contradictory. However, it may be noted that β-worked material can vary in microstructural appearance to closely approximate as-transformed Widmanstätten at one extreme to equiaxed α-β at the other. Besides being of interest because it occurs in castings, as-transformed Widmanstätten is also of interest because of its occurrence in weldments, in weld heat-affected zones, and as a processing defect due to overheating into the β-phase field.

Somewhat related to as-transformed Widmanstätten structures is martensite formed by very rapid cooling (e.g, water quenching sections of 1 in. or less) from the β-phase field. Van Orden and Soffa reported electron beam weldments in Ti-6Al-4V to have a 10^7 cycle fatigue strength of 44 ksi for $K_t = 3.0$ and $R = 0.1$, compared to 26 ksi for β-forged materials and 20 ksi for α-β-forged material.[6] This is a spectacular 41 pct increase in notched fatigue strength for the EB weldment compared to β-worked material. The structure of the EB weldment was martensite. It should be noted that martensite is the only microstructure possible in Ti-6Al-4V alloy that is not charac-terized by a linear interface between α and β assuming 100 pct transformation. Martensite needles, i.e., alpha, end at prior β grain boundaries, while α formed by nucleation and growth processes forms preferentially in prior β grain boundaries. More will be said about this below in the discussion of the work of Greenfield and Margolin.[7] The exceptionally high fatigue strength of the martensitic structure dic-tates that it should be evaluated for its own sake as well as for its occurrence in EB weldments.

Ti-6Al-4V alloy was selected as the material for investigation because it continues to be the most used titanium alloy. Valid plane-strain fracture toughness data are needed to ensure reliability of the new aircraft now in development such as the F-14, the F-15, and the B-1 Air Force bomber. A definition of the relationship between microstructure and plane-strain fracture toughness is urgently needed because of the wide variety of microstructures that are possible in Ti-6Al-4V considering heat-treated extrusions, forgings, plate, weldments, and castings. Furthermore, Ti-6Al-4V is an ideal model alloy because of its relative simplicity of composition and the fact that the stronger and deeper hardening α-β alloys are simply more complex analogies of it. Finally, of all titanium alloys now in production, it has the least problems with macroscopic and microscopic segregation upon melting and solidification and for this reason is much favored among users.

1.3 THEORETICAL CONSIDERATIONS

The only published study relating microstructural features to fracture toughness in titanium alloys is the work of Greenfield and Margolin.[7] The study included

6

equiaxed and Widmanstätten microstructures of the alloy Ti-5.25Al-5.5V-0.9Fe-0.5Cu for a common STA condition. Equiaxed sturctures were found to follow the relationship

$$K_Q = 43 + 400/D \tag{1}$$

where K_Q is the calculated fracture toughness index (ksi-in$^{1/2}$), and D is the β grain diameter (μm). At the solution treatment temperature, the β:α ratio was approximately 1:1. Widmanstätten structures were found to have higher fracture toughness for the same strength level (and, incidentally, lower tensile ductility) than equiaxed structures. The relationship for Widmanstätten structures was found to be

$$K_Q = 43 + 400/D + 10.5(\ell - 2.6) \quad ; \quad 2.6 < \ell \leq 5.5 \tag{2}$$

where K_Q and D are as defined above and ℓ is the width of the continuous α in the β grain boundaries. It may be noted that this grain boundary α makes a contribution to fracture toughness provided it is at least 2.6 μm thick. The importance of the grain goundary α lies in the fact that fracture is intergranular and the crack propagates along the interface between α and β. Solution-treated and aged Ti-6Al-4V apparently always, or nearly always, has α in the β grain boundaries; for β/β boundaries existing after solution treatment will develop α precipitates during aging. Apparently, when such α particles surpass the 2.6 μm thickness, they increase the crack tip critical plastic zone size and thereby enhance resistance to crack propagation. In this regard martensitic structures are of special interest because the prior β grain boundaries of fully martensitic structures contain no continous films of α. For this reason, martensitic structures are included in the present study.

The finding of Greenfield and Margolin that Widmanstätten structures have superior fracture toughness to equiaxed structures in spite of having significantly lower tensile ductility contradicts the model proposed by Hahn and Rosenfield, [8]

$$K_{Ic} \approx \sqrt{\frac{2}{3} E \cdot F_{ty} \, \bar{\epsilon}^* \, n^2} \tag{3}$$

7

where E is the elastic modulus, F_{ty} is the tensile yield strength, $\bar{\epsilon}^*$ is the critical true strain for coalescing voids which Hahn and Rosenfield propose is approximately the true strain at fracture $(\ln a_o/a_f)$ displayed by a uniaxial tensile specimen, and n is the strain hardening exponent. Greenfield and Margolin observed that their fracture toughness specimens did not fail by void coalescence, and therefore their findings do not challenge the above model, for that model should apparently be applied only in cases where the observed microfractographic mode of plane strain fracture is by void coalescence.

1.4 DEFECTS

1.4.1 Inherent Defects

The only continuing inherent defects occurring in Ti-6A1-4V alloy to the authors' knowledge are void-associated alpha stabilized inclusions and alpha segregation. Both defects are relatively uncommon. The void-associated alpha stabilized defects are macroscopic in size. A very recent paper by Henry, et al. attributes these defects to contamination of magnesium-reduced titanium sponge by air leaks during the distillation cycle or to the use of air-contaminated magnesium.[9] The effect of this defect on strength can be estimated by fracture mechanics assuming a critical incipient flaw the size of the defect. The second type of inherent defect, alpha segregation, is a general microstructural condition which manifests itself as massive areas of α, sometimes many times larger than the grain size of the (usually) equiaxed α-β matrix. As defined herein, alpha segregation is not that which occurs as a result of ingot segregation during solidification in the pipe region (a problem that has been cured by special melting practice applied to the last metal to solidify). Rather, it is segregation which results from hot working practice, and is also called, "stringy alpha." It is caused by alpha nucleation and growth to such a large size under condition of slow cooling through the beta transus temperature that it is very difficult to eliminate in subsequent hot working operatings. The defect is a valid area of concern; therefore, it is included in the current investigation.

8

1.4.2 Processing Defects

The Ti-6Al binary alloy becomes saturated with respect to aluminum at about 1185°F, and at 900°F the solubility of aluminum in titanium is reduced to 4 pct. [10] In binary Ti-Al alloys, the occurrence of Ti_3Al is associated with loss of tensile ductility and of impact resistance. [11] However, in ternary alloys containing an isomorphous β-stabilizer such as Cb, Mo, Ta, or V, the effects of the Ti_3Al precipitation reaction are more complex. The isomorphous β-stabilizers appear to make the Ti_3Al precipitation reaction more sluggish, and to suppress its precipitation at grain boundaries. There appears to be a morphology and/or distribution of Ti_3Al which enhances impact resistance. Crossley reported the Ti-7Al-3Cb alloy to exhibit this phenomenon to an exceptional degree. [12] Alpha alloys containing oxygen at the level of 0.08 wt pct aged at 1200°F (i.e., the approximate position of the nose of TTT curves for Ti_3Al formation) for 10 hours exhibited Charpy V-notch impact energy at -80°F as follows:

Alloy	Atomic Pct Solutes	Charpy at -80°F (ft-lb)
Ti-7Al	12	44
Ti-8Al	13.5	10
Ti-7Al-3Cb	13.5	83

There appears to be a similar effect of Ti_3Al morphology and/or distribution on fracture toughness. This is demonstrated below by data for 1/2-in. plates taken from Piper, et al. [13]

Alloy	F_{tu}(ksi)	K_Q(ksi-in$^{1/2}$)	K_{Qscc}(ksi-in$^{1/2}$)
		Mill Annealed	
Ti-6Al-4V	133	83	38
Ti-8Al-Mo-1V	150	44	21
		Duplex Annealed	
Ti-6Al-4V	131	71	57
Ti-8Al-1Mo-1V	140	100	28

The specifics of the annealing treatments were not reported; however, the mill anneal conventionally involves furnace cooling from 1350° or 1450°F to 1050°F or lower temperature. That is, mill annealed alloys are slowly cooled through the temperature range of maximum rate of Ti_3Al formation. The duplex anneal consists of following the mill anneal with reheating to a temperature of 1450°F, or higher temperature but below the β transus, and air cooling. The duplex anneal was developed for alpha-beta alloys containing 6 pct or more aluminum in order to improve their resistance to stress corrosion. The duplex anneal reduces the extent to which the Ti_3Al precipitation reaction has progressed compared to the mill annealed condition. Note that Ti-6Al-4V has higher fracture toughness in the mill anealed condition but lower stress corrosion threshold. On the other hand, Ti-8Al-1Mo-1V has better fracture toughness and better stress corrosion threshold in the duplex annealed condition. Considering duplex annealed conditions, Ti-8Al-1Mo-1V is superior in fracture toughness to Ti-6Al-4V, but its stress corrosion threshold is only one-half as high.

These observations present a quandary. When exceptionally high fracture toughness is observed in an alloy such as Ti-6Al-4V, is it due to Ti_3Al? If so, then we may be required to pay a price in resistance to stress corrosion, that is, K_{Iscc}. Furthermore, at present it appears that determination of the threshold fracture toughness in the presence of sea water, or a salt solution approximating sea water, is the only means of determining if the high K_{Ic} is at the expense of K_{Iscc}. Processing schedules that maximize the extent of Ti_3Al precipitation may be considered undesirable, and the resulting precipitate a defect.

The most common processing defects are oxygen and hydrogen contamination. Oxygen contamination most frequently is the result of insufficient removal of contaminated surfaces from hot worked parts or parts or parts heat-treated in air, or castings made in an oxide coated mold. Hydrogen contamination may result from improper pickling, and from heat-treating in a reducing atmosphere. Both interstitial impurities are known to degrade fracture toughness. Overheating into the β-phase field so

10

that an unworked or as-transformed Widmanstätten structure results (and is not desired) is a processing defect which may result in the parts being scrapped.

Occurrence of Ti_3Al and hydrogen and oxygen contamination are not included in the investigation reported herein, but are candidates for an extension to the current study.

2.0 MATERIALS AND METHODS

2.1 MATERIALS, PROCESSING, AND HEAT TREATMENT

The two major titanium producers, Titanium Metals Corporation of America (TMCA) and Reactive Metals, Incorporated (RMI), were surveyed to determine the characteristics of the Ti-6Al-4V plate stocks they are currently producing. Reactive Metals is producing Ti-6Al-4V plate for the F-14 and F-15 systems. The plates are of standard grade Ti-6Al-4V with a 0.2 pct oxygen maximum and have equiaxed microstructure. Plates thicknesses being produced are 5/8 and 3/4 in. Ti-6Al-4V plate intended for use in the B-1 is of the ELI (extra low interstitials) grade with a 0.13 pct oxygen maximum. Such plate is required to meet fracture toughness and microstructural specifications in addition to the usual tension test specifications applicable to the standard grade. The specifications require a minimum K_{Ic} of 70 ksi-in$^{1/2}$ (75 ksi-in$^{1/2}$ desired), and that the plates have sufficient stored energy that they recrystallize to an equiaxed microstructure when subjected to a simulated diffusion bonding heat treatment cycle, which involves heating to 1750°F. Plate of greater thickness than one-inch for the B-1 program is supplied by TMCA, while Ti-6Al-4V plate for the F-14 program is supplied solely by RMI.

Since plate for the B-1 program is being purchased to a fracture toughness specification, such plate is being well characterized with respect to this property. Also, because of the microstructural specifications and the diffusion bonding joining process, microstructural control is, in all likelihood, considerably greater than for mill production and user frabrication of the standard grade plate being used in the F-14 and F-15 systems. Therefore, it was considered that the current program would provide the greater service by selecting plate being supplied for the F-14 and F-15 programs as the primary basis of the investigation.

The form, source, and chemistry of the Ti-6Al-4V materials of the current investigation are summarized in Table I. The 1-in. plate was specified to have a microstructure approximating as closely as possible that of 3/4-in. Ti-6Al-4V plate supplied for the F-14. (It may be noted that 3/4-in. is the thickest plate supplied for the F-14; however, 1-in. is needed to satisfy plane strain requirements for the level of fracture toughness anticipated.) The 2.4-in. plate was cut from a plate supplied for the Rockwell International B-1 program.

The processing schedule to produce the 4×4-in. forged billets is given in Fig. 3. The billet processed to produce the α-segregated, worked Widmanstätten microstructure was not evaluated during the current investigation; it will be included in an extension of this work.

The heat treatment applied to produce the various microstructural conditions of this investigation are given in Table II. The given heat treatment was applied to a single piece of alloy of sufficient size that all of the required test specimens could be machined from it, with the exception of conditions requiring an iced brine quench from the β-phase field in order to simulate the rapid cooling of an electron beam weld in a heavy section. In this case, individual specimen blanks were cut before heat treatment; however, all blanks for a given condition were heat-treated simultaneously. These procedures were followed to ensure that all test specimens and metallographic samples representing a given condition experienced an identical thermal history; and to approximate as closely as possible production practice which would necessarily involve the heat treatment of large volumes of metal.

2.2 MECHANICAL PROPERTIES TESTS

Tensile Properties

The tensile properties — ultimate strength, 0.2 pct offset yield strength, percent elongation at fracture, and percent reduction in area — were determined in accordance with the requirements of the applicable ASTM standards. The tensile test specimen

13

configuration is shown in Fig. 4. Specimen orientation was long transverse in the plate and transverse in the billet materials. One test was conducted for each of the 28 microstructural conditions. Loads were applied with a Tinius Olsen multirange 120,000-lb. capacity hydraulic testing machine. The accuracy of this machine meets or exceeds the accepted ASTM standard of 1 pct of indicated load. The specimens were loaded at a strain rate of 0.005 in/in/min to yield then increased to approximately 0.020 in/in/min to fracture. Strains were measured with an ASTM class B-1, LVDT extensometer. Individual load-elongation curves were autographically recorded for each specimen tested. These records were used to obtain the load at 0.2 pct offset strain and ultimate load for calculation of yield and ultimate strengths, respectively.

The percent elongation was computed from the measured change in separation between two gage marks preplaced one inch apart along the specimen length. The two pieces of the tested specimen were removed from the test assembly and fitted together to make this measurement. The percent reduction in area was computed from measurements of the cross-sectional diameter at the necked-down region compared with the original diameter at the same locus.

Fatigue Crack Growth and Fracture Toughness Properties

For each heat treatment condition two specimens of the same configuration were employed for evaluating fatigue crack growth rate behavior $(da/dN$ vs $\Delta K)$. One of these specimens was also used to obtain a value of the fracture toughness index, K_{Ic} or K_Q. The specimen configuration selected was the compact tension (CT) type shown in Fig. 5. This specimen type has the advantage of requiring the smallest volume of material to obtain plane-strain conditions and also is covered by an appropriate ASTM specification.[14] Orientation of each specimen was TL, i.e., the crack plane normal to the long transverse direction in the plate or transverse in the billet, and crack growth direction parallel to the longitudinal or rolling direction.

In each specimen, the starter notch was sharpened to fatigue crack acuity by low stress tension-tension sinusoidal loading. The maximum load in pre-cracking was closely

14

controlled, so that the plastic zone produced at the crack tip did not interfere with subsequent da/dN determinations. The pre-crack length was nominally 0.75 in. (a/W = 0.3).

The pair of specimens for each heat treatment condition was tested in the following way. The first specimen was loaded sinusoidally in tension-tension at a frequency of 10 to 16 Hz, and a minimum to maximum load ratio of 0.1 (i.e., R = 0.1). The cyclic load was adjusted to provide crack growth rate data in the range of 10^{-5} to 10^{-3} in. per cycle. The load range was periodically adjusted upwards as the crack extended to obtain incremental ranges of crack growth data. The crack length was monitored by an ultrasonic transducer positioned on the top of the test specimen (Fig. 6) so that the ultrasonic beam reflection from the crack front at mid-thickness and the bottom surface of the specimen could be compared electronically. The difference in amplitude between these two reflections was used to generate an error signal used to drive a gear head motor which repositioned the transducer to reduce the error signal to zero. The position of the ultrasonic transducer was independently monitored by a linear variable differential transducer (LVDT), the output of which provided a numerical value of crack length. The cycle count was obtained from a digital ramp function generator, calibrated for the sinusoidal load frequency applied to the specimen by a closed loop, electrohydraulic fatigue unit. An X-Y plotter was used to make an autographic record of crack length (ordinate) versus cycles (abscissa). Data were obtained in this manner to the maximum extent of useful subcritical crack length of the specimen, approximately 1.73 in.

The second specimen was used to obtain fatigue crack growth rate data in the same manner as the first specimen, but with two differences. One difference was that the cyclic load was adjusted to provide crack growth rate data in the range of 10^{-6} to 10^{-5} in. per cycle. The other difference was the fatigue crack length was extended to between 1.13 and 1.36 in. (0.45 ≤ a/W ≤ 0.55). Thus, the second specimen provided complementary data to the first specimen, and the final fatigue crack length was in the appropriate range for subsequent testing to obtain a fracture toughness value, K_{Ic} or K_Q.

15

After fatigue testing, the second specimen was removed from the axial fatigue unit, and a crack opening displacement (COD) gage was affixed. This specimen was then loaded to failure to obtain a valid plane-strain fracture toughness index, according to ASTM Standard E 399-72. During this test, load (ordinate) vs. COD (abscissa) was autographically recorded. The conditional stress intensity factor (K_Q) was then calculated from the equation:

$$K_Q = C P_Q/Ba^{1/2}$$

where C is a function of the dimensionless ratio of the crack length to specimen length, P_Q is the conditional value of the critical load as defined in the ASTM specification, B is the specimen thickness and a is the average crack length from the load line. The function, C, is expressed in polynomial from[15] as:

$$C = 30.96(a/W) - 195.8(a/W)^2 + 730.6(a/W)^3$$
$$- 1186.3(a/W)^4 + 754.6(a/W)^5$$

where W is the specimen length measured from the load line.

When the K_Q value was obtained, it was then determined whether K_Q equals a valid K_{Ic}. Two major tests and a number of minor tests are applied to make this determination. The major tests are $1.00 \leq P_{max}/P_Q \leq 1.10$ and B, a, W-a, and H $\geq 2.5(K_Q/F_{ty})^2$, where P_{max} is the maximum load obtained in the test, and H is the height of the specimen from the crack plane. The minor tests involve rate of loading, crack shape, and a number of other factors detailed in the ASTM specification.

2.3 METALLOGRAPHY AND FRACTOGRAPHY

Metallography

Metallographic samples were prepared for light microscopy by mechanical polishing.
Polished samples were etched by immersion in a 10 vol. pct solution of 49 vol. pct
concentrated fluoboric acid (HBF_4) for a time of 1.5 to 2 minutes. Thin-foil electron
transmission studies were done with a Siemens Elmiskop 1A-125 kV electron micro-
scope equipped with a universal specimen stage with a double tilt. Samples were cut
from bulk material to the dimensions: 2.3 mm diameter × 1/4 to 1/2 mm thick.
Cutting means were carbide abrasive wheel and jewelers saw. A Fischione twin jet
electropolisher was used for thinning the disc specimens. Polishing was automatically
stopped when a hole formed in the center of the sample. The electrolyte was 40 ml
methyl alcohol, 20 ml H_2SO_4, 60 g $AlCl_3$, and 20 g $ZnCl_2$. Polishing conditions were:
15 V, 10−20 mA, and bath temperature of 23°F. The foils were rinsed in ethyl alcohol
upon removal from the bath.

Fractography

Fracture surfaces of each K_{Ic} test specimen were cleaned by immersing one-half
of a full specimen in acetone at room temperature for 5 to 15 minutes in a low-power
ultrasonic bath. Each specimen half was inserted intact into the chamber of the
Cambridge Steroscan II Scanning Electron Microscope (SEM). The angle between
the incident electron beam and collector tube is 90 degrees; the angle between the
(normal to the) specimen fracture surface and incident electron beam was 10 to 30
degrees, inclined toward the collector. An accelerating voltage of 10 kV was em-
ployed. Two areas at mid-thickness on each fracture surface were documented at
1200 ± 200 magnifications. One area was a fatigue region 4 mm before the onset of
rapid crack propagation, where the macroscopic crack growth is nominally 10^{-5} to
10^{-4} in. per cycle. The other area was in the elastically unstable (fast fracture)
crack growth region, 2 mm beyond the fatigue crack region.

The hardness of each microstructural condition was obtained by averaging ten or more Rockwell "C" readings obtained on both sides of one fracture toughness specimen. These readings were taken at approximately 5-mm intervals in a line parallel to the crack plane and 2–3 mm from the crack plane.

3.0 RESULTS AND DISCUSSION

3.1 TENSILE PROPERTIES

The tensile properties for the twenty-eight product-heat-treatment conditions are given in Table III. These data provide a useful baseline characterization of both strength and large volume plastic deformation capacity (elongation, reduction of area). The properties are grouped according to product and subgrouped according to type microstructure. Within each type microstructure, they are grouped according to type of heat treatment. The fracture toughness properties, hardness, Young's Modulus, and some other calculated values (calculated plastic zone size, r_p, and flaw size surviving a particular proof test; a_i) are also contained in this table and will be discussed later.

The individual tensile properties within a particular product − structure − heat-treatment type (P-S-HTT) combination do not vary much about the average values within that set. This is particularly true for yield and ultimate tensile strength. Elongation and reduction of area (RA) vary little within a P-S-HTT set except for the 1-in. Widmanstätten plate, solution heat-treated and aged (Conditions 10, 11, 12, and 14); these vary from 5 to 18 pct RA. Condition 14 in this set does not have a valid elongation measurement as the specimen broke outside of the gage section. The implication of this combined with the low (5 pct) RA would lead one to expect this microstructural condition to exhibit a low fracture toughness. As can be seen in Table III, K_{Ic} for Condition 14 is 71 ksi-in$^{1/2}$, contrary to expectations. The significance of acicular microstructure (a characteristic of Condition 14, see Fig. 22) to high fracture toughness is discussed in detail later.

No particular relation between yield strength and elongation or RA was found even within a particular P-S-HTT set. Thus, each microstructural condition has a unique

19

set of tensile properties which is similar only to other conditions within the same P-S-HTT set.

3.2 FRACTURE TOUGHNESS PROPERTIES

The fracture toughness index, K_{Ic} (or in some cases, K_Q) was determined for each of the twenty-eight conditions. K_Q is used to designate toughness when a major test of validity for K_{Ic} is not met. The fracture toughness test for some conditions resulted in some other minor violations of K_{Ic} validity according to ASTM Specification E 399-72.[14] The fracture toughness index, K_{Ic} or K_Q, is presented in Table III, along with an indication of violations of the specification requirements. The violations noted in Table III and described in the ASTM Specification are presented in Table IV. Data obtained for each specimen is illustrated for Condition No. 1 in Fig. 7.

It is the authors' judgment that a conditional value of the fracture toughness index, K_Q, is essentially equal to a valid K_{Ic} if it meets the major tests for validity, and is listed as such in Table III. This interpretation is consistent with the practice prior to publication of the ASTM Specification. For example, the recently released Damage Tolerant Design Handbook incorporates this practice.[16]

A useful relation of fracture toughness between different microstructural conditions is the comparison of K_{Ic} and F_{ty}. Such a comparison is made in Fig. 8. Although the overall range of toughness is from 46.9 to 110.9 ksi-in$^{1/2}$ (Conditions 1 and 2), respectively, only Condition 2 exceeds 87.2 ksi-in$^{1/2}$. Test results for Conditions 2, 7, 8, and 13 failed to meet the size requirement; B, etc. $\geq 2.5\,(K_Q/F_{ty})^2$.

With the exception of Condition 2, the upper bound of toughness declines with increasing yield strength. This is a commonly observed generality for structural materials. For a particular level of yield strength such as 125 ± 5 ksi, there is a significant range in toughness from a low of 47.7 ksi-in$^{1/2}$ for Condition 15, as received, 2.4-in. thick plate to a high (K_Q) of 87.2 ksi-in$^{1/2}$ for Condition 13, 1-in. thick plate, annealed Widmanstätten structure. At higher levels of yield strength, the fracture toughness

range is narrower with the exception of Condition 2. Above a yield strength of 160 ksi, the fracture toughness range narrows to 48 ± 1 ksi-in$^{1/2}$. Only one type structure, fine equiaxed, 1-in. plate, developed a yield strength in excess of 160 ksi. It is interesting to note that over the entire range of yield strength from 120 to 160 ksi, the lower bound of toughness is constant, $47-48$ ksi-in$^{1/2}$. The three lowest fracture toughness values were for Conditions 15, 1, and 4, having yield strengths of 120, 144, and 164 ksi, respectively. Conditions 15 and 1 represent as-received (mill-annealed) conditions, while Condition 4 represents an STA condition. Condition 15 presumably represents material supplied for the Air Force B-1 bomber program. The purchase specification for such material requires a minimum toughness of 70 ksi-in$^{1/2}$ following a heat-treatment cycle consistent with diffusion bonding temperature-time parameters. The heat treatment for Condtion 16 (1775°F-1/2 h-AC, 1450°F-1 h-AC) simulates a diffusion bonding cycle. This heat treatment applied to the 2.4-in. plate produced a modest increase in yield strength from 121 to 134 ksi; but produced a significant improvement in fracture toughness from 47.7 to 79.9 ksi-in$^{1/2}$. The simulated diffusion bonding cycle applied to the as-received 1-in. plate produced even greater change in fracture toughness — compare Conditions 1 (as-received) and 2 (simulated diffusion bonding cycle) in Fig. 8. Published data for 1-1/4-in. mill-annealed plate of Ti-6Al-4V shows an average fracture toughness of 95.7 ksi-in$^{1/2}$ and yield strength of 119.4 ksi.[17] Although this strength compares favorably with the nominally equivalent Condition 1 of the present study, the fracture toughness is twice as high. The 1-1/4-in. plate is believed to have been heat-treated in the α-β phase field, as was the as-received 1-in. plate. A possible explanation for this discrepancy is presented later when microstructures are discussed.

Besides the fracture toughness index, two other related factors are presented in Table III. These are r_p, the calculated plastic zone size (radius) at onset of elastically unstable fracture, and a_i, the maximum size (depth) of a semicircular surface flaw surviving a proof test at a given stress. The numerical value of r_p has no engineering usefulness, but simply indicates the maximum size of the intensely deforming region immediately ahead of the crack tip. The maximum source of energy absorption in the crack propagation resistance (fracture toughness) of a metallic material

stressed in tension is the work involved in plastic deformation. A large critical plastic zone size indicates a high resistance to crack propagation. Computation of r_p is made from the equation for stress distribution normal to the crack plane at the crack tip[18]:

$$\sigma_y = K \sqrt{\frac{1}{2 \pi r}} \tag{4}$$

For plane strain conditions, Irwin[19] computes:

$$r = r_p = \frac{1}{4 \pi \sqrt{2}} \left(\frac{K_{Ic}}{F_{ty}}\right)^2 \approx \frac{1}{6 \pi} \left(\frac{K_{Ic}}{F_{ty}}\right)^2 \tag{5}$$

The maximum flaw size for survival of proof testing, a_i values in Table III were calculated for an applied tensile stress of 120 ksi for each material condition. For the semicircular surface flaw model:

$$a_i = \frac{Q}{1.2 \pi} \left(\frac{K_{Ic}}{\sigma}\right)^2 \tag{6}$$

where:

$$Q = 2.467 - 0.212 \left(\frac{\sigma}{F_{ty}}\right)^2$$

σ = applied stress, 120 ksi

F_{ty} = tensile yield strength

K_{Ic} = fracture toughness index

The magnitude of a_i is important with respect to the usefulness of nondestructive test (NDT) techniques other than the proof test. A range of 0.030 to 0.050 in. is the size often quoted as being reliably detectable by high quality X-ray, ultrasonic, eddy current, etc., techniques.[20,21] A proof stress of 120 ksi would not detect any flaws smaller

22

than 0.094 in. deep for Condition 1, or smaller than 0.524 in. for Condition 2. Thus, conventional NDT would establish a smaller initial flaw size than a proof test at 120 ksi stress. Establishment of an initial flaw size at least as small as the detectable limits of high-quality NDT is desirable in order to maximize the life of a structure in terms of subcritical crack growth. Application of a proof stress higher than 120 ksi could be applied beneficially only to those structures known to have a yield strength in excess of the proof stress. Because of the strong probability of not knowing the microstructural variation in some complex part, and the corresponding yield strength and toughness variations, a great risk is incurred by proof testing Ti-6Al-4V components at a stress higher than 120 ksi. Newer NDT techniques, for example, acoustic emission, offer promise of being able to establish a smaller initial crack size than proof testing, thus increasing reliability in terms of service life.

3.3 RELATIONSHIP OF MICROSTRUCTURES TO MECHANICAL PROPERTIES

Microstructures of the various conditions evaluated are shown in Figs. 9 through 37. For convenience in relating mechanical properties to structure, plane-strain fracture toughness and 0.2 pct offset yeild strength are given below the photomicrographs. Micrstructures of Conditions 1, 2, and 3, of the 1-in. plate are shown in Fig. 9, 10, and 11. Nominally, the heat treatments are similar. Condition 1 was solution heat-treated at $1725°F$ for 1 h and air-cooled; while Conditions 2 and 3 were solution heat-treated at $1775°F$ for 1/ h and $1750°F$ for 2 h, respectively, and air-cooled. All three conditions were given a final anneal of $1450°F$-1 h-AC. While there was no significant variation in yield strength for the three conditions, fracture toughness differed by more than a factor of two with the as-received Condition 1 having the lowest value, $K_{Ic} = 47$ ksi-in$^{1/2}$, and Condition 2 having the highest value of all 28 conditions, i.e., $K_Q = 111$ ksi-in$^{1/2}$. The absence of coarse acicular areas in the Condition 1 microstructure compared to Conditions 2 and 3 indicates that it cooled considerably more slowly from solution heat treatment than the other two. The grain size of Condition 1 is clearly smaller than Conditions 2 and 3 suggesting that the absence of acicular areas is a significant factor in the low fracture toughness associated with this condition.

23

Also, the inference of slower cooling raises the suspicion that perhaps the Ti_3Al pre-
cipitation reaction is more advanced for Condition 1 than in the other two. At 1450°F
the Ti-6Al-4V alloy is just inside the boundary of the $\alpha + \beta + Ti_3Al$ phase region[22]
suggesting that most of what Ti_3Al may have formed upon slow cooling from the solu-
tion heat treatment temperature would dissolve at 1450°F. However, if the as-received
Condition 1 were more slowly cooled from the final 1450°F anneal than Condtions 2 and
3, which seems likely because of the much larger volume of metal involved, then the
suspicion that Ti_3Al is more prevalent in Condition 1 is restored. It may be noted that
no evidence of Ti_3Al formation was observed in transmission electron microscopy
(TEM) of this material. The TEM results are discussed in greater detail later.

Conditions 4, 5, and 6 represent identical STA type heat treatments of the 1-in. plate
in the equiaxed condition differing only in the time of the solution heat treatment in
order to vary the size of primary α. Fracture toughness and yield strength for the
three conditions differ but little from the average values for the three of K_{Ic} = 49 ksi-
$in^{1/2}$ and F_{ty} = 162 ksi. The average grain diameter in the transverse direction of
the primary α grains is 3.2 μm for Condition 4 and 5.9 μm for Condition 5; while
there is no significant difference between Conditions 5 and 6. The findings of Greenfield
and Margolin[7] would have (indirectly) led one to expect Condition 4 to exhibit higher
fracture toughness than Conditions 5 and 6. We believe that the β grain diameter, D,
in Eq. 1 is a variable which is dependent upon the particle, or grain, size of the primary
α. Greenfield and Margolin employed a solution heat-treatment temperature of 1625°F
but measured β grain size after heating to 1675°F. Crossley contended that during
such heating, α dissolved and β grew proportionately in order to adjust the α/β
ratio – the driving force being the free energy to establish equilibrium between the two
phases.[23] Another way of stating this phenomenon is that during heating the α/β
boundaries migrate toward the center of the primary α grains terminating in an all
β structure when the $\beta/\alpha + \beta$ transus is reached. Employing the data of Greenfield
and Margolin, one obtains a relationship similar to Eq. 1 between K_Q and d, the
transverse dimension of the primary α, to wit:

$$K_Q = 45 + 83/d \tag{7}$$

where K_Q is expressed in ksi-in$^{1/2}$ and d in μm. However, scatter in the data is wide, particularly at smaller values of d. It may be noted that the grain diameters reported above for Conditions 4 and 5 are within the range of values measured by Greenfield and Margolin, but that the alloy of the Greenfield and Margolin study was Ti-5.25Al-5.5V-0.9Fe-0.5Cu. The difference in composition between this alloy and Ti-6Al-4V may mean differences in microconstituents after aging which may influence fracture toughness such as to account for the findings of Greenfield and Margolin as opposed to the findings of the current investigation.

Considering the Widmanstätten structures of Conditions 7, 8, and 9 shown in Figs. 15, 16, and 17, respectively, the microstructures of the three conditions are essentially the same. This similarity is reflected in the fact that there is no significant difference in fracture toughness and yield strength for the three conditions. Average values for the three conditions are: $K_Q = 84$ ksi-in$^{1/2}$ and $F_{ty} = 125$ ksi.

Considering the STA Widmanstätten microstructures of Conditions 10, 11, and 12, Eq. 2 (from the work of Greenfield and Margolin[7]) would lead one to expect Conditions 11 and 12 to exhibit higher fracture toughness than Condition 10. The basis of this expectation is that the grain boundary α of Condition 10 (which is 3 to 4 μm in transverse dimension) is finer than that of Conditions 11 and 12. However, this is not the case; the K_{Ic} value for Condition 10 is about 14 pct higher than those for Conditions 11 and 12.

Condition 13 of the 1-in. plate differs from Condition 8 only in that it was air-cooled from 1875°F to form the Widmanstätten structure compared to 1850°F for Condition 8. There is no apparent difference in their microstructures as shown in Figs. 16 and 21; however, Condition 13 had a larger β grain size as expected. No significant differences in fracture toughness and yield strength of the two conditions were observed. Tensile reduction of area of Condition 13 was 11 pct compared to 15 pct for Condition 8, perhaps reflecting the larger (β) grain size of the former.

Comparing STA conditions of Widmanstätten structures formed by cooling from 1875°F, Condition 14, and 1850°F, Condition 11, shows the former to have a 22 pct higher K_{Ic}

25

value, but less than 3 pct lower yield strength. The fact that the reduction of area was only 5 pct for Condition 14 compared to 18 pct for Condition 11 indicates that for relatively coarse, two-phase, lamellar microstructures, the plastic zone size is not controlling in fracture toughness as predicted by Eq. 3 (from the work of Hahn and Rosenfield[8]). It would appear that for these microstructures the constraints placed upon the fracture path by the lamellar spacing and orientation may be the controlling factors.

Martensitic structures produced in the 1-in. plate are shown in Figs. 23 through 26. Stress relief annealing 1450°F-1 h-AC lowered the fracture toughness about 15 ksi-in$^{1/2}$ compared to IBQ values. Values of K_{Ic} in both the as-quenched state and the annealed state were slightly higher for material quenched from 1875°F compared to material quenched from 1850°F. Small α particles 5 to 7 μm in diameter may be noted in Figs. 23 and 24 representing material quenched from 1850°F indicating that the β transus of this heat was about 1850°F. (The β transus of standard grade Ti-6Al-4V is 1820°F ± 25°F.) The presence of these small α particles may be the reason for the slightly lower fracture toughness of material quenched from 1850°F compared to material quenched from 1875°F. Inspection of the fracture surfaces of the compact tension specimens showed that the center one-third of the plate was significantly coarser grained than the rest of the plate after the 1850°F anneal. Grain size appeared to be uniform following the 1875°F anneal. Thus, it appears that a slight degree of alloy segregration existed in this plate causing the central region to have a somewhat lower β-transus temperature than the rest of the plate.

Microstructures of the 2.4-in. plate are shown in Figs. 27 and 28. This material was produced to specification for the B-1 program and is ELI grade with 0.13 wt pct oxygen maximum. Therefore, it may be expected to have a somewhat lower β-transus temperature than either the (standard grade) 1-in. plate or the 4 × 4-in. forged billets which were reported by the producer to contain 0.15 wt pct oxygen — assuming all other things being equal. The as-received 2.4-in. plate had two things in common with the as-received 1-in. plate; (1) the lowest fracture toughness values measured in this investigation at about 47 ksi-in$^{1/2}$; and (2) complete absence of lamellar α (as the result of nucleation and growth transformation of β) such as that appearing in Figs. 10,

11, and 15, representing Conditions 2, 3, and 7, for examples. As in the case of Condition 1, the as-received 2.4-in. plate, Condition 15, appears to have cooled so slowly from high in the α-β field that the primary α simply grew at the expense of residual α to adjust to the α/β ratios characteristic of lower temperatures.

Condition 16 represents the 2.4-in. plate given the heat treatment: 1750°F-1/2 h-WQ, 1000°F-2 h-AC. Two facts are worthy of note: (1) fracture toughness is at the highest level observed for material given an STA heat treatment, that is, K_{Ic} = 80 ksi-in$^{1/2}$; and (2) the β transformed by nucleation and growth (in contrast to martensitically) to produce a lamellar product characterized by having substantial areas in which the α platelet thickness appears to be larger than 1 μm. It is interesting to note that Conditions 4 and 10 have the same STA heat treatment, but have substantially lower fracture toughness, the values being 48 and 67 ksi-in$^{1/2}$, respectively. Note in Figs. 12 and 18 representing Conditions 4 and 10, respectively, that the β appears to have transformed martensitically in both cases; therefore, the former β areas are now tempered martensite, and the α' needles are less than 1 μm in thickness. In view of these conjectures associating low fracture toughness with the absence of transformed β to produce a lamellar product an α platelet size of at least 1 μm in transverse dimension, one is tempted to attribute the substantially higher fracture toughness of Condition 10 over that of Condition 4 to the presence of acicular (but very coarse) primary α in the former, compare Figs. 12 and 18.

Ti-6Al-4V plate for the B-1 program has a fracture toughness acceptance criterion of K_{Ic} = 70 ksi-in$^{1/2}$ or more. How then can the fracture toughness which we measured for the 2.4-in. plate (which was cut from plate delivered for the B-1 program) of K_{Ic} = 48 ksi-in$^{1/2}$ be squared with the acceptance criterion? We were advised that test blanks were cut by Timet from end trimmings from the mill stock and heat-treated as such. Therefore, there was a mass difference between the test specimen blank and the plate for delivery of about two orders of magnitude. While air cooling from solution heat treatment high in the α-β field produces lamellar structure in dimensions sufficient to satisfy the needs for test specimens, in the light of the microstructures of the as-received 1-in. and 2.4-in. plates (see Figs. 9 and 27), the

conclusion is inescapable that air cooling of the large masses represented by a commercial plate of 1 in. or more in thickness does not result in such lamellar structures. Such a conclusion, if verified, would have grave consequences for current plans for designing and building fail-safe wingbox structures, such as that for the B-1. It is planned to produce the wingbox structures for the B-1 by diffusion bonding in a retort to prevent oxidation and contamination of the work space. It is difficult to imagine how one could obtain a cooling rate rapid enough under such conditions to produce lamellar α if the maximum temperature in the bonding process is below the β transus temperature. In order to have the high fracture toughness values desired, it may be necessary to have a temperature excursion above the β transus after bonding in order to ensure a lamellar microstructure. Coarse Widmanstätten structure resulting from relatively slow cooling from above the β transus produces high fracture toughness as has been confirmed in the current investigation — see data for Conditions 7, 8, 9, and 13. However, a word of caution appears to be in order. There is some question whether such large grained materials will perform as well under fatigue loading with dwell time at maximum stress to simulate take-off and climb to altitude. A further condition of such evaluation for heavy sections is that the fatigue specimen be of sufficient thickness to give plane-strain loading conditions.

Microstructures of annealed Conditions 17, 18, and 19 representing 4×4-in. forged billet solution treated for various times at 1750°F are shown in Figs. 29 through 31. There are no significant differences either in microstructures, fracture toughness, or yield strength. Average values of fracture toughness and yield strength for the three conditions are 67 ksi-in$^{1/2}$ and 125 ksi, respectively. Solution heat-treated and aged conditions of the 4×4-in. forged billet, Conditions 20, 21, and 22, show little variation in microstructure, fracture toughness, or yield strength. Average values of fracture toughness and yield strength for these conditions are 53.5 ksi-in$^{1/2}$ and 145 ksi, respectively.

Microstructures of Conditions 27 and 28 representing annealed and STA heat treatments of 4×4-in. billet forged to develop alpha segregation or "stringy alpha" are shown in Figs. 35 and 36. At high magnification the difference between the α-segregated billet and the normal equiaxed billet (Figs. 29 through 34) is not readily apparent.

28

However, the difference is obvious at lower magnification as shown by Fig. 37. Comparison of fracture toughness of the α-segregated billet with that of the normal billet having the same heat treatment (that is, compare Conditions 17 and 27 for the annealed state, and Conditions 20 and 28 for the STA state) shows superior values associated with the α-segregated material. The discussion given above relating high fracture toughness to the presence of lamellar or acicular α suggests that perhaps the stringy primary α is responsible for the superiority of the α-segregated billet. It appears that alpha segregation is one inherent defect that need not be a cause for concern.

It is instructive to compare microstructures with fracture toughness for Conditions 4 (1-in. plate), 16 (2.4-in. plate), 20 (forged billet), and 28 (α-segregated forged billet) – see Figs. 12, 28, 32, and 36. All are basically equiaxed structures to which the 1750°F-1/2 h-WQ, 1000°F-2 h-AC heat treatment was applied. The β phase of Conditions 4 and 20 appears to have transformed martensitically and to have a lamellae thickness of less than 1 μm. Fracture toughness K_{Ic} values determined for these conditions were 48 and 56 ksi-in$^{1/2}$, respectively. On the other hand, the β phase of Conditions 16 and 28 appears to have transformed by nucleation and growth to produce lamellae in significant amounts that are 1 μm or larger in transverse dimension. Fracture toughness values determined for these conditions are 80 and 67 ksi-in$^{1/2}$, respectively. The higher fracture toughness of the 2.4-in. plate Condition 16 compared to the α-segregated forged billet Condition 28 is at least partly due to the fact that it is ELI grade; and, of course, the difference may be partly due to subtle differences in microstructure. Thus, there is further evidence that lamellar α of at least 1 μm thickness is necessary for high fracture toughness. In this regard it is of interest to note that according to Eq. 2 no benefit to fracture toughness derives from gain boundary α in Widmanstätten structures until its thickness exceeds 2.6 μm. Greenfield and Margolin observed that the fracture path in age hardened Widmanstätten structures was along α/β interfaces at the grain boundaries[7]. These authors proposed that increasing thickness of grain boundary α beyond 2.6 μm thickness makes an increasing contribution to fracture toughness through increasing the volume of material that is plastically deformed in advance of the crack tip. However, their paper offers no explanation for the necessity of the grain boundary α to exceed 2.6 μm.

3.4 COMMENTS ON STRUCTURAL DETAILS OBSERVED BY TRANSMISSION ELECTRON MICROSCOPY

Thin foils of Conditions 1, 4, 17, and 20 were studied by transmission electron micro-scopy. Conditions 1 and 4 represent 1-in. plate and 17 and 20 represent 4 × 4-in. billet, respectively. Conditions 1 and 17 represent annealed conditions; and had a microstructural characteristic in common: a transition structure of very fine α particles between the β and α phase regions. This structure is shown in Fig. 38. Since material having only an anneal high in the α-β field followed by air cooling (without a subsequent stress relief anneal at 1450°F) was not included in this study, the origin of this structure is not clear. However, since no indication of this transition structure was observed in samples of Conditions 4 and 20, which were water-quenched from solution treatment, it is hypothesized that this structure results from the nucleation and growth transformation of β to form the lamellar product starting from a solution treatment temperature below the β transus. It remains to be seen whether this structure forms upon cooling from above the β transus.

As a consequence of the inability of alloy partitioning (through diffusion) to keep up with the decreasing ratio of β to α as temperature is lowered, the outer region of the β-phase particles are richer in aluminum and poorer in vanadium than the core. (Note that the diffusion of aluminum in titanium alloys is particularly sluggish. Crossley demonstrated that once segregation has occurred in Ti-Al binary alloys, it is virtually impossible to achieve homogenization in practical times of annealing at temperatures below about 1800°F.[10,23]) It follows that the β at the α-β interface would be less stable than the core β, and that separation of α from it, either by martensitic transformation or precipitation, would occur under conditions that would not produce a similar reaction in the core β, or would produce it to a lesser degree. During cooling this less stable β transforms. The question arises, "Why are there two variants of α, one apparently starting at a well-defined interface, and the other starting about 600 Å from this interface?" It is suggested that two marten-sitic products are involved: (1) the cubic (probably fcc) martensitic initially reported by Williams and Blackburn,[24] and substantiated by Modin and Modin,[25] which is

associated with β enriched by relatively low temperature solution treatment; and (2) hcp martensite which forms from relatively lean β. The subsequent stress relief anneal at 1450°F would temper both products: the hcp martensite becoming stabilized by diffusion across its boundaries, and the cubic martensite by precipitating α.[24] Our present state of knowledge of this transition structure gives no reason to suppose that it is detrimental to fracture toughness.

Conditions 4 and 20, 1-in. plate and 4×4-in. billet, respectively, given the heat treatment 1750°F-1/2-h-WQ, 1000°F-2 h-AC, were also revealed by transmission electron microscopy to have a characteristic in common. A selected area diffraction pattern of Condition 4 showed prominent (0001) reflections, while one of Condition 20 showed weak (0001) reflections. The (0001 reflections may be due to the presence of ordering, or Ti_3Al precipitation; or they may be the result of double diffraction. The transmission work was not intensive enough to provide for a resolution between these alternative interpretations. The areas involved in both cases were martensitically transformed. Considering the effect of dissolved vanadium on reducing the solubility of aluminum in titanium (discussed above), one would expect hcp martensite to precitate Ti_3Al more readily than α formed by nucleation and growth. Martensitically formed α contains the alloy content of the parent β. Therefore, it would be supersaturated with respect to vanadium and have reduced solubility for aluminum as a consequence.

It was suggested above that Conditions 16 and 28 had significantly higher fracture toughness than Conditions 4 and 20 (although all had the same STA heat treatment) because the β phase of the former conditions transformed martensitically. It was suggested that transverse thickness of the α needles was the controlling factor in the higher toughness – the nucleation and growth α being thicker. A presumption of ordered α, or Ti_3Al, in the microstructures of Conditions 4 and 20 challenges this suggestion. Ordering or Ti_3Al precipitation may possibly be the controlling factor in their lower fracture toughness. In this case martensitic transformation is at fault, but not because it results in α needles that are $1\,\mu m$ or less in transverse dimension, but because it

31

produces α of greater supersaturation which aging at 1000°F readily initi-
ates precipitation of Ti_3Al. This suspicion of Ti_3Al as the culprit in degrading
fracture toughness and not martensitic transformation, per se, is consistent with
our finding that β-IBQ structures, both the as-quenched and the stress-relief
annealed martensitic Conditions 23 through 26, exhibited relatively high fracture
toughness. The stress-relief anneal of 1450°F-1 h-AC degraded fracture toughness
compared to the as-quenched conditions; and this temperature is just below the
$\alpha + \beta/\alpha + \beta + Ti_3Al$ transus of the Ti-6Al-4V composition.[22] Maximum em-
brittlement due to formation of Ti_3Al is associated with an aging temperature of
1000°F.[11] However, aging time as well as temperature is a significant factor in
the embrittlement phenomenon.[12]

This discussion of the relationship between fracture toughness, yield strength and
microstructure is summarized graphically in Fig. 8. All data points having
$K_{Ic} \leq 56$ ksi-in$^{1/2}$ represent material conditions which contained no nonmarten-
sitic, acicular α. They include the 1-in. and 2.4-in. plates in their as-received
conditions, and certain of the STA Conditions of equiaxed materials. These latter
conditions contained martensitically formed acicular α rather than nucleation
and diffusion-controlled growth acicular α. Two factors are suspect in the lower
fracture toughness of martensitically formed structures: (1) the fineness of the
α needles, and (2) their greater propensity to form Ti_3Al upon age hardening due
to their greater supersaturation with respect to the alloying additions aluminum
and vanadium.

3.5 FATIGUE CRACK GROWTH

The characteristic fatigue crack resistance of each of the twenty-eight conditions
is plotted in Figs. 39 through 66. These figures of crack growth rate (da/dN)
versus stress intensity range (ΔK) also include the upper bound asymptote for
ΔK at a crack growth rate approaching elastically unstable fracture. This upper
bound for ΔK is $0.9 K_{Ic}$. For Conditions 2, 7, 8, and 13, $0.9 K_Q$ is plotted.

Because the ratio of minimum load to maximum load, R, is 0.1 for these tests, ΔK corresponding to the highest fatigue crack growth rate is $K_{Ic}(1-R)$ or $0.9\,K_{Ic}$.

Equation fitting to da/dN data is a currently popular topic. It is appropriate to indicate that no simple form equation fits all data of this type. The equation

$$\frac{da}{dN} = C_1 \Delta K^n \tag{8}$$

developed by Paris, et al.[26,27] fits such data over small or moderate ranges of ΔK. Forman et al.[28] modified this equation to account for the upper asymptote of ΔK tending to elastically unstable fracture. When the range for $\frac{da}{dN}$ is at least three orders of magnitude, one usually observes a sigmoidal (s-shaped) curve between the upper asymptote of $\Delta K = K_{Ic}(1-R)$ and the lower asumptote of the fatigue crack growth threshold. This threshold is the ΔK value for crack growth rates less than 10^{-7} to 10^{-9} in. per cycle. Collipriest has proposed a form of such an equation as follows[29]:

$$da/dN = C_1 + C_2 \, TANH^{-1} \, \Phi \, (K_{eff}) \tag{9}$$

where:

$$C_1 \text{ and } C_2 = \text{scaling factors for data fit}$$

$$\Phi = \frac{\log\,(K_c K_o/K_{eff}^2)}{\log\,(K_o/K_c)}$$

$$K_o = \text{fatigue threshold value of intensity}$$

$$K_c = \text{critical value of stress intensity}$$

$$K_{eff} = (1-R)^m \, K_{max}$$

$$R = \text{minimum stress/maximum stress in fatigue}$$

$$m = \text{a material parameter, from unflawed specimen fatigue life test}$$

$$K_{max} = \text{maximum stress intensity in fatigue}$$

33

The derivation of an equation that fully describes the da/dN vs. ΔK relation for a material will be of value to designers and materials specialists in more accurately predicting fatigue life of aerospace structures. Materials test data over a small range of crack growth rate, along with fracture toughness, K_{Ic}, would then be sufficient to preview the full range of crack growth rate. This would save a lot of time and money over obtaining test data from below 10^{-7} to above 10^{-3} in. per cycle.

In the present study, data for some of the material conditions follows a sigmoidal form. These are Condition 2 (Fig. 40), Condition 6 (Fig. 44), Condition 7 (Fig. 45), Condition 9 (Fig. 47), Condition 24 (Fig. 54), Condition 16 (Fig. 58), and Condition 18 (Fig. 60). Extrapolation of these data to 10^{-7} or 10^{-8} in. per cycle indicates the ΔK threshold for fatigue crack growth is between 10 and 15 ksi-in$^{1/2}$. This apparent threshold is higher than the 6 to 8 ksi-in$^{1/2}$ at a crack growth rate of about 10^{-8} in. per cycle observed by Bucci for Ti-6Al-4V, 1/8-in. sheet, solution treated and aged (STA), or STA plus 1300°F-2 h-AC.[30] This difference in threshold ΔK may be due to differences in microstructure or crystallography texture, or both of these things. No other published data for Ti-6Al-4V threshold determination are known to the authors.

The combined crack growth data obtained in the present study is summarized in Fig. 67. The data are separated in major categories of microstructure – fine equiaxed, worked Widmanstätten, coarse equiaxed, Widmanstätten, and martensitic – as described in Table II. This figure was developed by constructing a set of "best fit" straight line segments through each individual set of data (Figs. 39 through 66), then combining these segments. All of the microstructure types exhibit overlapping crack growth rate behavior. Of particular interest is the crack growth resistance exhibited by the 1-in. plate, martensitic structure. Conditions 23 and 25, both martensitic, as quenched from β, give the lowest crack growth rate (about 3×10^{-6} in. per cycle) at ΔK = 30 ksi-in$^{1/2}$. Condition 25 has the lowest crack growth rate at all higher values of ΔK. The poorest resistance to fatigue crack growth is exhibited by Condition 12, 1-in. plate STA Widmanstätten structure, at rates above 7×10^{-5} in. per cycle, and Conditions 4 and 5, 1-in. plate STA fine equiaxed structures at lower rates.

34

Of particular interest is the fact that Condition 2 which had the highest fracture toughness value of 111 ksi-in$^{1/2}$ exhibited the highest crack growth rates in the ΔK range of 15 to 20 ksi. This fact suggests that the microstructural condition which produced this exceptionally high fracture toughness must be taken with some reservations. The concern should be directed to those submicroscopic features that would only be revealed by transmission electron microscopy.

The possible import of this range in fatigue crack growth resistance for the different microstructures can be assessed in the following way. By assuming some initial flaw size, one may compare the cycles to failure between the least and most resistant microstructures. To perform this crack growth computation, one must also assume an initial shape of the incipient flaw, the stress-time relation, and peak stress. The crack growth equation proposed by Paris, Eq. 8 above, can be applied to each set of data describable by a straight line or a series of straight lines on the log da/dN versus ΔK plot. The integral of this equation permits "growing" an assumed initial flaw to the critical value, when K_{max} approaches K_{Ic} for the assumed material.

This comparison of simulated service life in fatigue is presented in Fig. 68, for the least and most fatigue crack growth resistant conditions. The terminal (largest) crack size plotted for each condition is the critical crack size for the assumed values of peak stress. Computations for this figure are based on a sinusoidal stress with a peak stress of 80 ksi and stress ratio, R, of +0.1. The initial (incipient) flaw shape was assumed to be a semi-circular surface flaw oriented in a plane normal to the peak tensile stress and having a depth of 0.040 in. This flaw size and shape are a reasonable estimate of the largest flaw that would probably escape detection in an important aerospace structure, vigorously inspected by a variety of high-quality NDT techniques.

The calculated service life for all the other twenty-six microstructural conditions is probably bracketed by Conditions 12 and 13 for these assumed conditions of stress, flaw size, etc. Thus, all twenty-eight conditions would fall within a fatigue life between 1500 and 70,000 cycles to failure. For a larger size initial flaw or higher peak stress, the fatigue life would be shorter, and vice versa.

The crack growth curves in Fig 68 show that a major portion of the cyclic life is spent at the low crack growth rates. Thus, a major influence on fatigue life of a structure containing an incipient crack is the material's resistance to fatigue crack growth at rates below 10^{-5} in. per cycle. Rates higher than this pertain to only a small fraction (less than 20 percent) of the total fatigue life of the growing crack.

Martensitic structures such as represented by Conditions 23 and 25 do not commonly occur in Ti-6Al-4V aerospace structures. Such a structure would result from a low energy input, high melting efficiency welding process such as electron beam welding. Stress-relief annealing of such a welded structure would have the effect of degrading fatigue crack growth resistance of the as-welded martensitic structure. For example, stress relief annealed martensites, Conditions 24 and 26 (Figs. 54 and 56), exhibit 10 to 50 times higher crack growth rates at the same ΔK values as as-quenched martensite, Conditions 23 and 25 (Figs. 53 and 55). If stress-relief annealing an electron beam welded Ti-6Al-4V aerospace structure detracts from the fatigue life of the weldment (assuming incipient flaws may be present), then some other benefit should be demonstrated. It is not obvious that a valid reason for stress-relief annealing is always determined, but is assumed to be beneficial to reduce residual stresses in the weldment. If these residual stresses are compressive in the vicinity of an incipient flaw, then stress-relief annealing increases the stress intensity at such a flaw. Thus, one should also know the residual stress pattern in electron-beam welded titanium alloy plates before assuming stress-relief annealing will be beneficial.

3.6 MACROSCOPIC AND MICROSCOPIC FRACTURE APPEARANCE

Macroscopic fracture appearance of the twenty-eight conditions is reported in Table V. All of the conditions heat treated below the β transus have a "silky" fracture surface appearance at low magnifications (1 to 15X). Those specimens heat treated at 1850°F (Conditions 7 through 12, 23, and 24) have a crystalline (rough, faceted) appearance in the center third and silky in the outer thirds. Those specimens heat treated at 1875°F (Conditions 13, 14, 25, and 26) have a crystalline appearance over the entire

36

surface. This difference in macroscopic appearance is related to the β grain size, which grew rapidly above the β transus during solution treatment. The β transus is below 1875°F for both the 1-in. plate and the 4 × 4-in. forged billet. However, alloy segregation apparently exists in both of these mill products, causing the outer layers of the plate and billet to have a β transus above 1850°F and the core to have a β transus below 1850°F. Fracture toughness of the specimens experiencing β or α-β solution treatment in the same piece because of macroscopic segregation would tend to be governed by the core toughness rather than toughness of microstructure at and near the edge. This is because the highest degree of plane strain constraint is experienced at the core (mid-thickness) rather than the surface, where plane stress conditions prevail.

In summary, the macroscopic fracture appearance does not give any clue to specific fracture toughness of the structure, but only prior β grain size. A wide range of toughness is exhibited within both "silky" and "crystalline" macroscopic fracture appearance types.

Typical microscopic fracture appearance for the twenty-eight conditions is shown in Figs. 69 through 96. Crack propagation direction is toward 12 o'clock in all these figures. A rough, qualitative estimate of the area fraction of the different principal microscopic fracture features is included in Table V. These features pertain to the fast fracture surface only.

Quasi-cleavage is a fractographic mode occurring in low fracture tough microstructures. Because very little volume plastic deformation is incurred during formation of a quasi-cleavage crack, its relatively flat (two-dimensional) appearance facilitates identification of the constituent which contributes to low fracture toughness. As indicated in Table V, all of those conditions exhibiting a significant (> 5 pct) amount of quasi-cleavage are low in fracture toughness, regardless of product or microstructure type. The shape of these quasi-cleavage regions appears to correlate best with the morphology of primary α. For example, compare Fig. 74b and 14 for Condition 6 which has a K_{Ic} of 49 ksi-in$^{1/2}$. Similarly, compare Figs. 93b and 33 for Condition 21

which has a K_{Ic} of 51 ksi-in$^{1/2}$. The microfactographic feature best correlating with high fracture toughness is a large (> 20 μm diameter or width) void cavity. This is illustrated by Fig. 76b for Condition 8, which has a K_Q of 86 ksi-in$^{1/2}$, and by Fig. 77b for Condition 9, which has a K_{Ic} of 82 ksi-in$^{1/2}$. The presence of relatively coarse (> 3 μm thickness) platelets of α apears to promote growth of large void cavities rather than nucleation and growth of many small (1 to 5 μm diameter or width) voids of quasi-cleavage cracks. These observations are consistent with the previously discussed comments associating low toughness with equiaxed α and high toughness with coarse acicular structures. The microfractographic fatigue features are presented in Fig. 69a through 96a. The heterogeneous microscopic fatigue crack growth direction is readily apparent in the photo micrographs. The relation between fatigue microfractographic appearance and microstructural features is not obvious and correlating the two would take an effort beyond the intentions of this study.

4.0 SUMMARY AND CONCLUSIONS

Ti-6Al-4V alloy was studied in three mill product forms for the purpose of establishing a correlation between microstructure and fracture toughness. The mill products were: 1-in. plate characteristic of material being supplied for the F-14 and F-15 fighter programs, 2.4-in. plate characteristic of material being supplied for the B-1 bomber program and 4×4-in. forged billets. Mill product, processing, and heat treatment variables produced 28 microstructural conditions. Mechanical properties determined were: tension test, plane strain fracture toughness and crack growth rate. Metallographic means employed were: light microscopy, scanning electron microfractography, and a limited amount of transmission of electron microscopy.

Observed fracture toughness values varied from 47 to 111 ksi-in$^{1/2}$. Conditions having K_{Ic} values less than 60 ksi-in$^{1/2}$ were characterized by an absence of acicular α resulting from the nucleation and (diffusion dependent) growth transformation of β. The most significant finding was that commercial-size plates of 1-in. or more thickness air cooled from high in the α-β phase field do not have the same microstructures as similarly heat treated smaller volumes that are commensurate with test specimen blanks. The as-received 1-in. and 2.4-in. plates of Ti-6Al-4V were found to have an equiaxed, predominantly α structure having the lowest fracture toughness values measured in this study; i.e., about 48 ksi-in$^{1/2}$. Heat treatments similar to those reported for the as-received conditions of the plates were applied to test specimen blanks. These treatments produced microstructures consisting of equiaxed primary α plus acicular α resulting from nucleation and growth transformation of the β phase that existed at the solution treatment temperature. These conditions had fracture toughness values ranging from 62 to 111 ksi-in$^{1/2}$ in contrast to the 48 ksi-in$^{1/2}$ for the as-received conditions.

It appears that commercial size heavy plates cool so slowly, because of their mass, that the β phase is consumed by the primary α growing into it, rather than by its

39

nucleation and growth transformation. The former preserves the equiaxed condition existing at the solution treatment temperature, while the latter produces the familiar acicular product. This finding suggests a word of caution concerning structures resulting from working and solution heat treating in the α-β phase field: large structures of Ti-6Al-4V cannot be expected to have either the microstructure or the fracture toughness associated with test specimens unless cooling rate from solution treatment is approximately the same.

A correlation was found between microstructures and microfractographic features. Primary α was associated with quasi-cleavage (and lower fracture toughness). Wholly, or nearly so, acicular structures having platelets greater than 1 μm in thickness, and fully martensitic (unannealed) structures were associated with the higher fracture toughness values. Their fracture surfaces were characterized by the presence of large (> 20 μm) voids.

The major conclusion of this study is that for solution treatment below the β transus unless the microstructure contains a significant amount of acicular α formed by nucleation and growth transformation of α (rather than martensitically), plane strain fracture toughness will be less than 60 ksi-in$^{1/2}$. It would appear that microstructurally equiaxed heavy plates currently produced by the mills are not cooled rapidly enough from solution treatment to produce the type of microstructure associated with fracture toughness of more than 50 ksi-in$^{1/2}$.

40

REFERENCES

1. F. A. Crossley and R. W. Lindberg, "Microstructural Analysis of a High Strength Martensite-Beta Titanium Alloy," Proceedings, Second International Conference on the Strength of Metals and Alloys, ASM 1970, Vol. III, pp. 841–845

2. F. A. Crossley, R. L. Boorn, and R. W. Lindberg, and R. E. Lewis, "Fractrue Toughness of Transage 129 Alloy, Ti-2Al-11V-2Sn-11Zr," Titanium Science and Technology, R. I. Jaffee and H. M. Burte, eds, TMS-AIME Proceedings, Plenum Press, New York, 1973, pp. 2025–2039

3. F. A. Crossley and J. M. Van Orden, "A New Titanium Alloy for Forms and Weldments," Metal Engr. Quart., Vol. 13, 1973, pp. 55–61

4. E. A. Steigerwald, "Fracture Toughness," Titanium Course, New York University, 8–11 Sept 1969

5. W. J. Crichlow and T. Lunde, "High Cycle Fatigue Properties of Titanium in Aircraft Application," Titanium Course, New York University, 8–11 Sept 1969

6. J. M. Van Orden and L. L. Soffa, "Effect of Beta Working on 6A1-4V Titanium Alloy," ASM Technical Report System No. D8-24.3, Oct 1968

7. M. A. Greenfield and H. Margolin, "The Interrelationship of Fracture Toughness and Microstructure in a Ti-5.25Al-5.5V-0.9Fe-0.5Cu Alloy," Met. Trans., Vol. 2, Mar 1971, pp. 841–847

8. G. T. Hahn and A. R. Rosenfield, "Sources of Fracture Toughness: The Relation Between K_{Ic} and the Ordinary Tensile Properties of Metals," ASTM Symposium, Los Angeles, 18–19 Apr 1967

9. J. L. Henry, S. D. Hill, and T. T. Campbell, "Nitride Inclusions in Titanium Ingots: A Study of Possible Sources in the Production of Magnesium-Reduced Sponge," Met. Trans., Vol. 4, 1973, pp. 1859–1864

10. F. A. Crossley, "Titanium-Rich End of the Titanium-Aluminum Equilibrium Diagram," Trans. TMS-AIME, Vol. 236, 1966, pp. 1174–1185

11. F. A. Crossley and W. F. Carew, "Embrittlement of Ti-Al Alloys in the 6 to 10 Pct Al Range," Trans. AIME, Vol. 209, 1957, pp. 43–46

12. F. A. Crossley, "Kinetics of Ti_3Al Grain Boundary Precipitation in Ti-Al Binary and Ti-Al-X Ternary Alloys and Correlation with Mechanical Properties," Met. Trans., Vol. 1, 1970, pp. 1921–1929

13. D. E. Piper, S. H. Smith, and R. V. Carter, "Corrosion Fatigue and Stress-Corrosion Cracking in Aqueous Environments," Metals Engr. Quart., Vol. 8, 1968, pp. 50–63

14. Anon., "Standard Method of Test for Plane Strain Fracture Toughness of Metallic Materials," Amer. Soc. for Testing and Materials, Designation: E 399–72, May 1972

15. J. M Barsom, "Fatigue-Crack Propagation in High Yield-Strength Steels," Engineering Fracture Mechanics, Vol. 2, No. 4, June 1971, p. 301

16. J. E. Campbell, W. E. Berry, and C. E. Fedderson, Damage Tolerant Design Handbook, Metals and Ceramics Information Center, No. MCIC-HB-01, Dec 1972

17. M. J. Harrigan, "B-1 Fracture Mechanics Data for Air Force Handbook Usage," Report TFD-72-501-1; Los Angeles Division, Rockwell International (formerly North American Rockwell), Los Angeles, Cal., June 7, 1972

18. Anon., "Special ASTM Committee on Fracture Testing of High Strength Sheet Materials, Report No. 1," ASTM Bulletin; Am. Soc. for Testing Matls., Jan 1960, p. 29

19. G. R. Irwin, "Plastic Zone near a Crack and Fracture Toughness," Seventh Sagamore Ordnance Materials Research Conference, Aug 1960

20. W. H. Lewis, W. H. Sproat, and H. S. Pearson, "A Review of Nondestructive Testing for Aerospace Applications," Lockheed-Georgia Co., Marietta, Ga., Report No. ER-11051-1, June 1971

21. D. E. Pettit and D. W. Hoeppner, "The Influence of Nondestructive Inspection Parameters on the Preproof and Postproof Fatigue Crack Detection Inspection Limits for Fracture Mechanics Applications," Lockheed-California Co., Burbank, Ca., Report No. LR-25949, Aug 1973

22. F. A. Crossley, "Effects of the Ternary Additions: O, Sn, Zr, Cb, Mo, and V on the α/α + Ti_3Al Boundary of Ti-Al-Base Alloys," Trans Met. Soc., AIME, Vol. 245, 1969, pp. 1963–1968

23. F. A. Crossley, "Psuedo Two-Phase Titanium-Aluminum Alloys," Trans. ASM, Vol. 60, 1967, pp. 714–716

24. J. C. Williams and M. J. Blackburn, "A Comparison of Phase Transformations in Three Commercial Titanium Alloys," Trans. ASM, Vol. 60, 1967, pp. 373–383

25. M. Modin and S. Modin, "Phase Transformations in the Titanium Alloy Ti-6Al-4V, Jerkont. Ann., Vol. 155, 1971, pp. 425–428

26. P. C. Paris, M. P. Gomez, and W. E. Anderson, "A Rational Analytical Theory of Fatigue," Trends in Engineering, U. of Washington, V. 13, No. 1, 1961

27. P. C. Paris, "The Growth of Cracks Due to Variations in Loads," Ph.D. Thesis, Lehigh U., 1962

28. R. G. Forman, V. E. Kearney, and R. M. Engle, "Numerical Analysis of Crack Propagation in Cyclic-Loaded Structures," J. Basic Engr. Trans. ASME, V. 39, Series D, No. 3, Sept 1962, p. 459

29. J. E. Collipriest, "An Experimentalists View of the Surface Flaw Problem, "The Surface Crack & Physical Problems and Computational Solutions, ASME, N.Y., 1972, p. 43

30. R. J. Bucci, et al, "Fatigue Threshold Crack Propagation in Air and Dry Argon for a Ti-6Al-4V Alloy," Stress Analysis and Growth of Cracks, Part I, ASTM STP 513, Am. Soc. for Testing and Matls, 1972, p. 125

Table I

Ti-6Al-4V ALLOY MILL PRODUCTS

| Form | Supplier | Heat or Ingot No. | Weight (lb) | Chemistry (wt pct.) | | | | | | |
				Al	V	Fe	C	H	N	O
1-in. Plate	RMI	295900, Lot 06, S-R 00	413	6.5	4.0	0.19	0.02	0.0059	0.027 a	
2.4-in. Plate	Timet		90							b
4 x 4-in. Billet	Timet	K-8713	134	6.4	4.0	0.20	0.02	0.002	0.011	0.147
4 x 4-in. Billet (α-Segregated, Equiaxed)	Timet	K-8713	82	6.4	4.0	0.20	0 02	0.002	0.011	0.147

a - Specification maximum oxygen content of 0.2 wt pct.
b - ELI grade having a 0.13 wt pct maximum oxygen. The chemistry was not reported because this plate remnant was scheduled to be sent to the melt shop and its heat number identification was not maintained.

44

TABLE II

Summary of Ti-6Al-4V Microstructural Conditions Studies

Condition Number	Product	Microstructural Type	β-Solution Treatment	α-β-Solution Treatment	Age or Stress Relief Treatment
1	RMI 1-in. Plate	Fine Equiaxed (Standard)	(As Received)	1725°F-1 h-AC	1450°F-1 h-AC
2				1775°F-½ h-AC	1450°F-1 h-AC
3				1750°F-2 h-AC	1450°F-1 h-AC
4				1750°F-½ h-WQ	1000°F-2 h-AC
5				1750°F-2 h-WQ	1000°F-2 h-AC
6				1750°F-4 h-WQ	1000°F-2 h-AC
7	RMI 1-in. Plate	Widmanstätten	1850°F-½ h-AC	1775°F-½ h-AC	1450°F-1 h-AC
8				1750°F-2 h-AC	1450°F-1 h-AC
9				1750°F-4 h-AC	1450°F-1 h-AC
10				1750°F-½ h-WQ	1000°F-2 h-AC
11				1750°F-2 h-WQ	1000°F-2 h-AC
12				1750°F-4 h-WQ	1000°F-2 h-AC
13			1875°F-½ h-AC	1750°F-2 h-AC	1450°F-1 h-AC
14				1750°F-2 h-WQ	1000°F-2 h-AC
15	Timet 2.5-in. Plate	Worked Widmanstätten	(As Received)	1775°F-1 h-AC	1350°F-4 or 8 h-AC*
16				1775°F-½ h-AC	1450°F-1 h-AC
17	Timet 4- x 4-in. Billet	Coarse Equiaxed (Standard)	(As Forged)	1775°F-½ h-AC	1450°F-1 h-AC
18				1750°F-2 h-AC	1450°F-1 h-AC
19				1750°F-4 h-AC	1450°F-1 h-AC
20				1750°F-½ h-WQ	1000°F-2 h-AC
21				1750°F-2 h-WQ	1000°F-2 h-AC
22				1750°F-4 h-WQ	1000°F-2 h-AC
23	RMI 1-in. Plate	Martensitic	1850°F-½ h-IBQ	--	--
24				--	1450°F-1 h-AC
25			1875°F-½ h-IBQ	--	--
26				--	1450°F-1 h-AC
27	Timet 4- x 4-in. Billet	α-Segregated, Equiaxed	(As Forged)	1775°F-½ h-AC	1450°F-1 h-AC
28				1750°F-½ h-WQ	1000°F-2 h-AC

*The uncertainty about the annealing treatment is due to the fact that plate remnant was scheduled to be sent to the melt shop and its heat number identification was not maintained.

TABLE III

Summary of Mechanical Properties* Grouped by Structure Type & Ranked by Fracture Toughness

Product Condition No.	Structure Type **	$K_{Ic}(K_Q)$ ksi-in$^{\frac{1}{2}}$	a_1 in.	r_p in.	E399 Spec. Violations Major	Minor	F_{ty} ksi	F_{tu} ksi	Elong. (%)	RA (%)	10^6 psi	R_C No.
				ANNEALED								
1-in. Plate 2	E	(110.9)	.524	0.0329	A	-	140.7	148.1	15	37	17.6	35.6
3		62.4	.106	0.0104	-	-	140.7	148.8	17	24	18.8	35.4
1		46.9	.094	0.00567	-	-	143.5	150.6	18	27	19.1	36.1
				SOLUTION TREATED AND AGED								
5		50.7	.111	0.00533	-	j,l	159.9	171.6	12	28	18	43
6		48.6	.102	0.00464	-	l	164.3	174.4	12	26	17.4	42.2
4		47.9	.099	0.0045	-	l	164.5	172.6	15	32	17.8	42.6
				ANNEALED								
13	Wid.	(87.2)	.318	0.0257	A	n	125.2	136.4	10	11	16.5	35.3
8		(86.3)	.312	0.0244	A	j	127.1	141.9	12	15	16.7	36
7		(85.4)	.305	0.025	A	-	124.5	141.4	11	13	18.3	35
9		91.1	.281	0.0221	-	n	126.8	140.7	12	21	16.8	35
				SOLUTION HEAT TREATED AND AGED								
14		71.0	.217	0.011	-	j,m	155.6	168.2	FOG	5	18.3	43
10		66.8	.193	0.0096	-	n	157.0	172.2	10	11	18.2	42.7
12		58.9	.150	0.00717	-	j,l	160.2	174.0	7	11	17.1	42.8
11		58.0	.145	0.00702	-	n	159.4	172.1	8	18	18.3	42.9
				AS ICE BRINE QUENCHED FROM BETA								
25	a'	80.0	.271	0.0183	-	j,k,l,m	136.0	150.8	2***	10	17.9	39.9
23		77.6	.258	0.0146	-	k,l	148.0	168.9	10***	8	18.1	42.4
				STRESS RELIEF ANNEALED								
26		66.3	.189	0.010	-	j	152.6	160.7	5***	10	17.4	39.4
24		60.9	.159	0.00876	-	n	149.9	162.4	11	12	17.5	38.1
				SOLUTION HEAT TREATED AND AGED								
2.4-in. Plate 16	W.Wid.	73.9	.236	0.0182	-	j	134.4	146.1	15	37	18.6	34.4
				ANNEALED								
15		47.7	.095	0.00828	-	-	120.7	127.3	17	25	17.3	30.9
4 x 4-in. Billet 27	E a-Seg.	72.1	.219	0.0163	-	-	130.1	140.0	18	41	17.2	32.5
18	F	67.7	.192	0.0156	-	-	124.7	134.8	17	46	17.6	35.1
17		67.4	.189	0.0159	-	-	123.0	134.7	++	52	16.8	34.2
16		65.3	.179	0.0140	-	-	127.1	136.8	18	48	16.8	32.3
				SOLUTION HEAT TREATED AND AGED								
4 x 4-in. Billet 19	E a-Seg.	65.8	.184	0.012	-	-	138.2	148.6	11	24	17.2	34.8
20	F	66.4	.135	0.0081	-	j	144	157.3	10	42	16.2	36.3
22		53.4	.122	0.0073	-	j,n	143.8	159.1	12	36	16.6	36.6
21		50.6	.110	0.00627	-	-	147.2	159.8	12	34	16.8	36.5

* Description of headings:

    K_{Ic} – fracture toughness index, where $2.5(K_Q/F_{ty})^2 < 1.00$ in.

    K_Q – fracture toughness index, where $2.5(K_Q/F_{ty})^2 \geq 1.00$ in.

    a_1 – calculated maximum depth semicircular crack that would survive a proof stress of 120 ksi

    r_p – calculated plane strain critical plastic zone size

    E399 Spec. Violations – see Table IV

    F_{ty} – 0.2% offset tensile yield strength

    F_{tu} – ultimate tensile strength

    Elong– elongation in 1 inch

    RA – reduction of area

    E – Modulus of elasticity in tension

    R_C – Rockwell C scale hardness number

** E – equiaxed; Wid – Widmanstatten; W.Wid – worked Widmanstatten; and a' – martensitic

+ FOG – failed outside of gage length

*** Failed at scribe mark defining gage length

++ Gage marks obscured by deformation

46

TABLE IV

Identification of ASTM E 399 Fracture Toughness Test Specification Violations

Major violation

$$A = B,\ a_c,\ (W-a_c),\ \text{or } H \leqslant 2.5\ (K_Q/F_{ty})^2$$ 7.1.1

Minor Violations

$$j = \left| a_{\frac{1}{4}} - a_{\frac{1}{2}} \right|,\ \left| a_{\frac{1}{4}} - a_{3/4} \right|,\ \left| a_{\frac{1}{2}} - a_{3/4} \right| > 0.05\ a_c$$ 8.2.3

$$k = (a_{any} - a_o) < \text{larger of } 0.05\ a_c \text{ or } 0.05\ \text{in.}$$ 8.2.3

$$l,= a_l \text{ or } a_r \quad 0.9\ a_c$$ 8.2.3

$$m = \theta > 10 \text{ degrees}$$ 8.2.4

$$n = 30\ \text{ksi-in.}^{\frac{1}{2}}/\text{min.} \not< \Delta K/\Delta t \not< 150\ \text{ksi-in}^{\frac{1}{2}}/\text{min.}$$ 8.4

Where,

     B = specimen thickness
     a_c = critical crack length = $(a_{\frac{1}{4}} + a_{\frac{1}{2}} + a_{3/4})\ /\ 3$
     W = specimen length from load line
     H = specimen height from crack plane
     $a_{\frac{1}{4}}$, etc = fatigue crack length from load line at $\frac{1}{4}$, etc. thickness
     a_o = specimen notched length before fatigue precracking
     $a_{l,r}$ = fatigue crack length from load line on left or right side of specimen
     θ = angle between extension of fatigue precrack plane and plane of initial fast crack growth
     $\Delta K/\Delta t$ = rate of plane strain stress intensity factor increase in fracture toughness test

TABLE V

Macroscopic and Microscopic Fracture Appearance of
the Twenty-Eight Ti-6Al-4V Microstructural Conditions

Condition Number	$K_I(K_Q)$ ksi-in$^{\frac{1}{2}}$	F_{ty} ksi	Oblique Fracture %	Macroscopic Appearance		Microscopic Appearance — Ductile Rupture			Quasi-Clvge. %	Some Grain Boundary Separation
				Silky %	Crystalline %	Fine %	Coarse %	Very Coarse %		
1	47	144	7	100		70			30	
2	(111)	141	12			60	10	30		x
3	62	141	13			70	10		20	x
4	48	164	2			50	20		30	
5	51	160	4			70		15	15	x
6	49	164	3	100		40			60	x
7	(85)	124	14	67	33	40		60		
8	(86)	127	15			30		70		
9	82	127	14			20		80		
10	67	157	2			70		30		
11	58	159	2			60		20	20	
12	59	160	1	67	33	60	10	15	15	x
13	(87)	125	*		100		40	60		
14	71	156	*		"	50	10	40		
15	48	121	43	100		20	50	20	10	
16	80	134	22			40		60		x
17	67	123	9			50		20	30	
18	68	125	7			40	25	25	10	
19	65	127	8			60			40	
20	56	144	3			40	10		50	
21	51	147	3			30	10		60	x
22	53	144	5			30	20		50	
23	78	148	6			70		30		
24	61	150	6			50	10	30	10	
25	80	136	*			90	10			
26	66	153	4			90	10			
27	72	130	8			30	40		30	x
28	66	138	8	100		40		20	40	

* Fracture surface too rough to measure shear lip width.
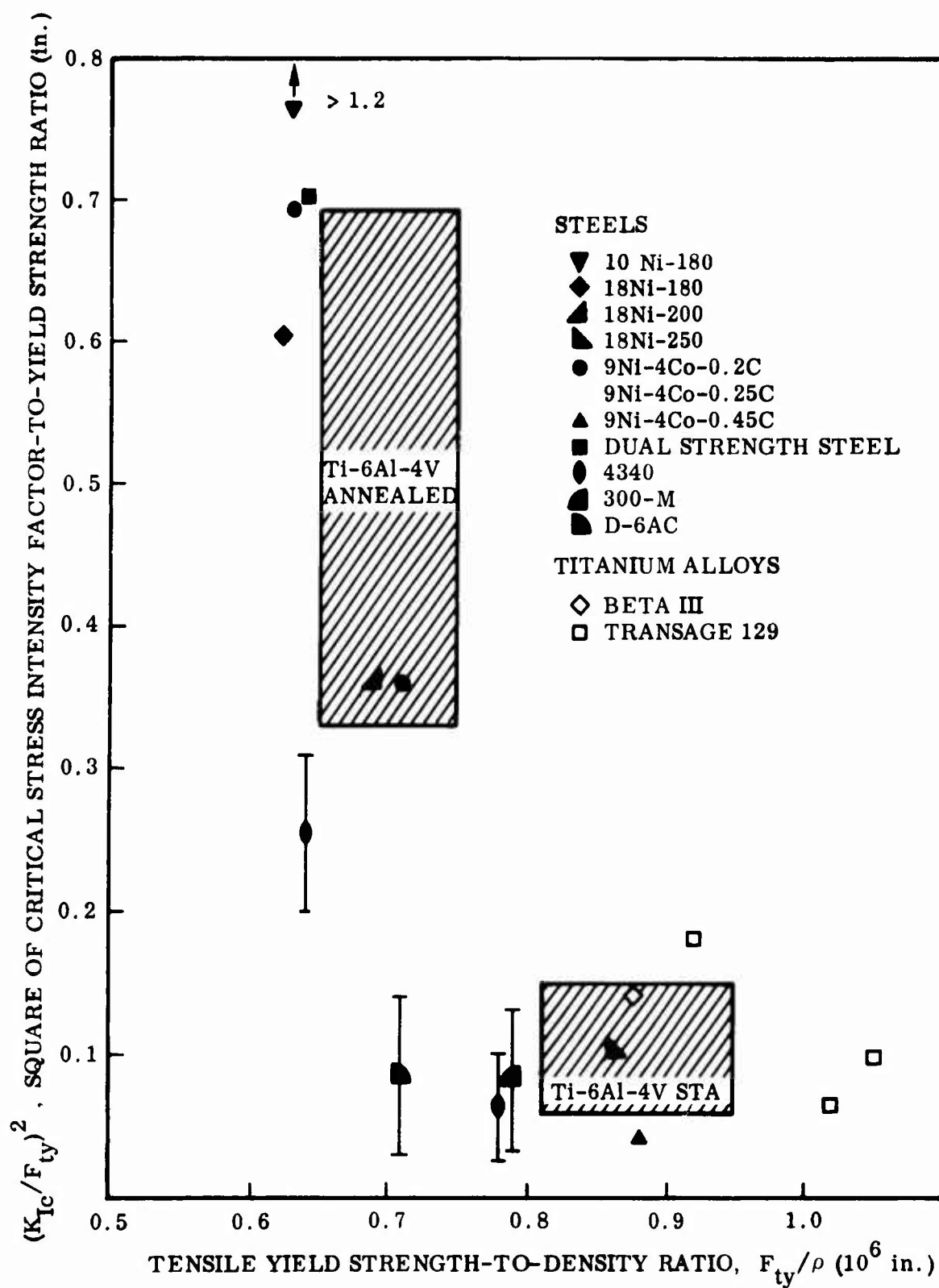
Fig. 1 Effect of specific yield strength on plastic zone size parameters at onset of elastically unstable crack growth for selected high-strength alloys.
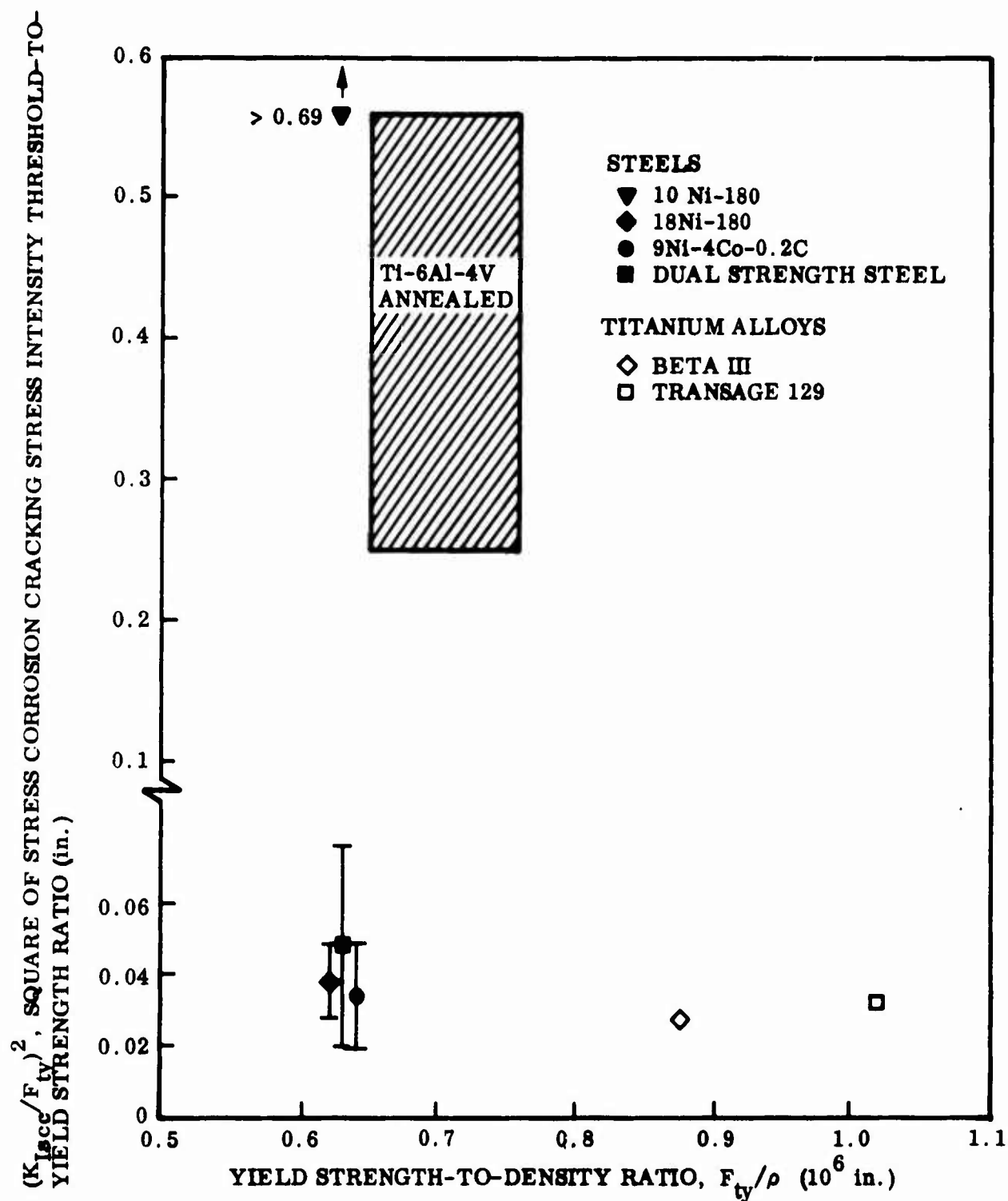
Fig. 2 Effect of specific yield strength on plastic zone size parameter at threshold of stress corrosion crack growth in salt water for selected high-strength alloys.

250 LB 9 IN. SQ, 20 IN. L

1750°F PRESS FORGE

6 IN. SQ × 45 IN. L

ABRASIVE CUT

BALANCE 19 IN.

26 IN.

1750°F PRESS
FORGE

2100°F (1 HR) FC
25°F/HR TO
1750°F AC

4 IN SQ × 58 IN. L
134 LB
STD EQUIAXED

CUT 1/2
6 IN. SQ × 9 IN. L

1750°F PRESS
FORGE

CUT 1/2
6 IN. SQ × 9 IN. L

1850°F PRESS
FORGE

4 IN. SQ × 31 IN. L
82 LBS

ALPHA SEGREGATED
EQUIAXED

5 IN. SQ × 13 IN. L

4 IN. SQ × 35 IN. L
86 LB

ALPHA SEGREGATED
WORKED WIDMANSTATTEN
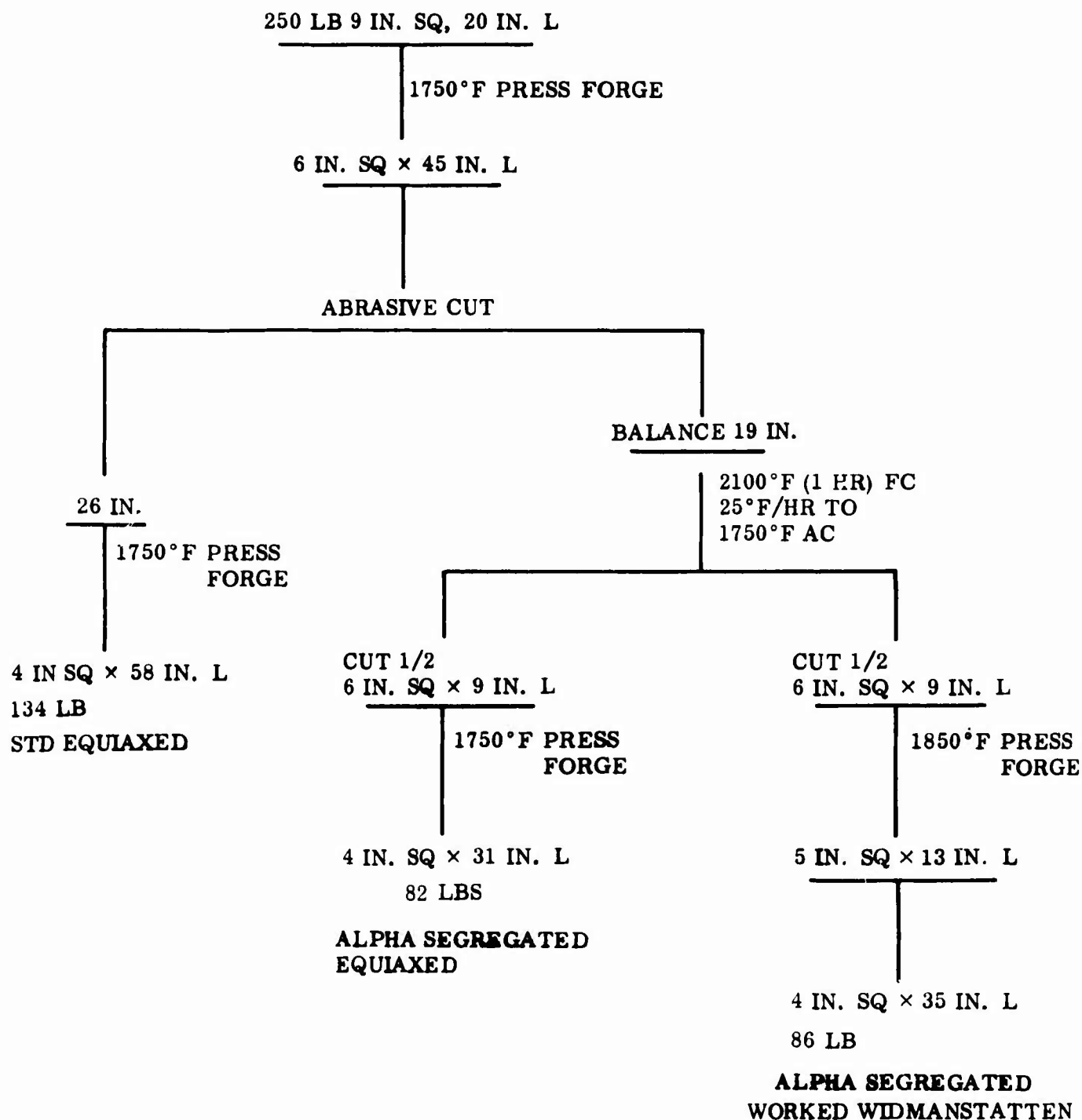
Fig. 3 Processing schedule for Ti-6Al-4V forged billets.

Fig. 4   Tensile specimen.

(4)

3/8-24 UNF, CLASS 2
BOTH ENDS

1/2 MINIMUM

3/8 MINIMUM R

(3)

(2)

32

3 MINIMUM

1-3/8 MINIMUM

1.000±.005

0.250±.005 DIA.

3/8 MINIMUM R

1/2 MINIMUM
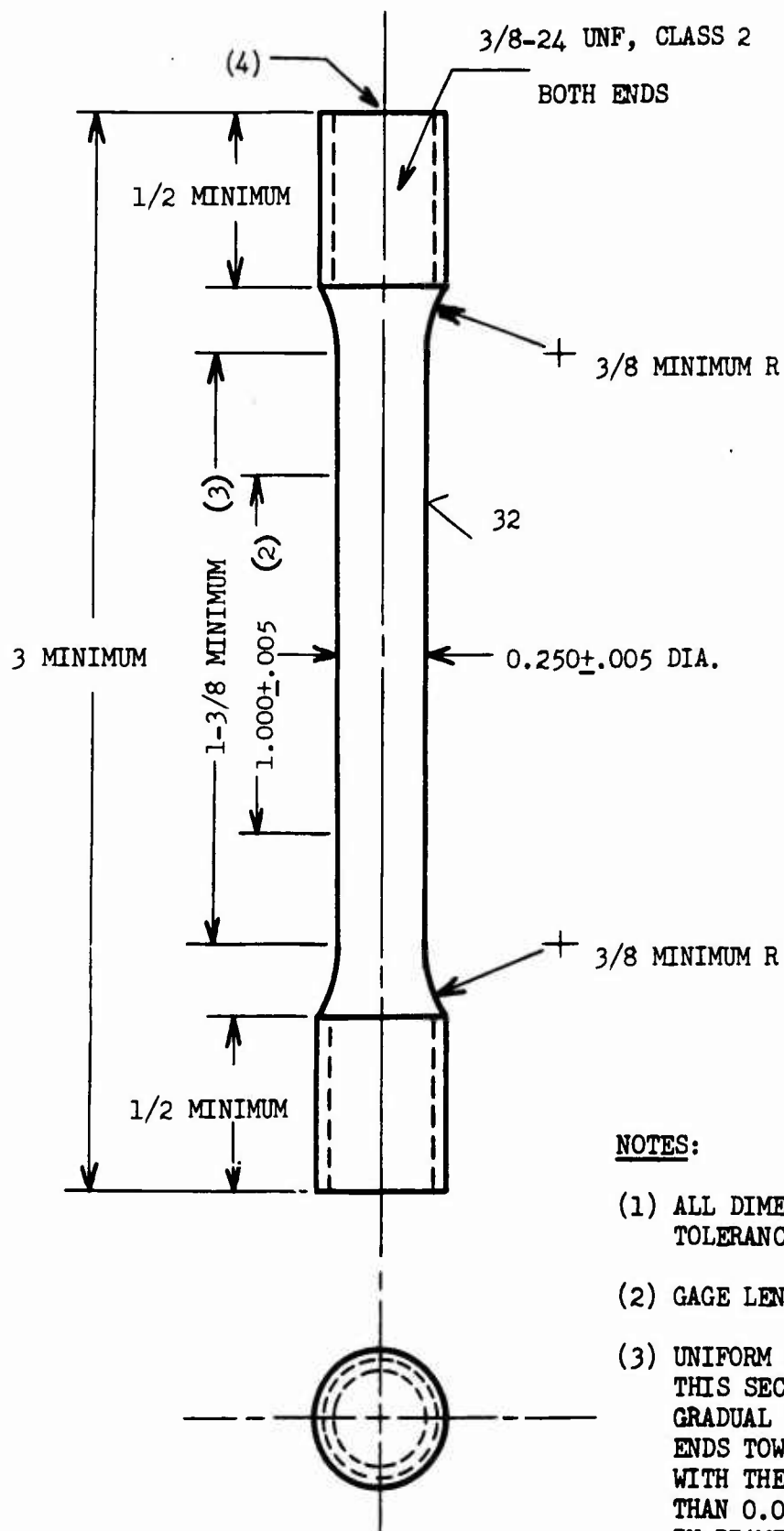
NOTES:

(1) ALL DIMENSIONS AND
    TOLERANCES IN INCHES.

(2) GAGE LENGTH.

(3) UNIFORM REDUCED SECTION.
    THIS SECTION MAY HAVE A
    GRADUAL TAPER FROM THE
    ENDS TOWARD THE CENTER,
    WITH THE ENDS NOT MORE
    THAN 0.0025 IN. LARGER
    IN DIAMETER THAN THE
    CENTER.

(4) LATHE CENTER O.K.

52
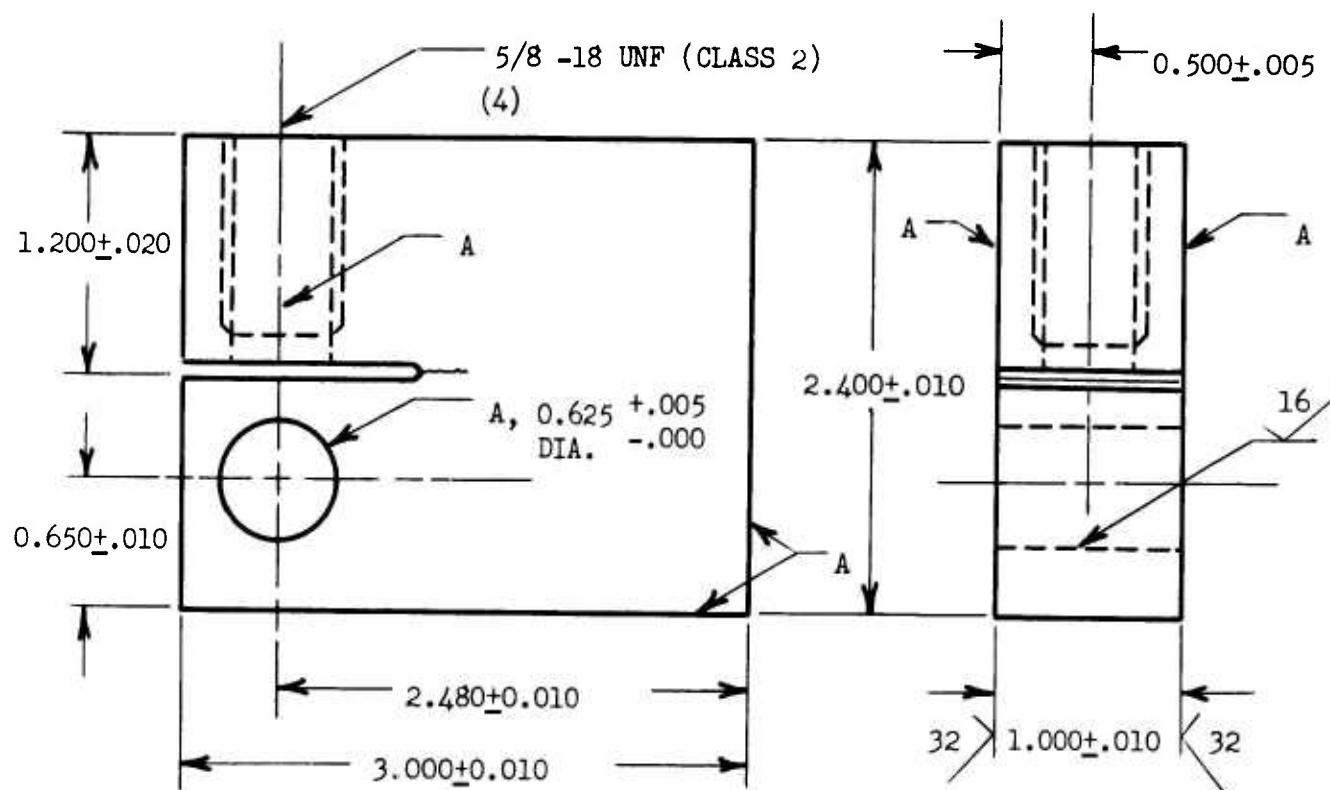
NOTES:

(1) ALL DIMENSIONS AND TOLERANCES IN INCHES.

(2) "A" SURFACES SHALL BE PERPENDICULAR AND PARALLEL
     AS APPLICABLE TO WITHIN 0.004 IN. TIR.

(3) ROUGHNESS ON ALL SURFACES NOT TO EXCEED 64 RMS
     UNLESS OTHERWISE SPECIFIED.

(4) HOLE TO BE FULL THREADED TO 1.00 IN. MIN. DEPTH

Fig. 5 Compact tension specimen.
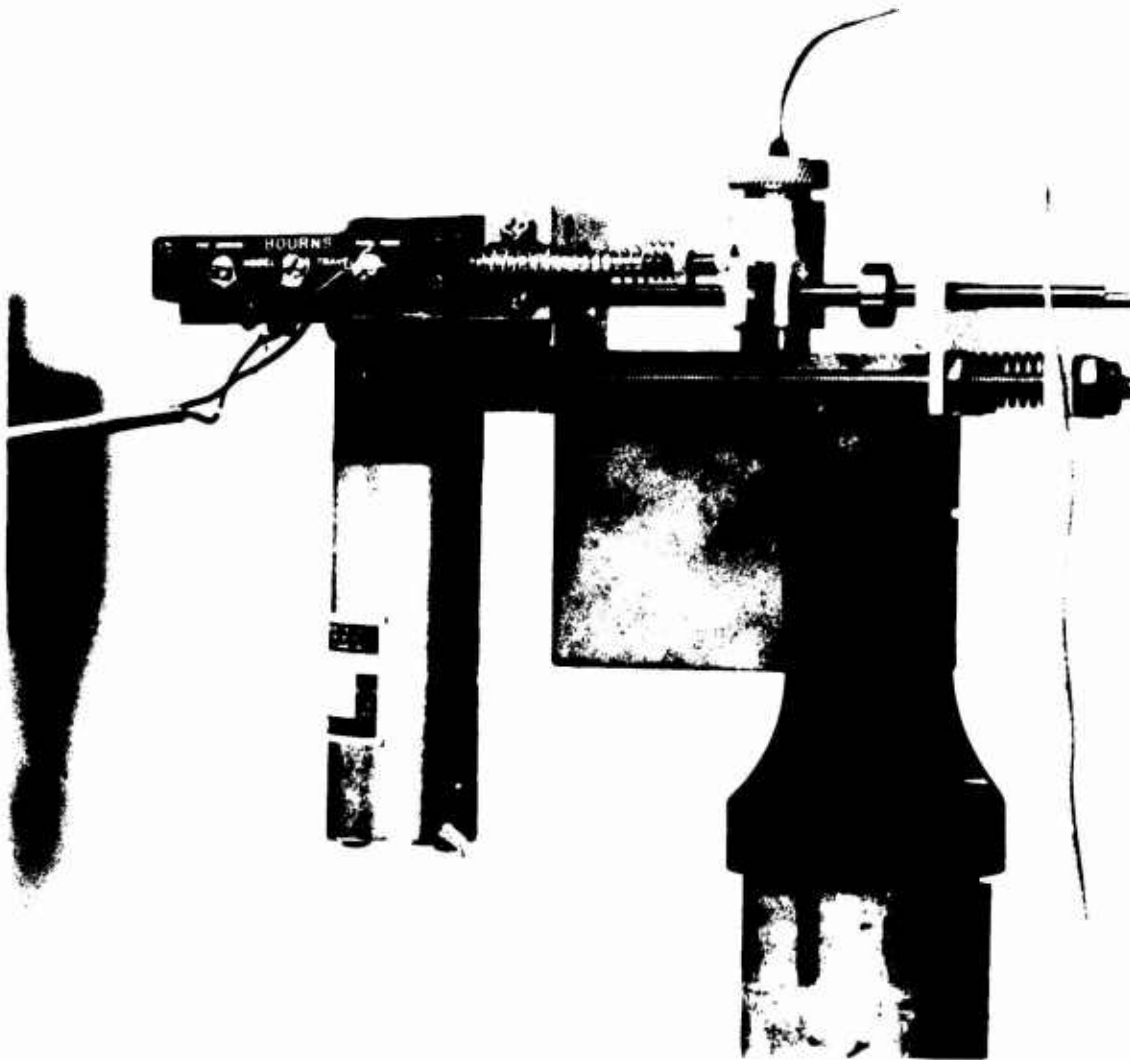
B 2853

Figure 6 Ultrasonic track follower mounted on
specimen during fatigue track growth rate test.

54

COMPACT TENSION K$_{Ic}$ TEST RECORD

Fracture Behavior Laboratory
Dept. 52-31, Bldg. 204
Materials and Structures Lab.

```
┌─────────────────────────────────────────────────────────────────────────┐
│                               SUMMARY                                     │
│                                                                           │
│  Material  Ti-6Al-4V              Tests by R.M.H.       Date 5-29-73      │
│  Specimen No. NAVAIR  01K-2       Calculations by TMM   Date 8-9-73       │
│  K_f(max)   15.42    ksi-in^½     Checked by  REL       Date 8-9-73       │
│  ΔK_f at a_f  13.88  ksi-in^½                           Date              │
│  K_f(max)/E  0.000807  in^½                                               │
│  K_Q    46.9     ksi-in^½         Precracking Temperature (T_1) 78 °F     │
│  P_max/P_Q   1.04                 Test Temperature (T_2)  78  °F          │
│  2.5(K_Q/F_ty)^2  0.268           Relative Humidity    48  %              │
│  K_Ic   46.9    ksi-in^½          Fracture Appearance  7  % Oblique       │
│  R_sc   0.382                                       SILKY                 │
│                                   ASTM E399-72                            │
└─────────────────────────────────────────────────────────────────────────┘
```

1. Material: 1-in. plate

   1.1 Heat Treatment: as-rec'd [1725°F-1hr-AC; 1450°F-1hr-AC]

   1.2 Process History:

   1.3 Properties: F$_{tu}$ 150.6 ksi; F$_{ty}$ 143.5 ksi; E 19.1 10^6 psi; 18 % Elong.;

   27 % RA; — Ft-lbs. CVN at — °F

2. Specimen:

   2.1 Thickness, B: 1.004 in.   2.4 R/W   0.486
   2.2 Depth, W: 2.48 in.   2.5 Notch Length, a$_o$: 0.470 in.
   2.3 Height, 2H: 2.40 in.   2.6 Orientation: TL

3. Fatigue Precracking:

Run No.	a$_i$(1)* (in.)	a$_i$(r)* (in.)	P$_{max}$ (lbs.)	F$_{min}$ (lbs.)	N Cycles	a$_f$(1)* (in.)	a$_f$(r)* (in.)	K$_f$(max.)** (ksi-in^½)	ΔK$_f$ @ a$_f$** (ksi-in^½)	Frequency (Hz)
1	.500	.500	7k	0.7K	29150	.555	.555			10
2	.555	.555	4K	0.4K	30159	.605	.605			10
3	.605	.605	7k	0.7k	5415	—	—			10
4	—	—	4k	0.4k	51029	1.0553	1.0461			10
5										
6			Σ =	115,753						
7										
8										

* a$_i$ and a$_f$ are measured at the specimens left (1) and right (r) free surfaces.
** stress intensity calculated using the average value of a$_f$ [(a$_f$(1) + a$_f$(r))/2] .
Note: Stress intensity values in the summary calculated using the post-test final crack size a$_c$ (Section 4.4).

Fig. 7   Typical record for fracture toughness test.
         Illustration is for Ti-6Al-4V Condition 1.

COMPACT TENSION K_{Ic} TEST RECORD (continued)

4. Final Crack Measurements:

4.1 $a_{\frac{1}{4}}$:	1.107 + ___ in.	4.5 a_c/W	0.448	
4.2 $a_{\frac{1}{2}}$:	1.116 + ___ in.	4.6 (a_{left}:	1.055 + ___ in.)	
4.3 $a_{3/4}$:	1.109 + ___ in.	4.7 (a_{right}:	1.046 + ___ in.)	
4.4 $a_{avg} = a_c$:	1.111 + ___ in.	4.8 crack plane, Θ:	0 degrees	

5. Tension Testing:
(Load vs. Crack Opening Displacement Record Attached)

5.1 COD Gage No.:	8848
5.2 Loading rate:	20 k lbs/min.
5.3 Loading rate in terms of K_I:	115 ksi-in$^{\frac{1}{2}}$/min.
5.4 Elastic compliance (v/P):	47.6 μ-in/lb.
5.5 Load at 5% Secant Intercept, P_5:	8.15 k lbs.
5.6 Maximum load, P_{max}:	8.48 k lbs.
5.7 Load at onset of unstable crack growth, P_Q:	8.15 k lbs.
5.8 P_{max}/P_Q:	1.04
5.9 $f (a/W)$:	6.09523
5.10 $K_Q = (P_Q/BW^{\frac{1}{2}}) f (a/W)$:	46.9 ksi-in$^{\frac{1}{2}}$

6. Fracture Appearance:

6.1 Width of flat fracture, f:	0.85 in.
6.2 Oblique fracture, $(B-f)/B \times 100$:	16.9 %

7. $K_Q = K_{Ic}$ if following criteria not violated:

	E399 Section	Not Violated	Violated
a. a_c and $B \geq 2.5 (K_Q/\sigma_{ys})^2$	7.1.1	■	☐
b. $0.45 \leq a/W \leq 0.55$	7.2.1	■	☐
c. $N \leq W/16$	7.2.2	■	☐
d. $(a_f - a_1) \geq 0.05 a_c$ or 0.05 in.	7.2.3	■	☐
e. $K_{f\ max}/E \leq 0.002$ in$^{\frac{1}{2}}$	7.4.2	■	☐
f. K_f max $\leq 0.6 K_Q$ (last 0.025(a_c))	7.4.2	■	☐
g. $\Delta K_f \geq .9 K_f$	7.4.3	■	☐
h. $K_{f(max)_{T_1}} \leq 0.6 (\sigma_{Y.S._{T_1}} / \sigma_{Y.S._{T_2}}) K_{Q_{T_2}}$	7.4.4	☐ N/A	☐
i. Size tolerances	8.2	■	☐
j. $|a_{\frac{1}{4}} - a_{\frac{1}{2}}|$, $|a_{\frac{1}{4}} - a_{3/4}|$, $|a_{\frac{1}{2}} - a_{3/4}| \leq 0.05(a_c)$	8.2.3	■	☐
k. $(a_{any} - a_o) \geq$ larger of 0.05 a_{avg} or 0.05 in.	8.2.3	■	☐
l. a_1 or $a_r \geq 0.9 a_{avg}$	8.2.3	■	☐
m. $\Theta \leq 10°$	8.2.4	■	☐
n. 30 ksi-in$^{\frac{1}{2}}$/min. $\leq K/\Delta t \leq 150$ ksi-in$^{\frac{1}{2}}$	8.4	■	☐
o. Alignment	8.4	■	☐
p. $P_{max}/P_Q \leq 1.1$	9.1.2	■	☐

8. If 7a only violation, then:
$$R_{sc} = 2P_{max} (2W + a)/B(W-a)^2 \sigma_{YS}$$

0.382

Fig. 7 Typical record for fracture toughness test.
Illustration is for Ti-6Al-4V Condition 1.
(continued)
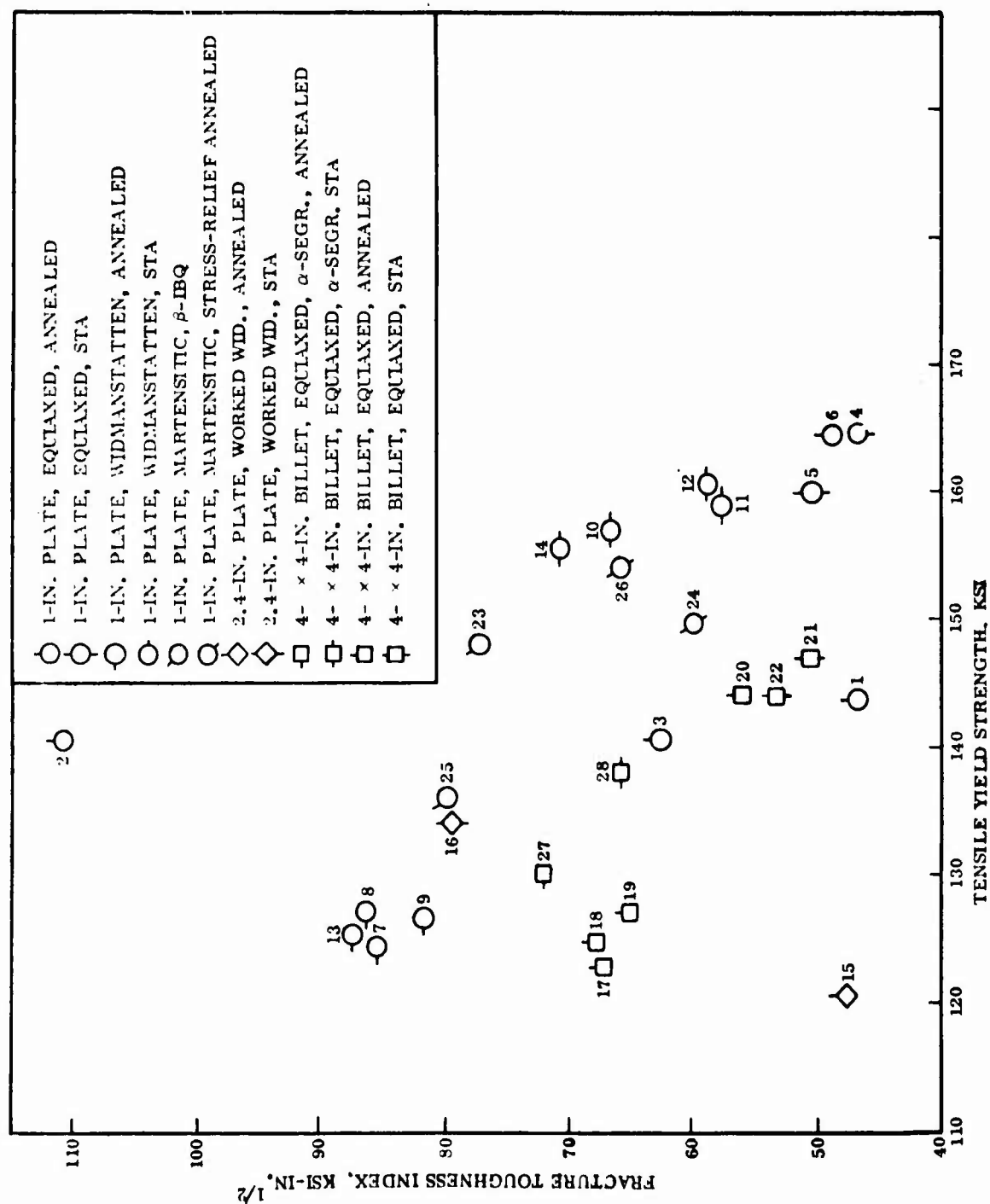
Fig. 3 Fracture toughness versus yield strength comparison for the twenty-eight Ti-6Al-4V conditions.

B4630   X1000

Fig. 9 - Ti-6Al-4V Condition 1, 1-in. plate, as received (1725°F-1 h-AC, 1450°F-1 h-AC). $K_{Ic} = 47$ ksi-in$^{\frac{1}{2}}$, $F_{ty} = 144$ ksi.

B4632   X1000

Fig.10 - Ti-6Al-4V Condition 2, 1-in. plate, 1775°F-$\frac{1}{2}$ h-AC, 1450°F-1 h-AC. $K_Q = 111$ ksi-in$^{\frac{1}{2}}$, $F_{ty} = 141$ ksi.

Etchant: 10 pct aq. sol. of HBF_4, immersion for 1.5 to 2 min.

58
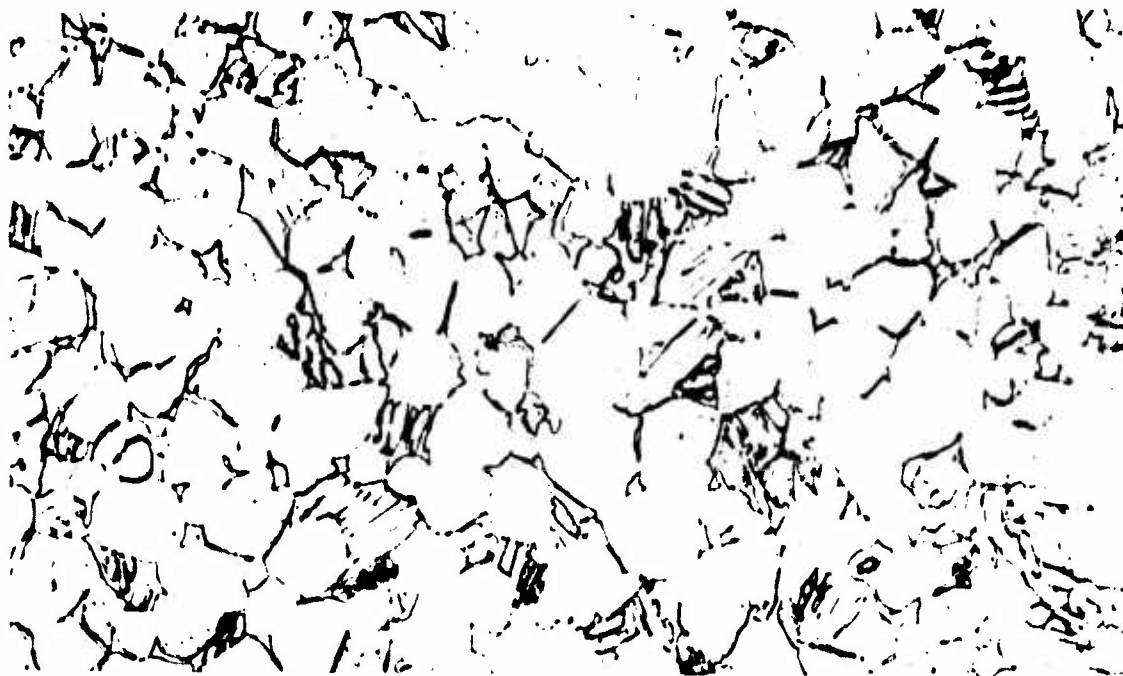
B4639   X1000

Fig. 11 - Ti-6Al-4V Condition 3, 1-in. plate, 1750°F-1 h-AC, 1450°F-1 h-AC.
K_{Ic} = 62 ksi-in^{2}, F_{ty} = 143 ksi.
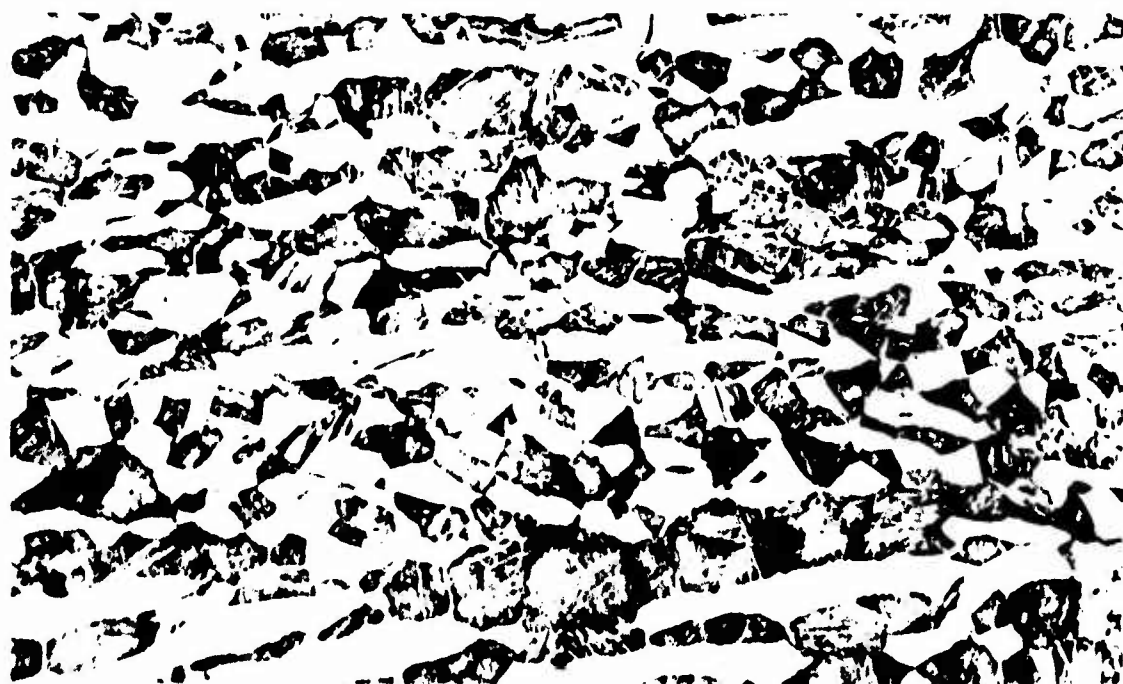
B4640   X1000

Fig. 12 - Ti-6Al-4V Condition 4, 1-in. plate, 1750°F-$\frac{1}{2}$ h-WQ, 1000°F-2 h-AC.
K_{Ic} = 48 ksi-in^{2}, F_{ty} = 164 ksi.

Etchant: 10 pct aq. sol. of HBF$_{4}$, immersion for 1.5 to 2 min.

59
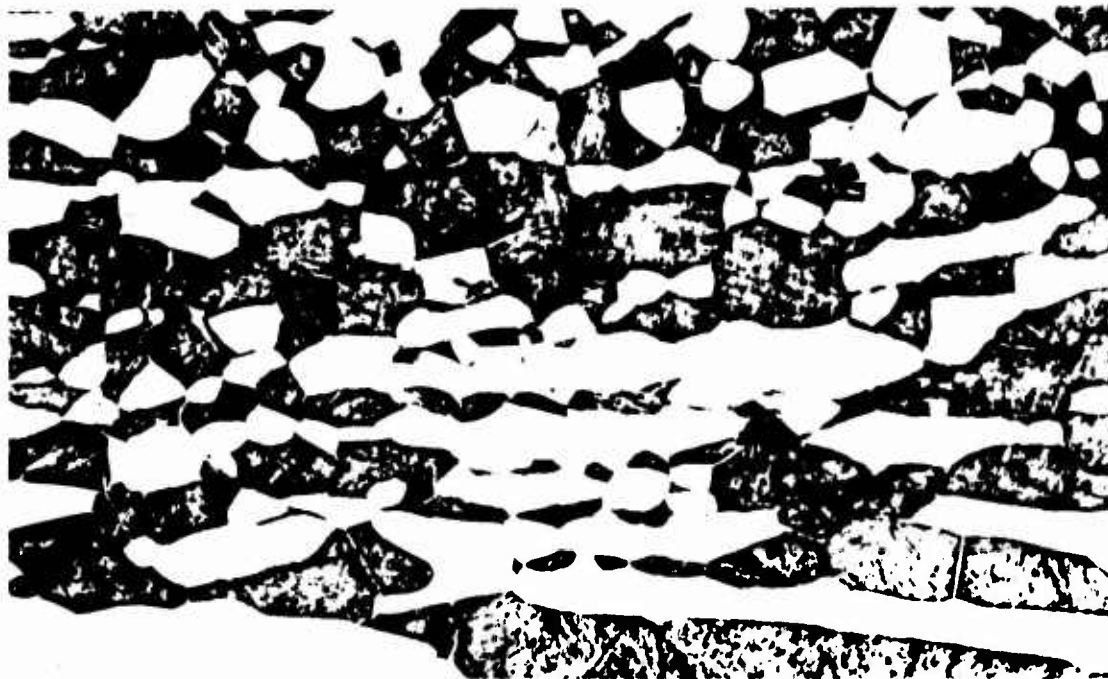
B4641   X1000

Fig. 13 - Ti-6Al-4V Condition 5, 1-in. plate, 1750°F-2 h-WQ, 1000°F-2 h-AC. K_{Ic} = 51 ksi-in$^{\frac{1}{2}}$, F_{ty} = 160 ksi.

B4642   X1000

Fig. 14 - Ti-6Al-4V Condition 6, 1-in. plate, 1750°F-4 h-WQ, 1000°F-2 h-AC. K_{Ic} = 49 ksi-in^{2}, F_{ty} = 164 ksi.

Etchant: 10 pct aq. sol. of 49 pct conc. HBF_4, immersion for 1.5 to 2 min.

60

B.646   X1000

Fig. 15 - Ti-6Al-4V Condition 7, 1-in. plate, $1850^{O}F-\frac{1}{2}$ h-AC, $1775^{O}F-\frac{1}{2}$ h-AC, $1450^{O}F-1$ h-AC. K_Q = 85 ksi-in, F_{ty} = 124 ksi.
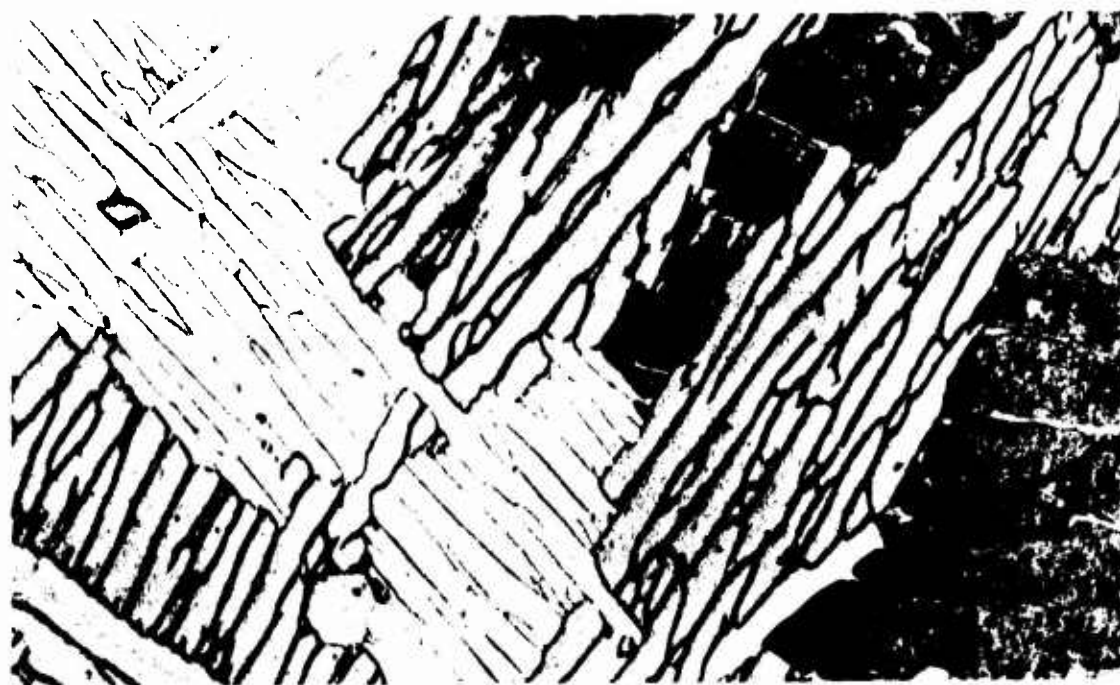
B4644   X1000

Fig. 16 - Ti-6Al-4V Condition 8, 1-in. plate, $1850^{O}F-\frac{1}{2}$ h-AC, $1750^{O}F-2$ h-AC, $1450^{O}F-1$ h-AC. K_Q = 86 ksi-in, F_{ty} = 127 ksi.

Etchant: 10 pct aq. sol. of 49 pct conc. HBF_4, immersion for 1.5 to 2 min.
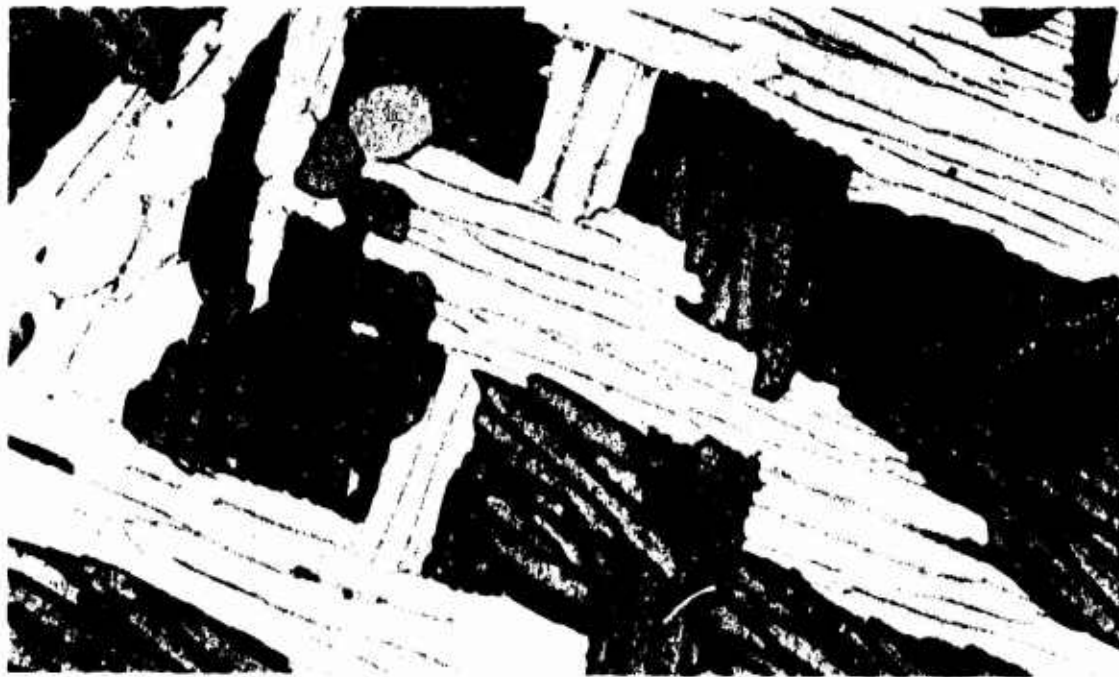
B4647   X1000

Fig. 17 - Ti-6Al-4V Condition 9, 1-in. plate, 1850°F-$\frac{1}{2}$ h-AC, 1750°F-4 h-AC
         1450°F-1 h-AC. K_{Ic} = 82 ksi-in$^{\frac{1}{2}}$, F_{ty} = 127 ksi.

B4648   X1000

Fig. 18 - Ti-6Al-4V Condition 10, 1-in. plate, 1850°F-$\frac{1}{2}$ h-AC, 1750°F-$\frac{1}{2}$ h-
         WQ, 1000°F-2 h-AC. K_{Ic} = 67 ksi-in$^{\frac{1}{2}}$, F_{ty} = 157 ksi.

Etchant: 10 pct aq. sol. of 49 pct conc. HBF$_4$, immersion for 1.5 to 2 min.

62

B4649   X1000

Fig. 19 - Ti-6Al-4V Condition 11, 1-in. plate, 1850^OF-$\frac{1}{2}$ h-AC, 1750^OF-2 h-WQ, 1000^OF-2 h-AC. K_{Ic} = 58 ksi-in^2, F_{ty} = 159 ksi.

B4650   X1000

Fig. 20 - Ti-6Al-4V Condition 12, 1-in. plate, 1850^OF-$\frac{1}{2}$ h-AC, 1750^OF-4 h-WQ, 1000^OF-2 h-AC. K_{Ic} = 59 ksi-in^2, F_{ty} = 160 ksi.

Etchant: 10 pct aq. sol. of 49 pct conc HBF_4, immersion for 1.5 to 2 min.

63

B4651   X1000

Fig. 21 - Ti-6Al-4V Condition 1s, 1-in. plate, 1875°F-½ h-AC, 1750°F-2 h-
          AC, 1450°F-1 h-AC. K_Q = 87 ksi-in², F_{ty} = 125 ksi.

B4652   X1000

Fig. 22 - Ti-6Al-4V Condition 1s, 1-in. plate, 1875°F-½ h-AC, 1750°F-2 h-
          WQ, 1000°F-2 h-AC. K_{Ic} = 71 ksi-in², F_{ty} = 156 ksi.

Etchant: 10 pct aq. sol. of 49 pct conc. HBF₄, immersion for 1.5 to 2 min.

64

B4659   X1000

Fig. 23 - Ti-6Al-4V Condition 23, 1-in. plate, $1850^{O}F-\frac{1}{2}$ h-IBQ.
K_{Ic} = 78 ksi-in^2, F_{ty} = 148 ksi.

B4660   X1000

Fig. 24 - Ti-6Al-4V Condition 24, 1-in. plate, $1850^{O}F-\frac{1}{2}$ hr-IBQ, $1450^{O}F$-1 h.
AC. K_{Ic} = 61 ksi-in^2, F_{ty} = 150 ksi.

Etchant: 10 pct aq. sol. of 49 pct conc. HBF$_4$, immersion for 1.5 to 2 min.

65

B-661   X1000

Fig. 25 - Ti-6Al-4V Condition 25, 1-in. plate, $1875^{\circ}F-\frac{1}{2}$ h-IBQ.
$K_{Ic} = 80$ ksi-in, $F_{ty} = 156$ ksi.

B-662   X1000

Fig. 26 - Ti-6Al-4V Condition 26, 1-in. plate, $1875^{\circ}F-\frac{1}{2}$ h-IBQ, $1450^{\circ}F-$
1 h-AC. $K_{Ic} = 66$ ksi-in$^{\frac{1}{2}}$, $F_{ty} = 153$ ksi.

Etchant: 10 pct aq. sol. of 49 pct conc. HBF$_4$, immersion for 1.5 to 2 min.

66
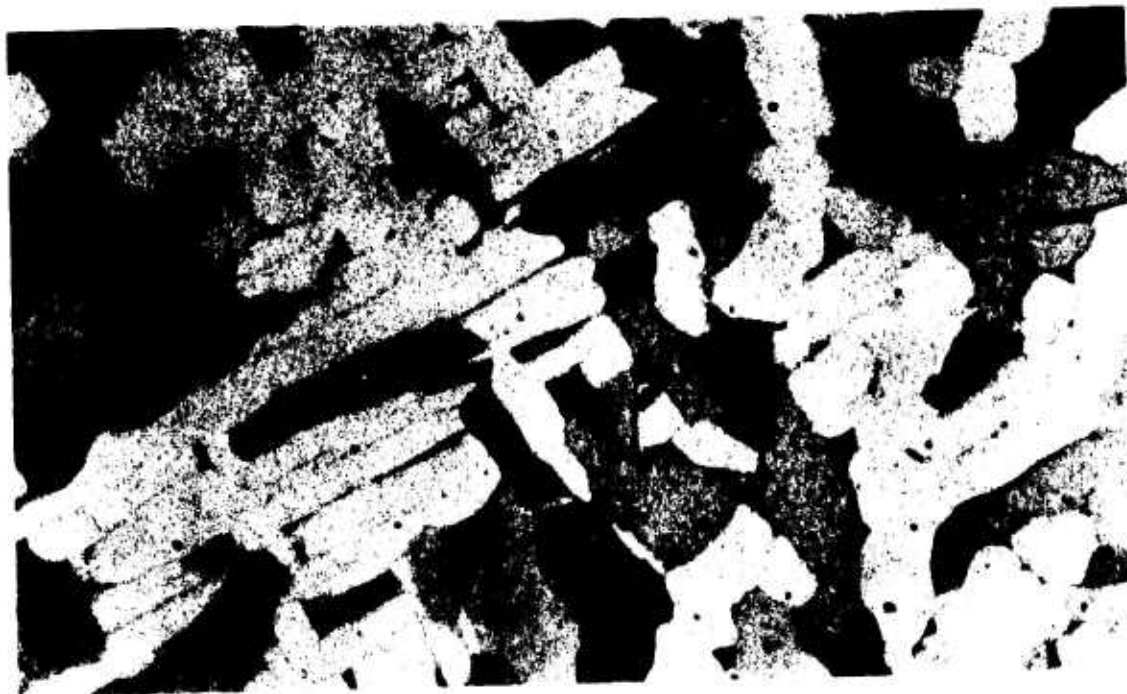
B4631   X1000

Fig. 27 - Ti-6Al-4V Condition 15, 2.4-in. plate, as-received
K_{Ic} = 48 ksi-in$^{\frac{1}{2}}$, F_{ty} = 121 ksi.

B4653   X1000

Fig. 28 - Ti-6Al-4V Condition 16, 2.4-in. plate, 1775°F-$\frac{1}{2}$ h-AC, 1450°F-
1 h-AC. K_{Ic} = 80 ksi, F_{ty} = 124 ksi.

Etchant: 10 pct aq. sol. of 49 pct conc. HBF$_4$, immersion for 1.5 to 2 min.

B4648   X1000

Fig. 29 - Ti-6Al-4V Condition 17, 4- X 4-in. forged billet, 1775°F-1 h-AC,
        1450°F-1 h-AC. K_{Ic} = 67 ksi-in., F_{ty} = 124 ksi.

B4634   X1000

Fig. 30 - Ti-6Al-4V Condition 18, 4- x 4-in. forged billet, 1750°F-1 h-AC,
        1450°F-1 h-AC. K_{Ic} = 68 ksi-in., F_{ty} = 125 ksi.

Etchant: 10 pct aq. sol. of 49 pct conc. HBF4, immersion for 1.5 to 2 min.

B4635   X1000

Fig. 31 - Ti-6Al-4V Condition 19, 4- X 4-in. forged billet, 1750°F-4 h-
AC, 1450°F-1 h-AC. K_{Ic} = 65 ksi-in$^{\frac{1}{2}}$, F_{ty} = 127 ksi.

B4636   X1000

Fig. 32 - Ti-6Al-4V Condition 20, 4- X 4-in. forged billet, 1750°F-$\frac{1}{2}$ h-WQ,
1000°F-2 h-AC. K_{Ic} = 56 ksi-in$^{\frac{1}{2}}$, F_{ty} = 144 ksi.

Etchant: 10 pct aq. sol. of 49 pct conc. HBF$_4$, immersion for 1.5 to 2 min.

60

B4637   X1000

Fig. 33 - Ti-6Al-4V Condition 21, 4- X 4-in. forged billet, 1750°F-2 h-
         WQ, 1000°F-2 h-AC. K_{Ic} = 51 ksi-in$^{\frac{1}{2}}$, F_{ty} = 147 ksi.

B4648   X1000

Fig. 34 - Ti-6Al-4V Condition 22, 4- X 4-in. forged billet, 1750°F-4 h-WQ,
         1000°F-2 h-AC. K_{Ic} = 55 ksi-in$^{\frac{1}{2}}$, F_{ty} = 144 ksi.

Etchant: 10 pct aq. sol. of 49 pct conc. HBF$_4$, immersion for 1.5 to 2 min.
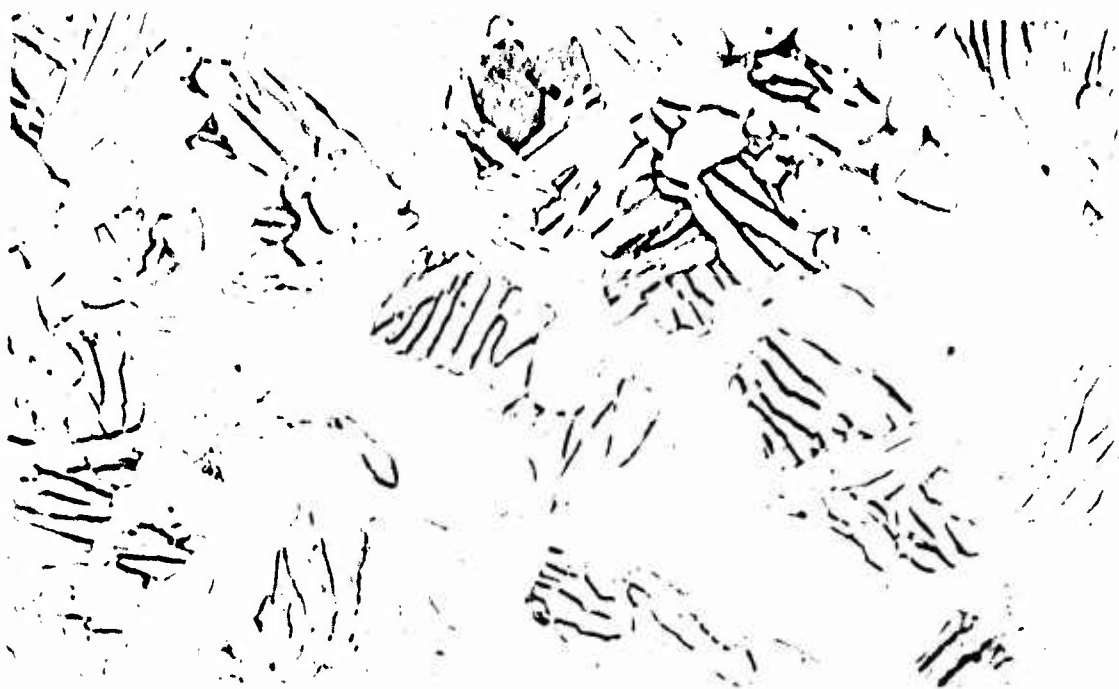
B4644 X1000

Fig. 35 - Ti-6Al-4V Condition 27, 4- X 4-in. forged billet,
α-segregated, equiaxed, $1775^{O}F-\frac{1}{2}$ h-AC, $1450^{O}F$-1 h-AC.
$K_{Ic} = 72$ ksi-in$^{\frac{1}{2}}$, $F_{ty} = 130$ ksi.

B4645 X1000

Fig. 36 - Ti-6Al-4V Condition 28, 4- X 4-in. forged billet, α-segregated,
equiaxed, $1750^{O}F-\frac{1}{2}$ h-WQ, $1000^{O}F$-2 h-AC. $K_{Ic} = 66$ ksi-in$^{\frac{1}{2}}$,
$F_{ty} = 138$ ksi.

Etchant: 10 pct aq. sol. of 49 pct conc. HBF$_4$, immersion for 1.5 to 2 min.
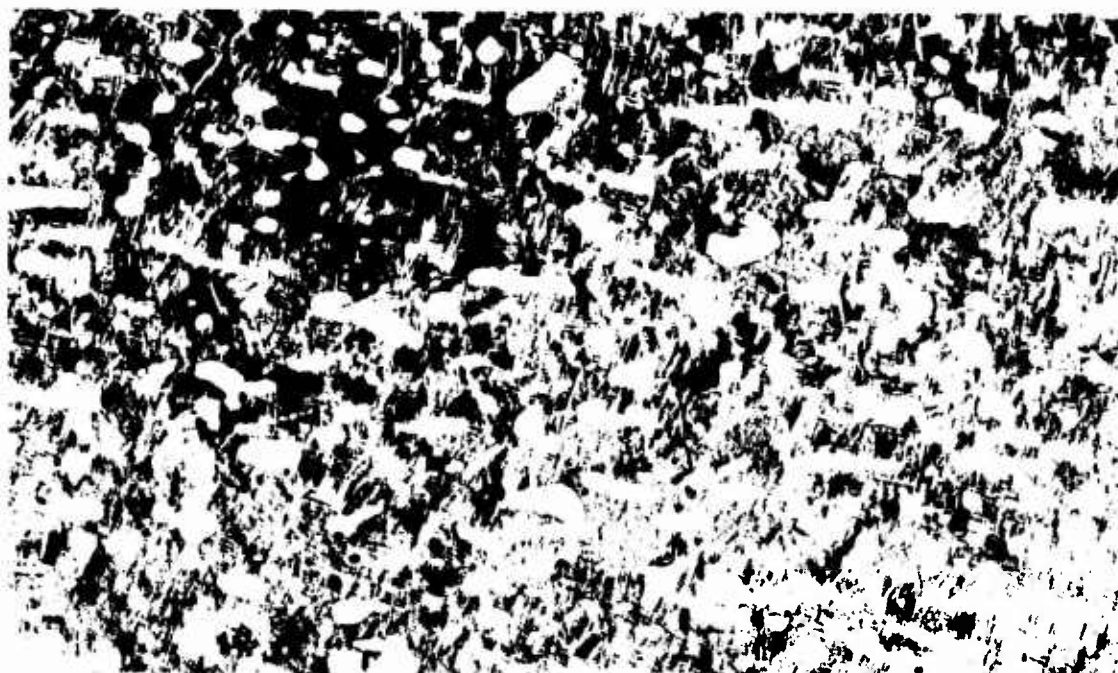
B4677   X200

B4678   X200

Fig. 37 - Comparison of normal microstructure (Condition 18, top) with
          α-segregated microstructure (Condition 28, bottom) of
          4- X 4-in. forged billets of Ti-6Al-4V alloy.

Etchant: 10 pct aq. sol. of 49 pct conc. HBF$_4$, immersion for 1.5 to
         2 min.

F1311

F1307

F1310   X80,000

Fig. 38 - Condition 1, 1-in. plate, as received (1725°F-1 h-AC, 1450°F-
1 h-AC. Top - bright field electron micrograph showing highly
dislocated transition structure between β (white ribs) and α.
Center - Dark field image with $(\overline{1}010)_\alpha$. Bottom - Dark field
image with $(\overline{1}011)_\alpha$.
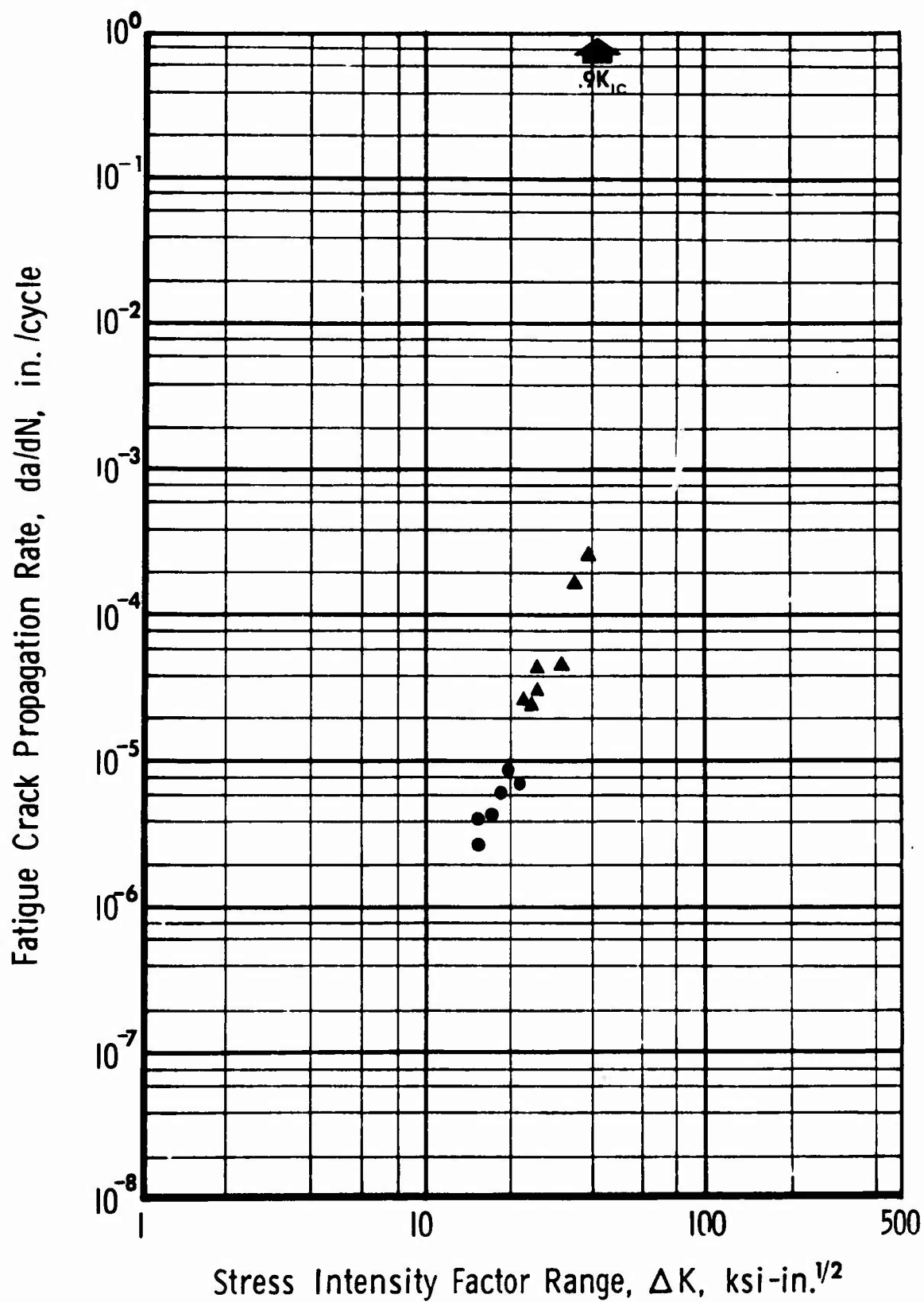
Fig. 39 Ti-6Al-4V Condition 1, 1-in. plate, as-received (1725°F-1 h-AC, 1450°F-1 h-AC).
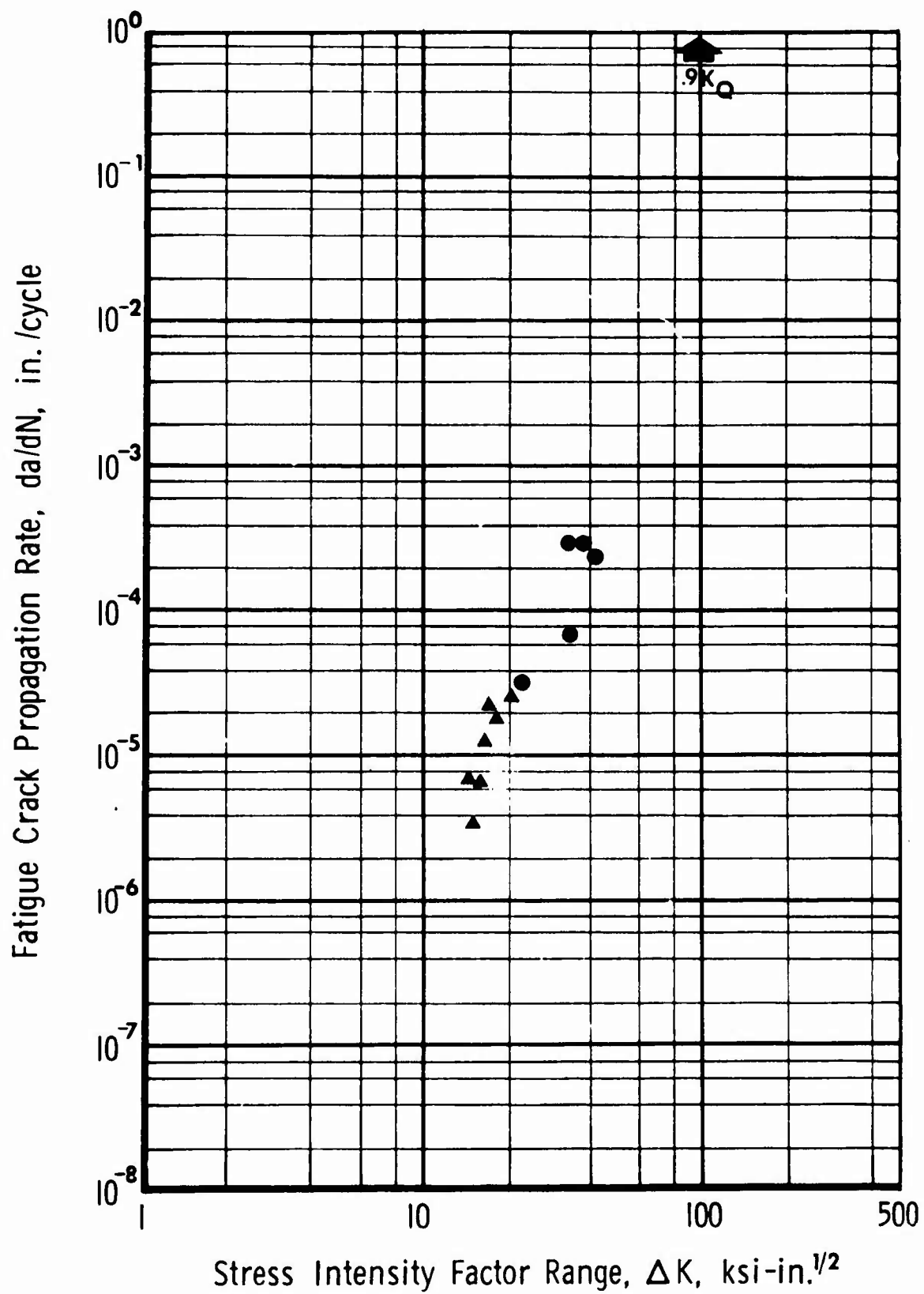
Fig. 40 Ti-6Al-4V Condition 2, 1-in. plate, 1775°F-½ h-AC, 1450°F-1 h-AC.
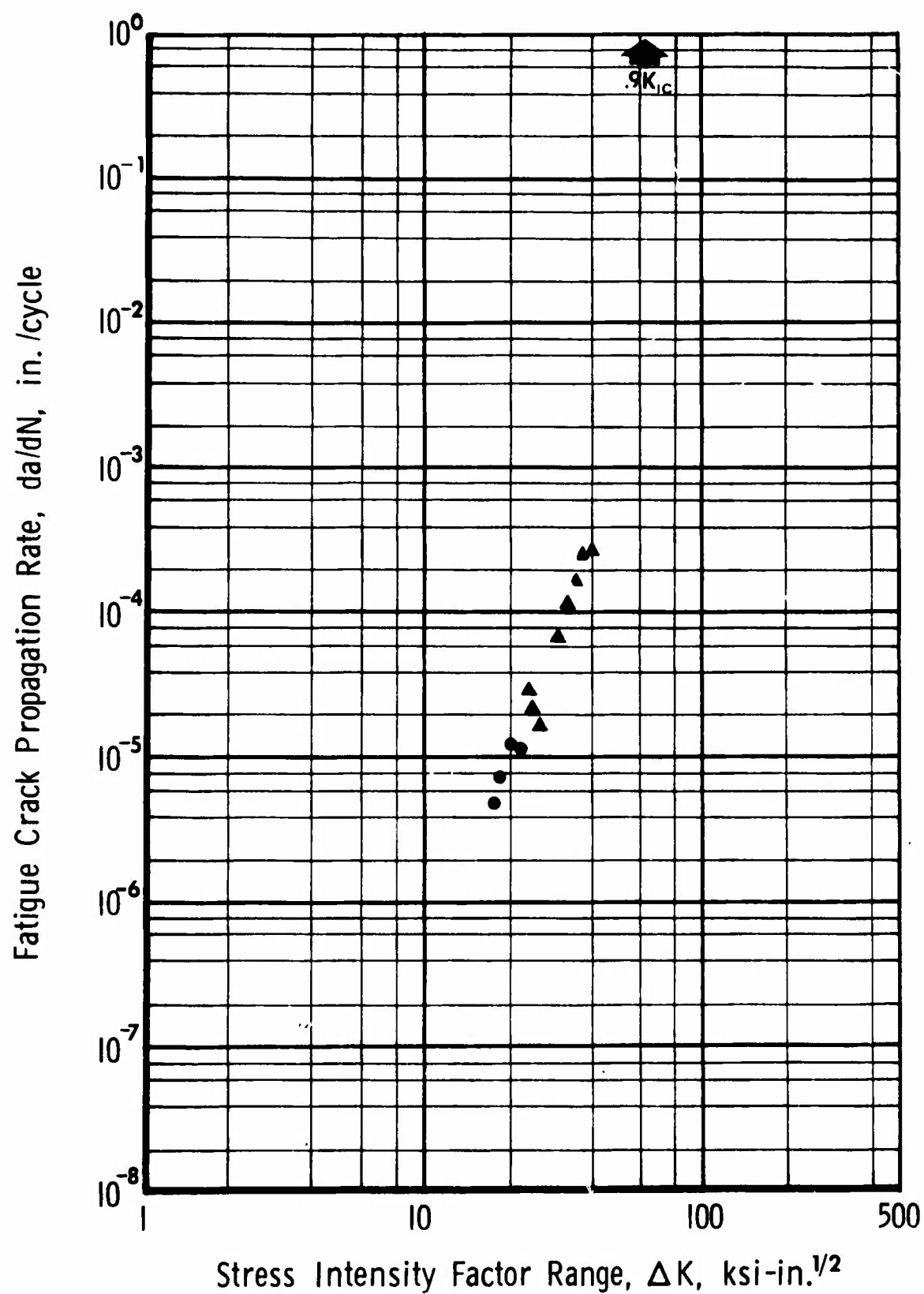
Fig. 41   Ti-6Al-4V Condition 3, 1-in. plate, 1750°F-1 h-AC, 1450°F-1 h-AC.
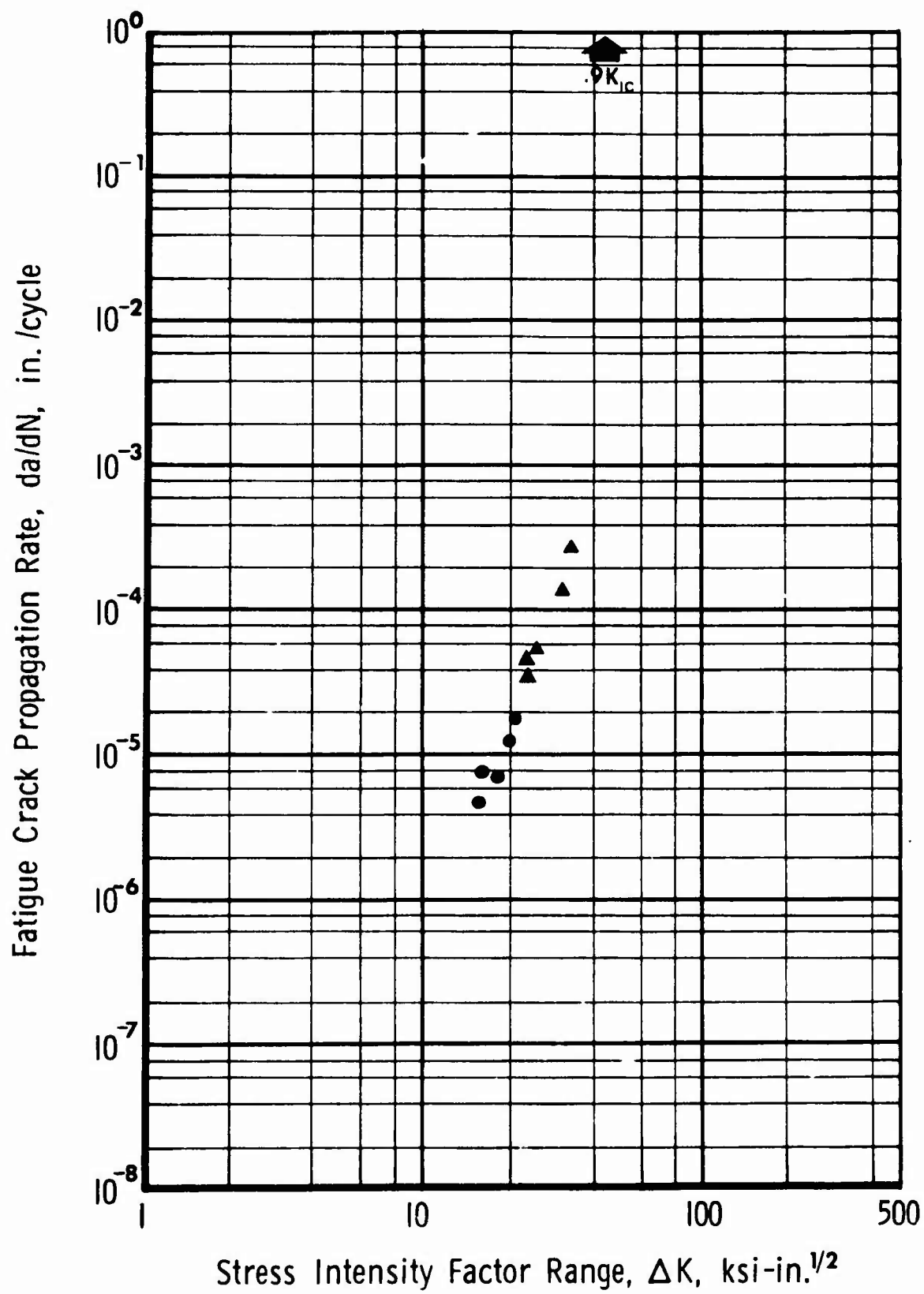
Fig. 42 Ti-6Al-4V Condition 4, 1-in. plate, 1750°F-½ h-WQ, 1000°F-2 h-AC.
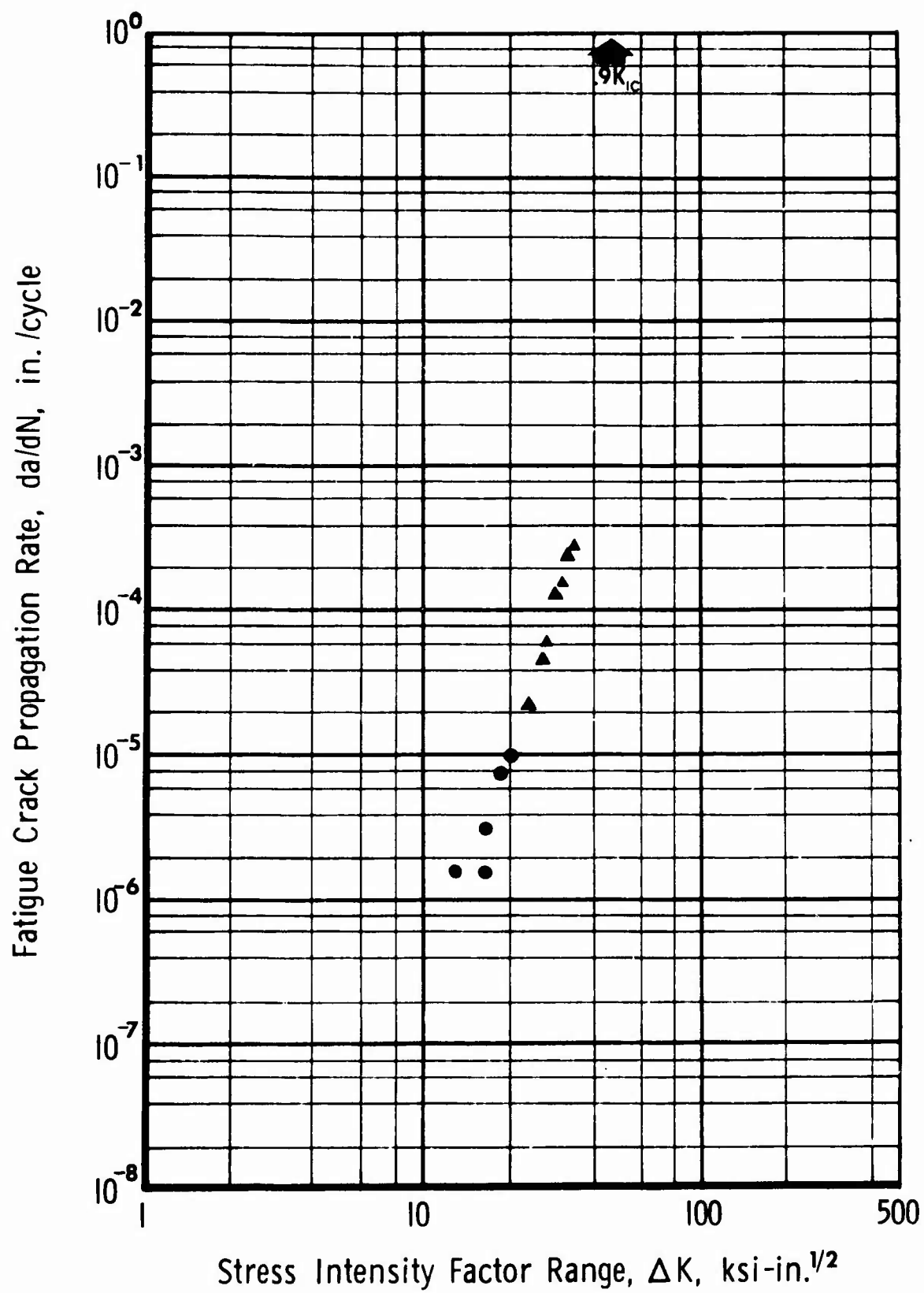
Fig. 43 Ti-6Al-4V Condition 5, 1-in. plate, 1750°F-2 h-WQ, 1000°F-2 h-AC.
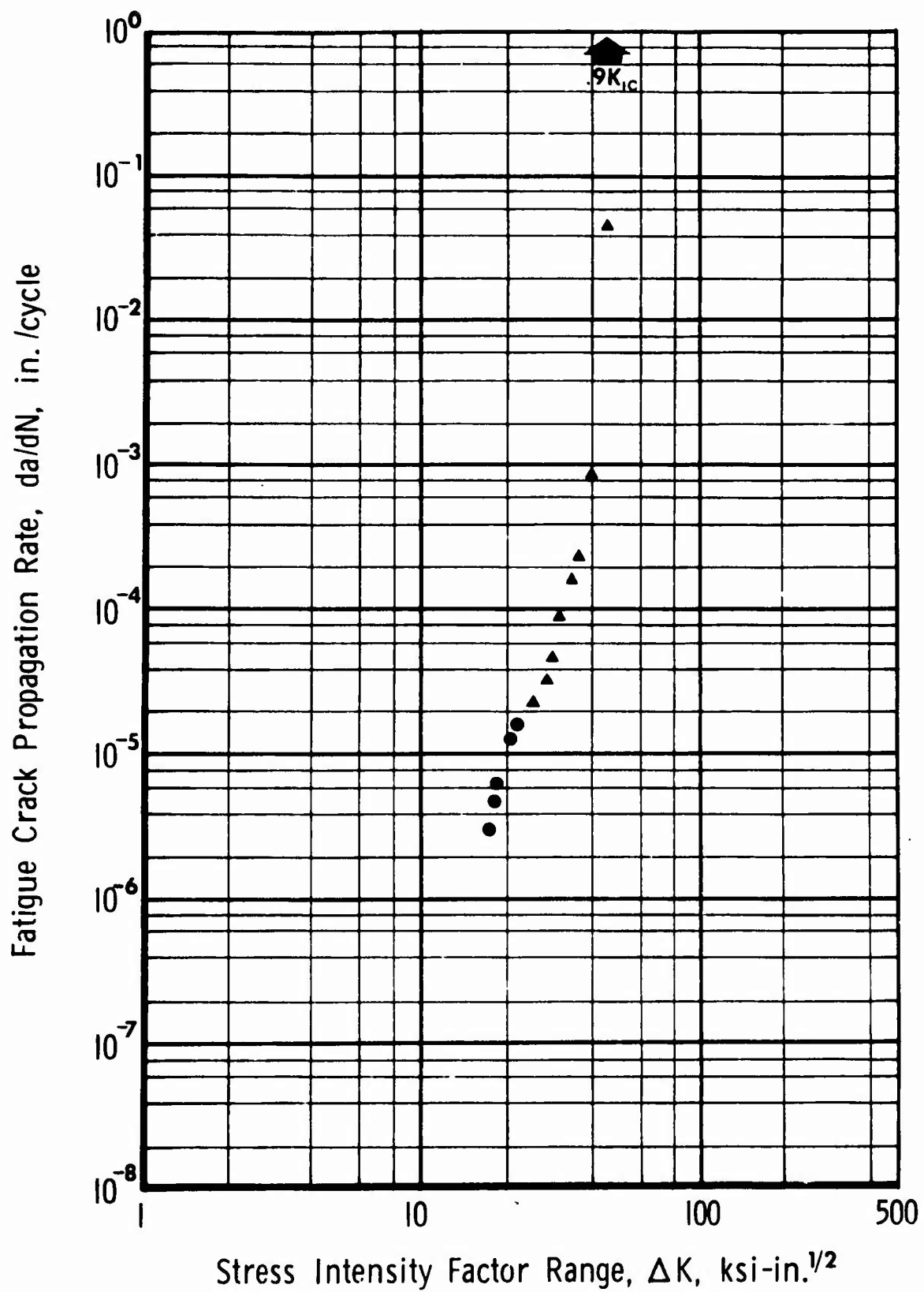
Fig. 44 Ti-6Al-4V Condition 6, 1-in. plate, 1750°F-4 h-WQ, 1000°F-2 h-AC.

79
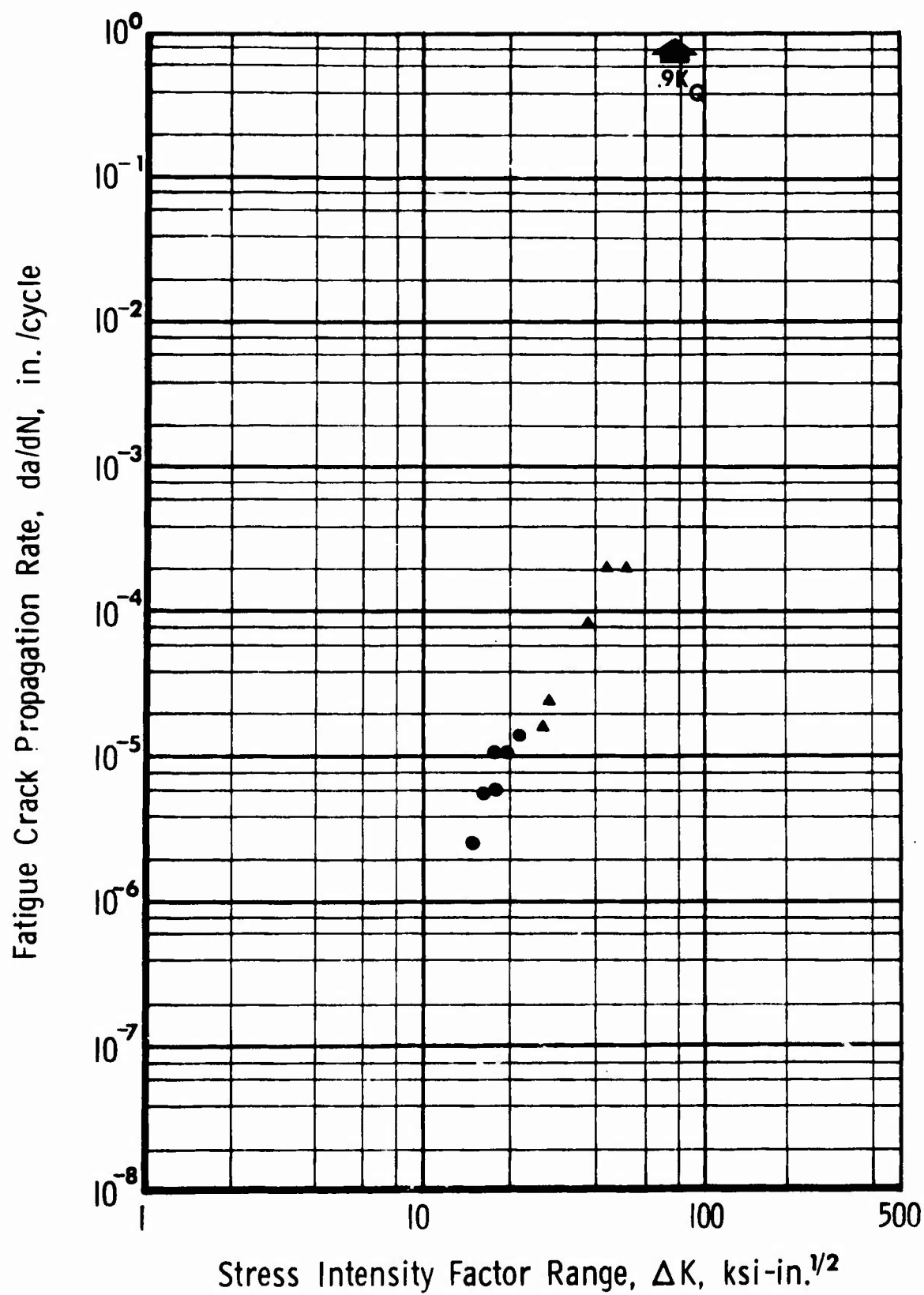
Fig. 45   Ti-6Al-4V Condition 7, 1-in. plate, 1850°F-½h-AC, 1775°F-½ h-AC, 1450°F-1 h-AC.
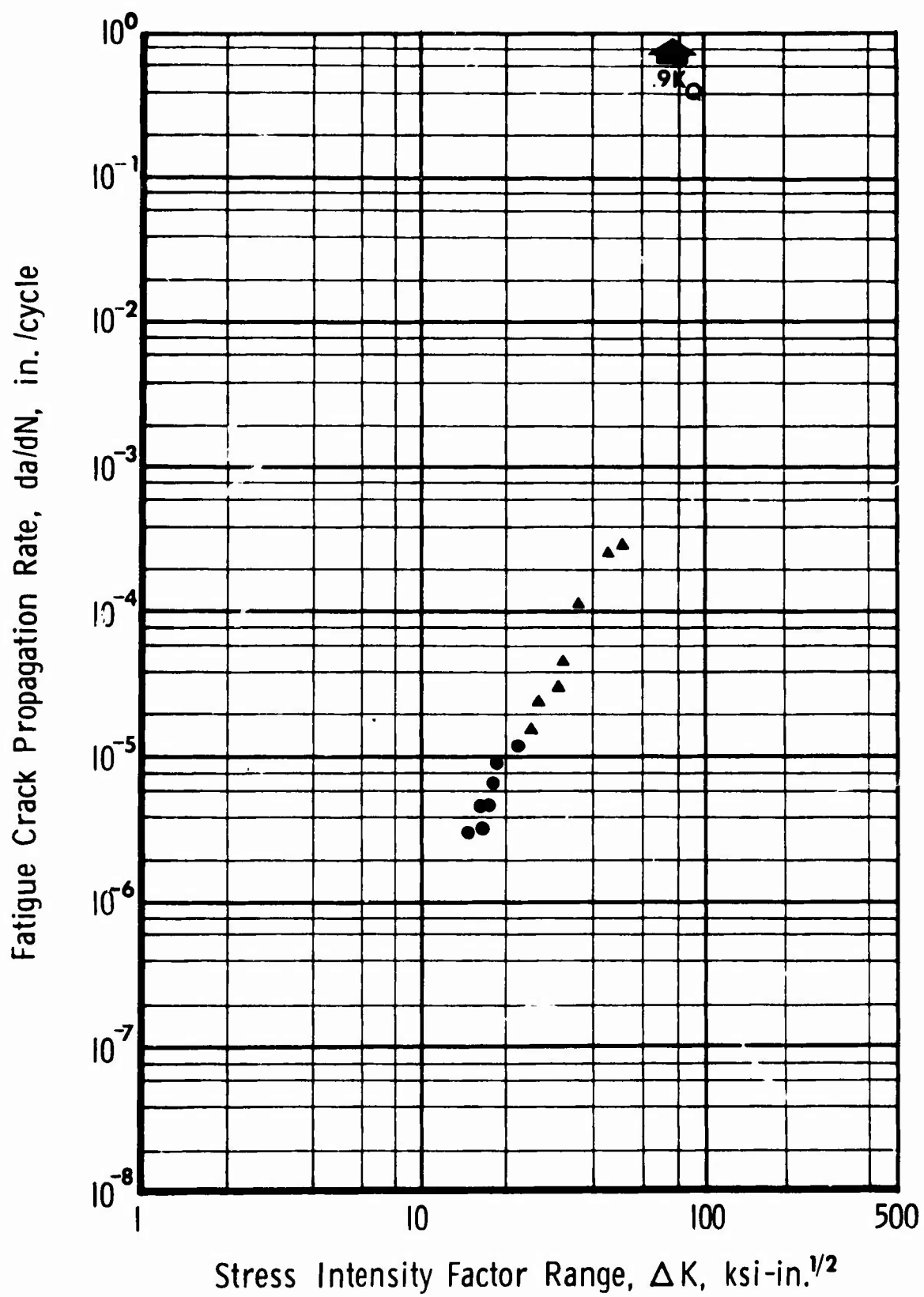
Fig. 46 Ti-6Al-4V Condition 8, 1-in. plate, $1850^\circ F\text{-}\frac{1}{2}$ h-AC, $1750^\circ F\text{-}2$ h-AC, $1450^\circ F\text{-}1$ h-AC.
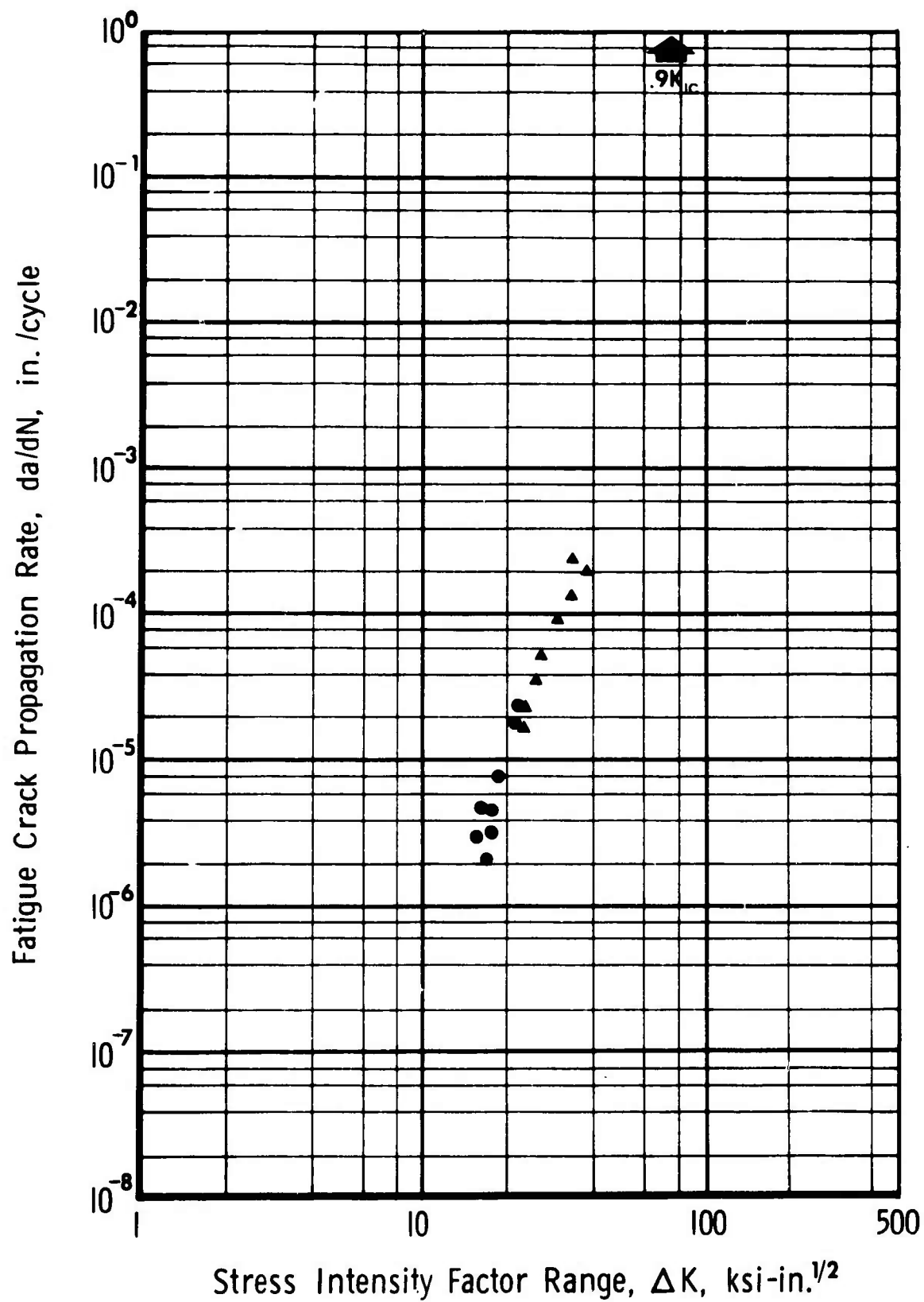
Fig. 47 Ti-6Al-4V Condition 9, 1-in. plate, 1850°F-$\frac{1}{2}$ h-AC, 1750°F-4 h-AC, 1450°F-1 h-AC.
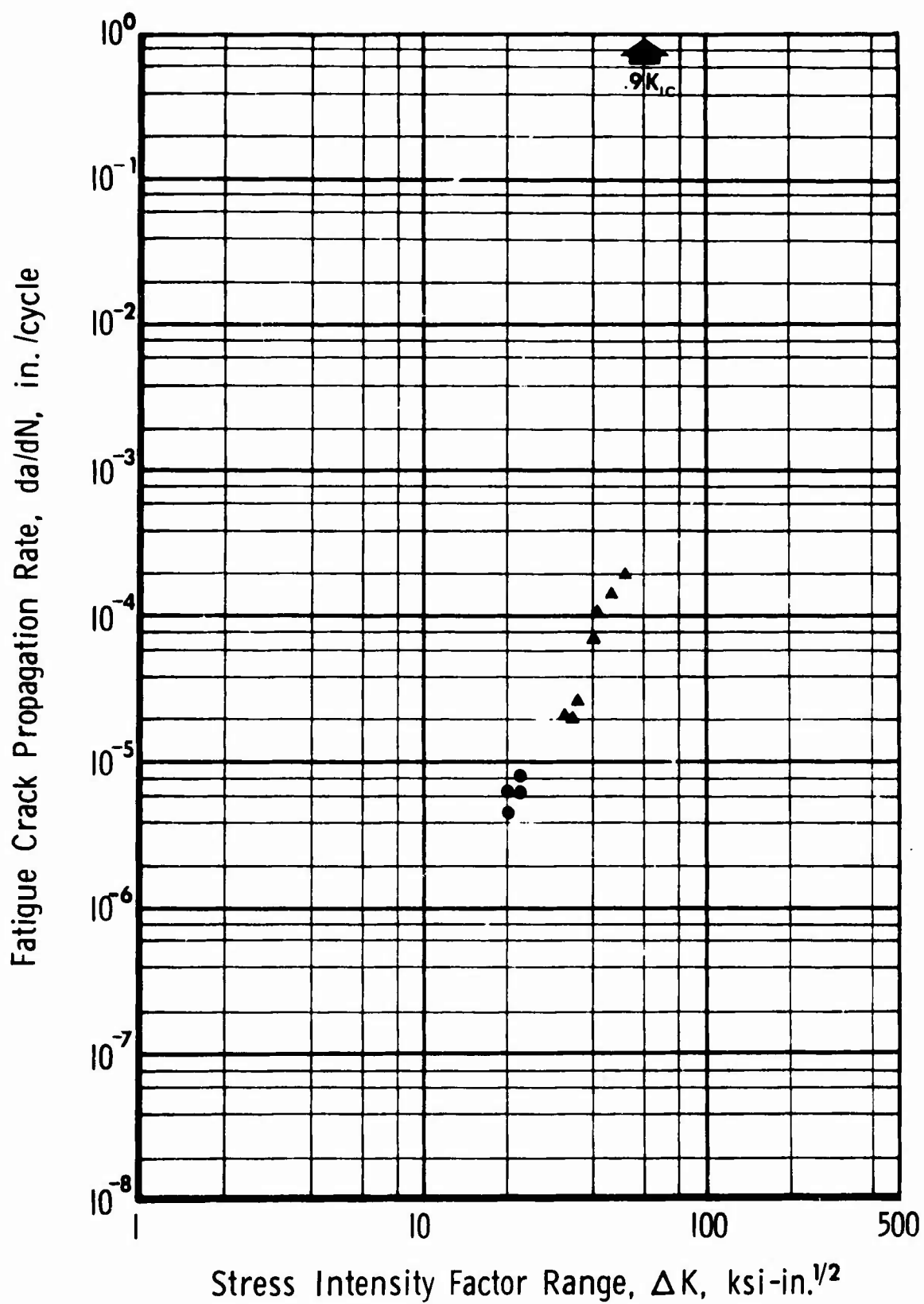
Fig. 48 Ti-6Al-4V Condition 10, 1-in. plate, $1850°F-\frac{1}{2}$ h-AC, $1750°F-\frac{1}{2}$ h-WQ, $1000°F$-2 h-AC.
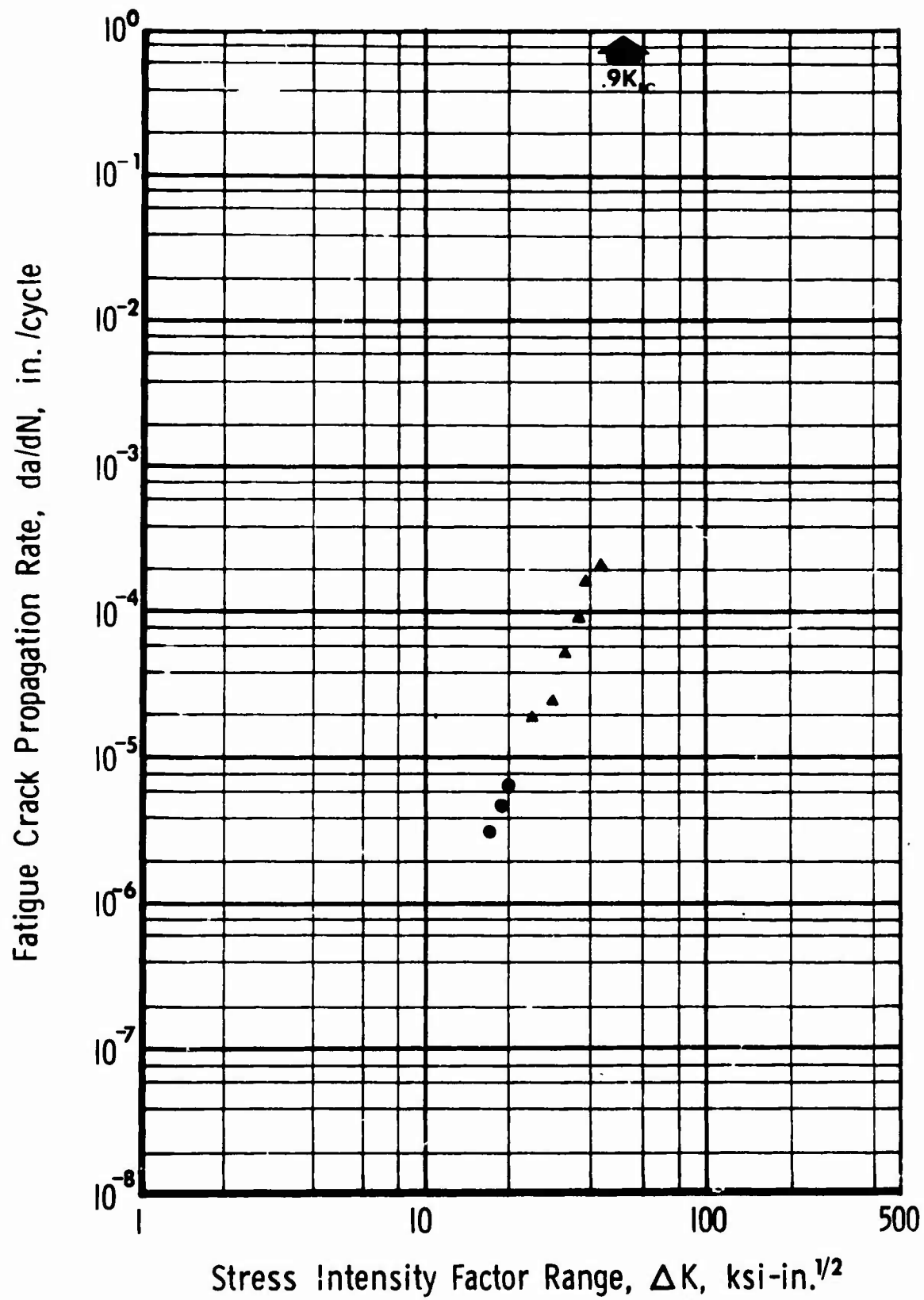
Fig. 49 Ti-6Al-4V Condition 11, 1-in. plate, 1850°F-½ h-AC, 1750°F-2 h-WQ, 1000°F-2 h-AC.
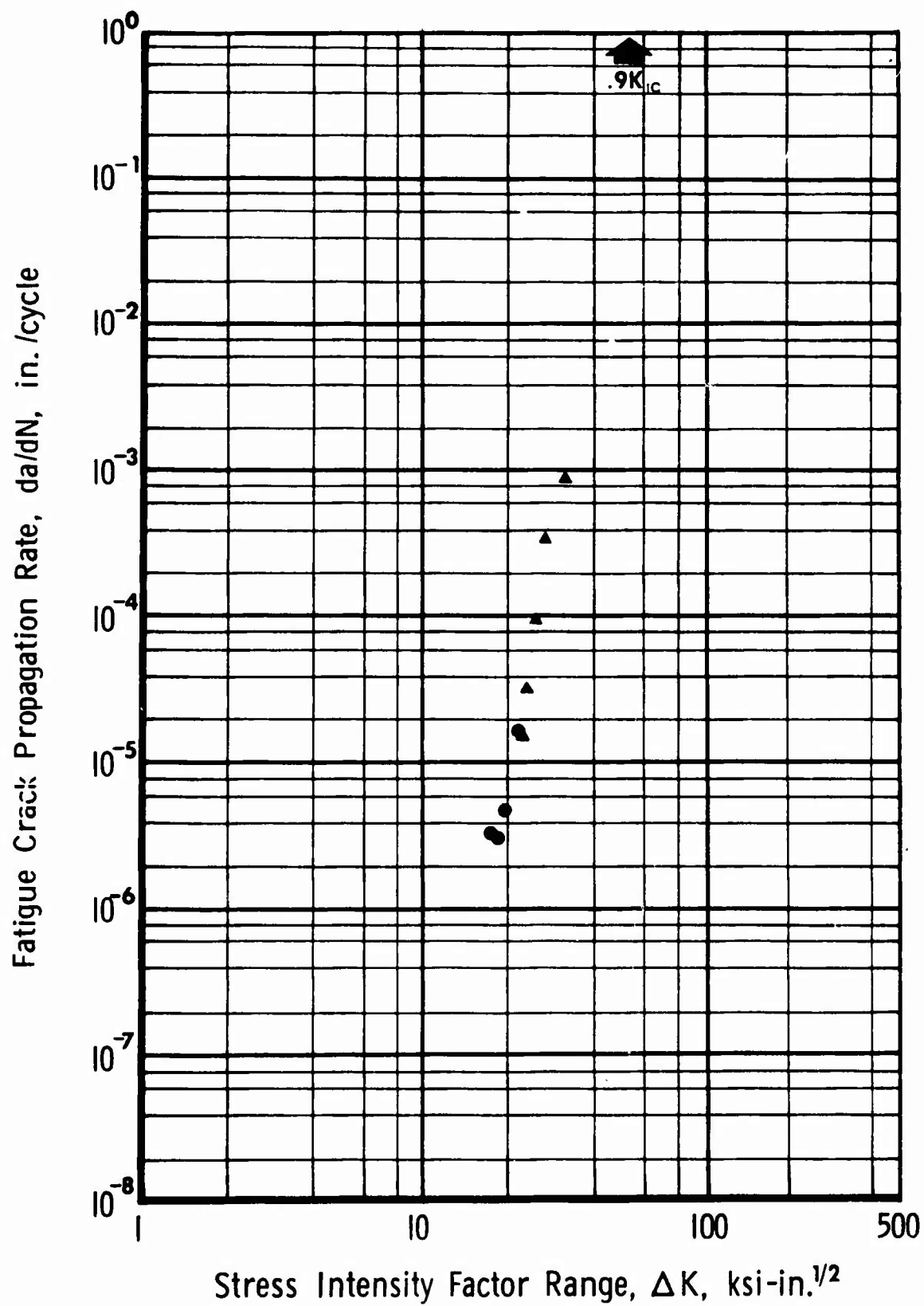
Fig. 50 Ti-6Al-4V Condition 12, 1-in. plate, 1850°F-½ h-AC, 1750°F-4 h-WQ, 1000°F-2 h-AC.
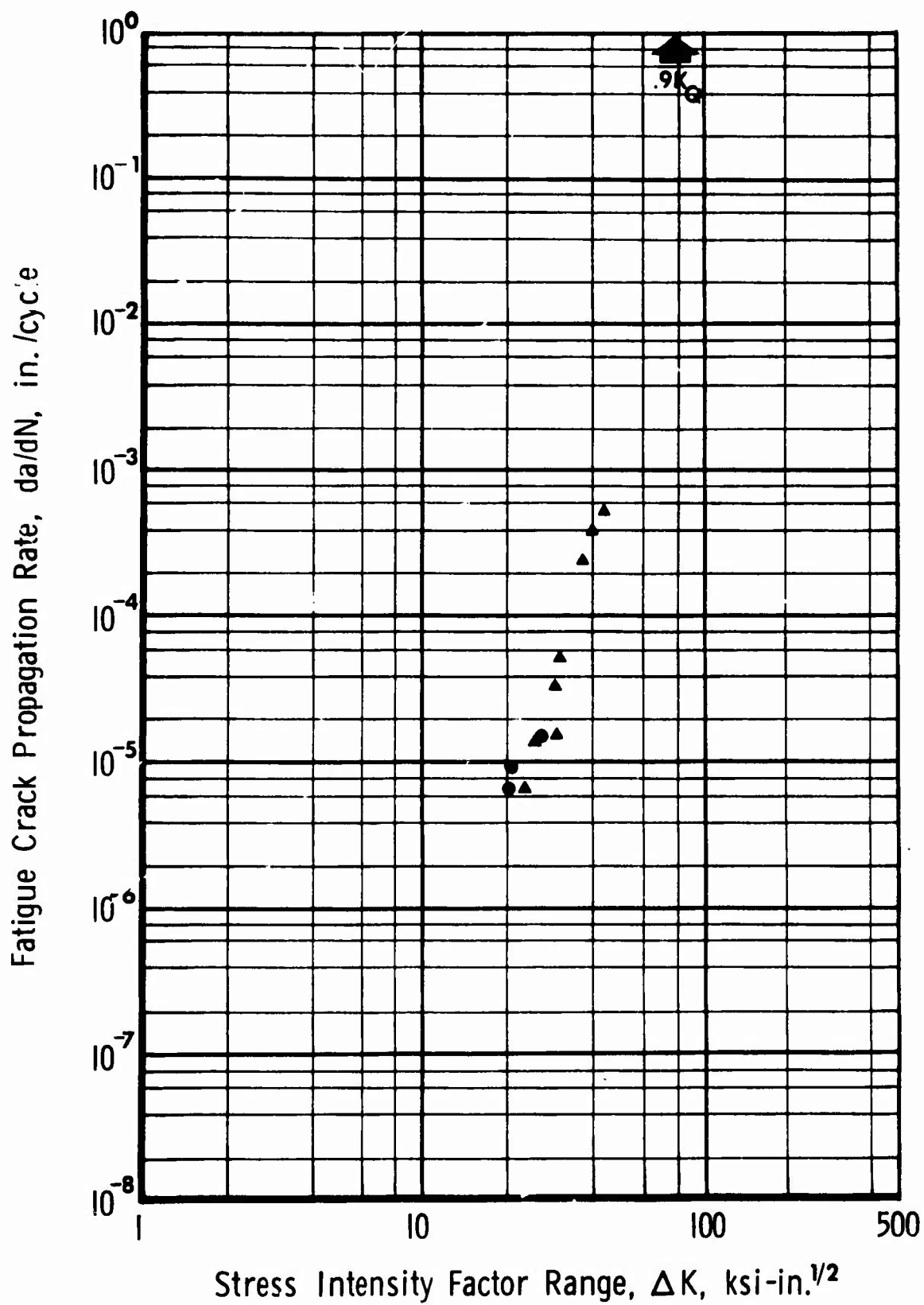
Fig. 51 Ti-6Al-4V Condition 13, 1-in. plate, 1875°F-½ h-AC, 1750°F-2 h-AC, 1450°F-1 h-AC.

86
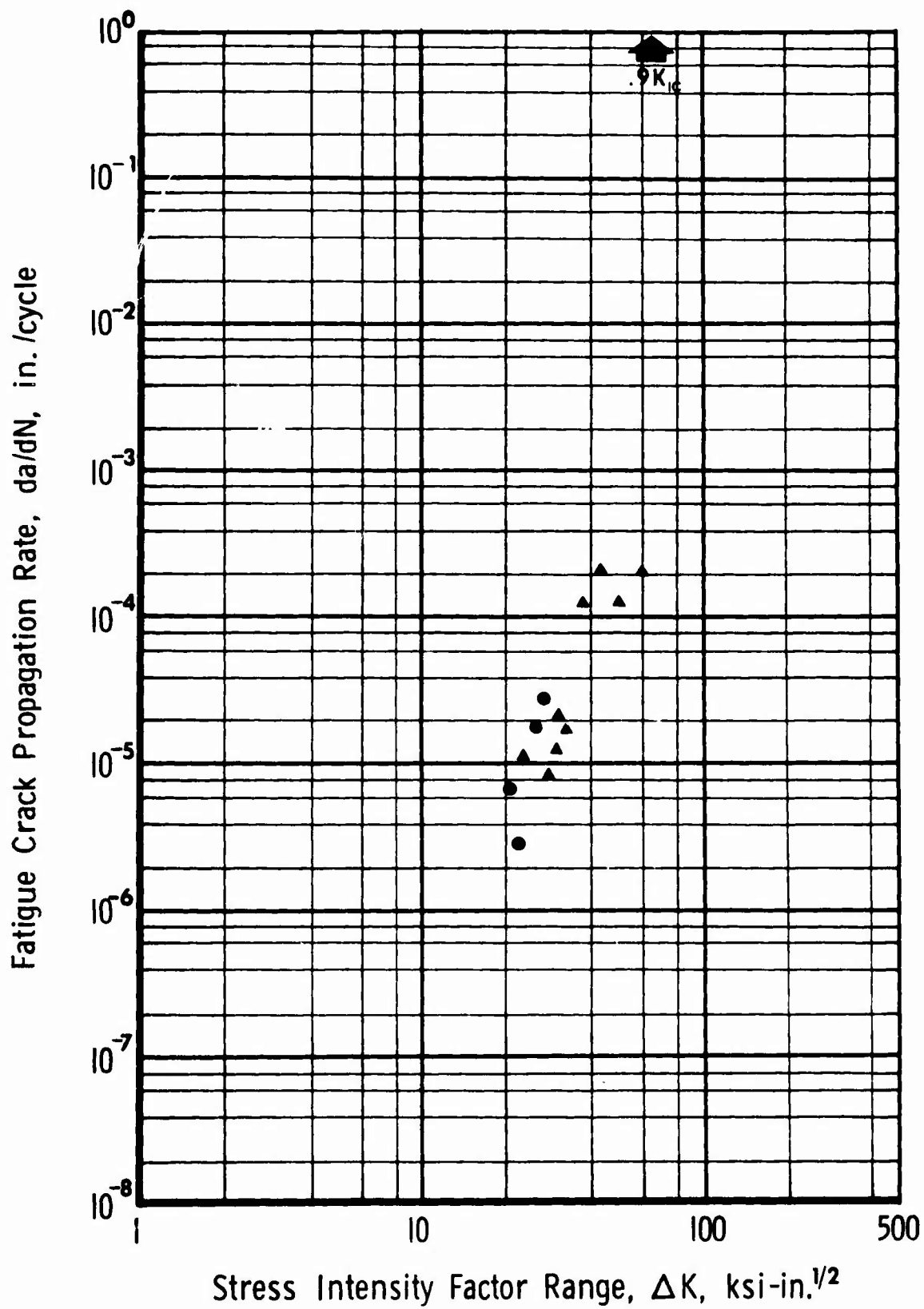
Fig. 52 Ti-6Al-4V Condition 14, 1-in. plate, 1875°F-½ h-AC, 1750°F-2 h-WQ, 1000°F-2 h-AC.
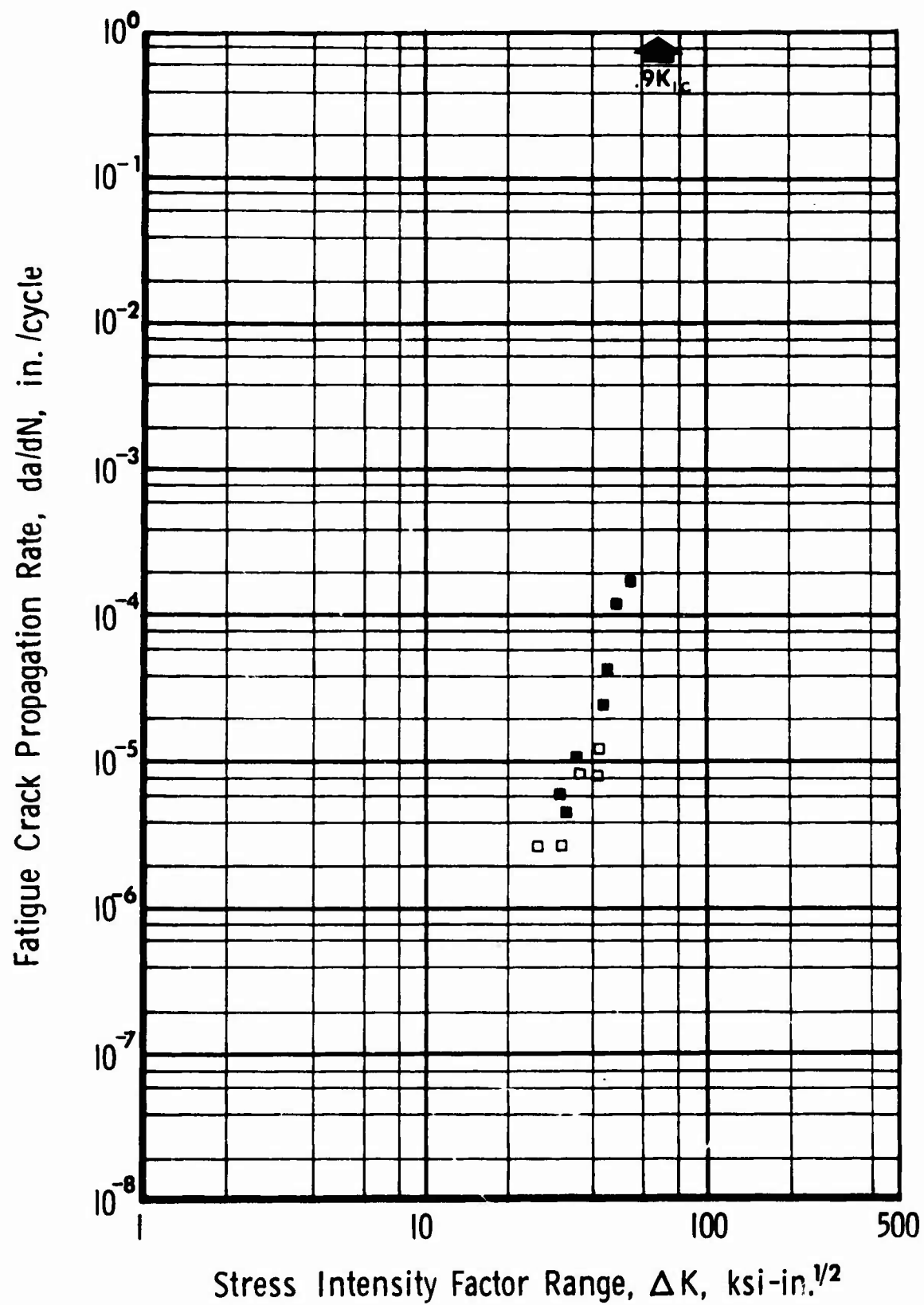
Fig. 53 Ti-6Al-4V Condition 23, 1-in. plate, 1850°F-$\frac{1}{2}$ h-IBQ.

83
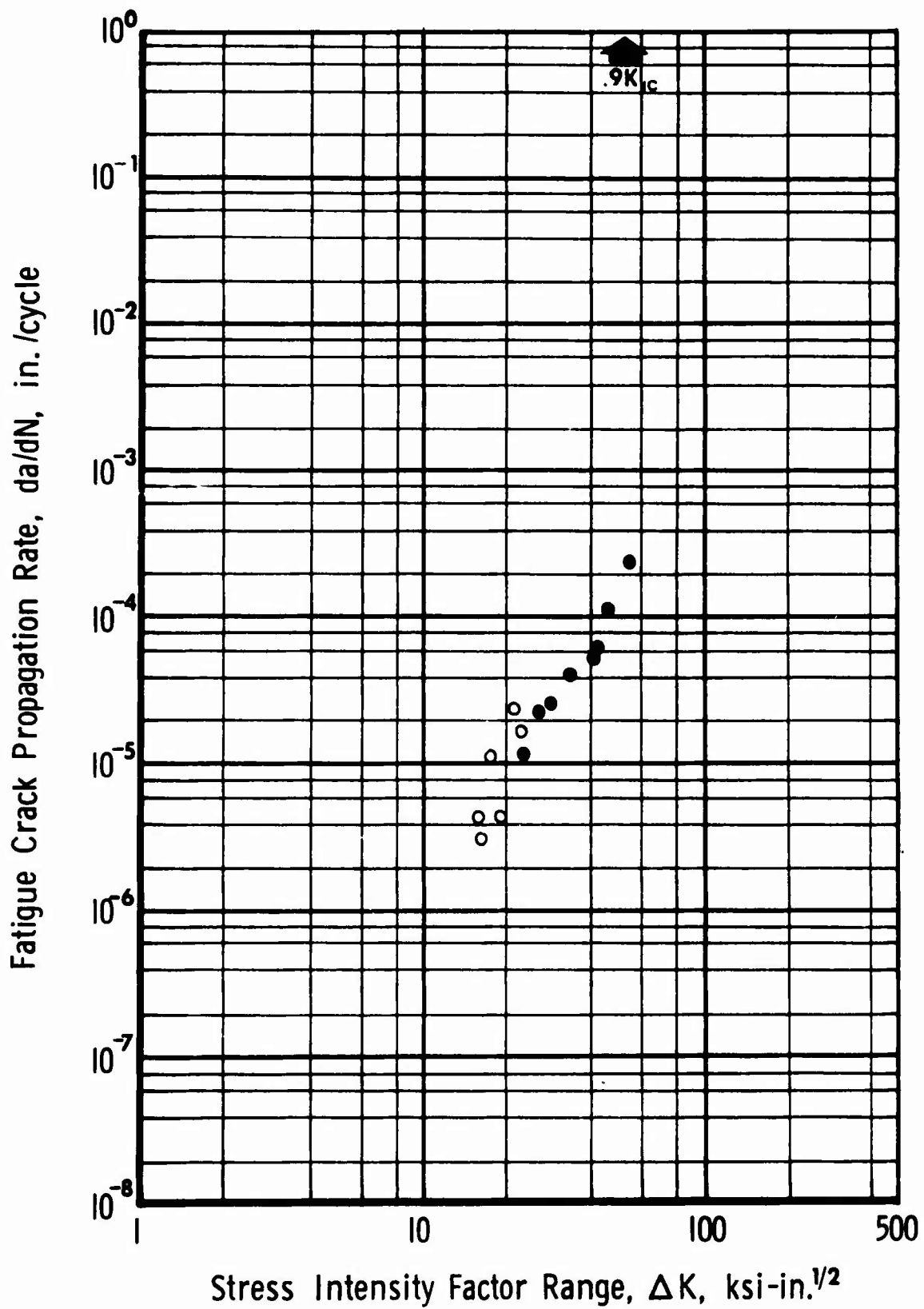
Fig. 54 Ti-6Al-4V Condition 24, 1-in. plate, 1850°F-½ h-IBQ, 1450°F-1 h-AC.
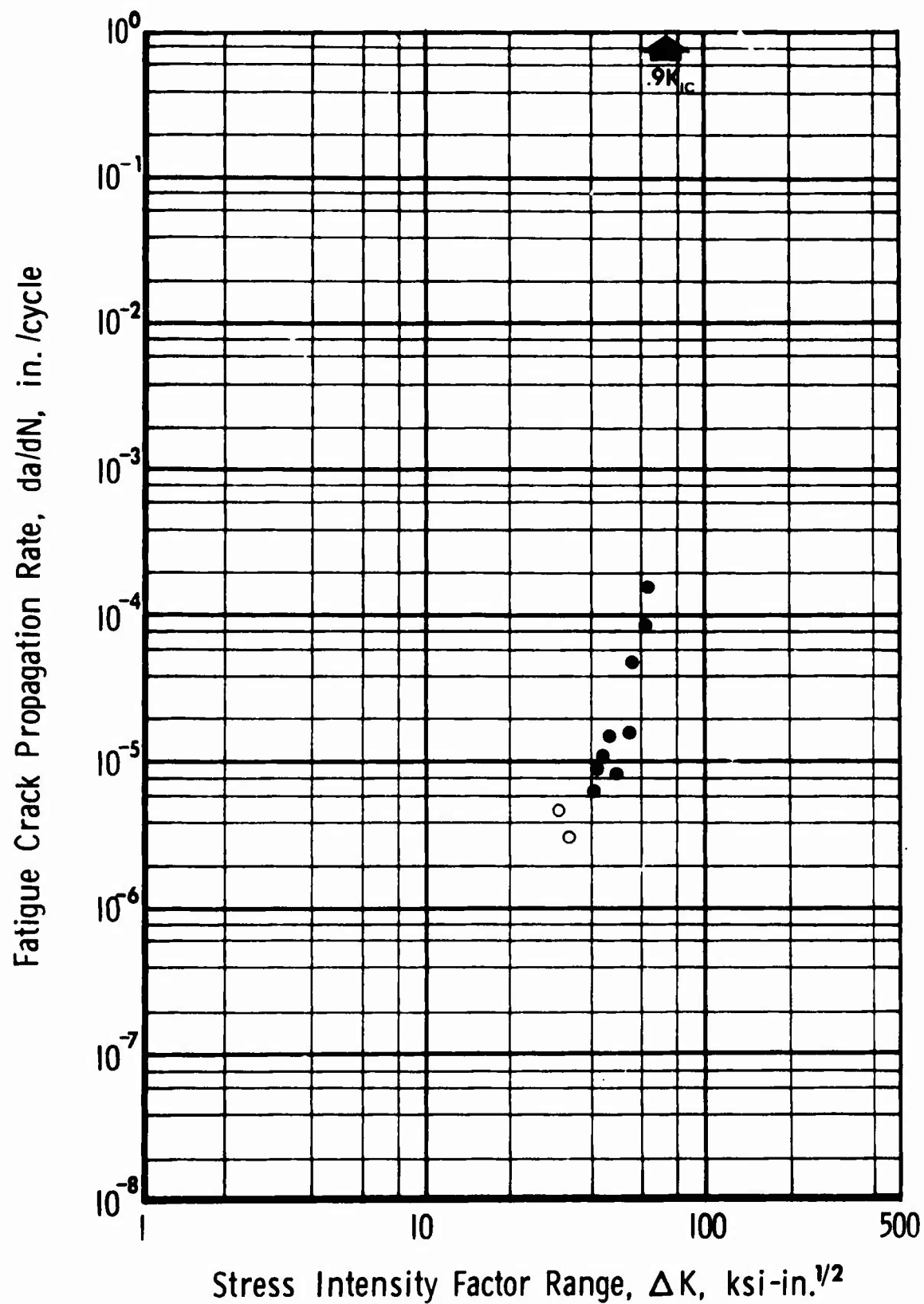
Fig. 55   Ti-6Al-4V Condition 25, 1-in. plate, 1875°F-$\frac{1}{2}$ h-IBQ.
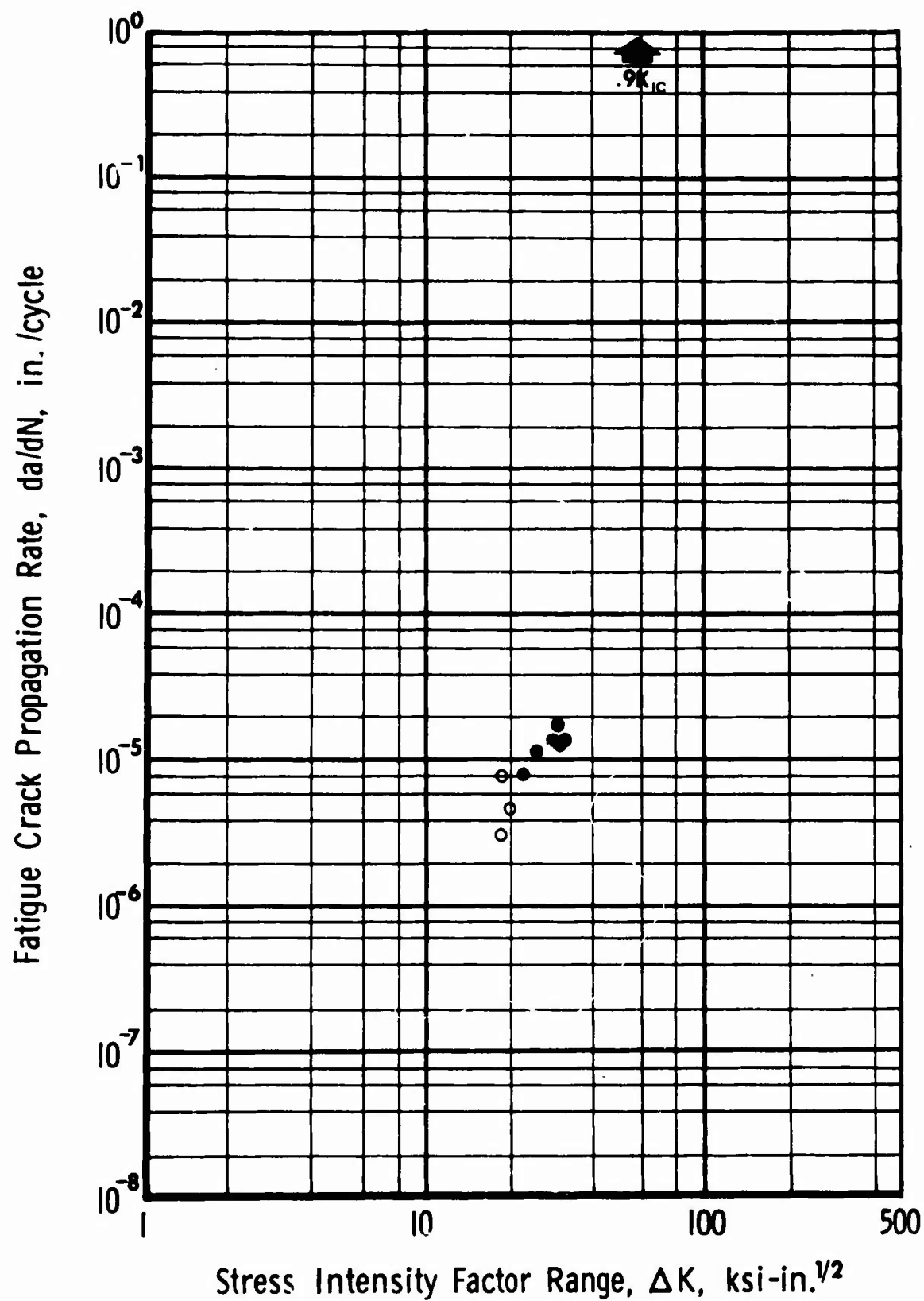
Fig. 56 Ti-6Al-4V Condition 26, 1-in. plate, 1875°F-$\frac{1}{2}$ h-IBQ, 1450°F-1 h-AC.

91
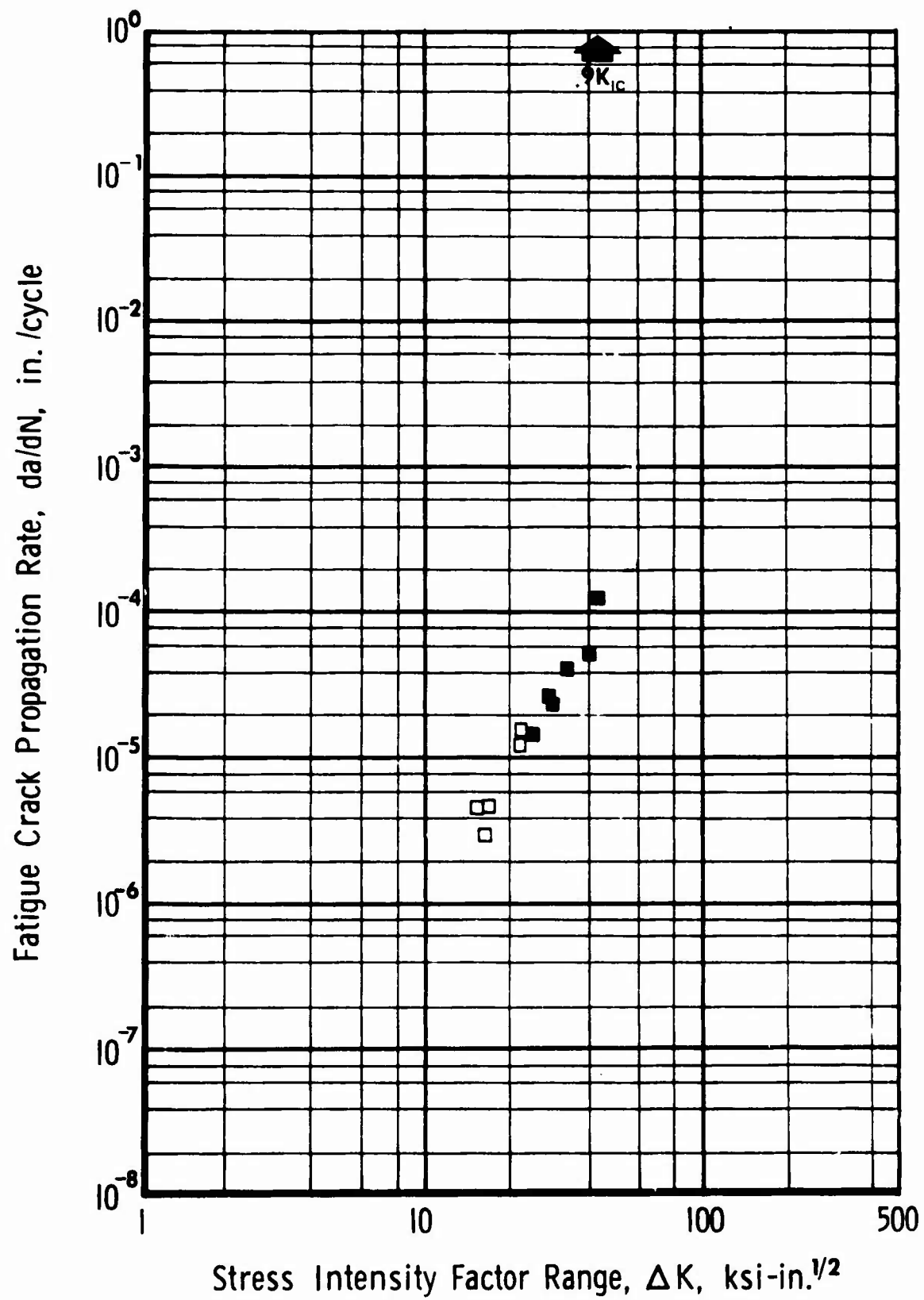
Fig. 57 Ti-6Al-4V Condition 15, 2.4-in. plate, as-received.
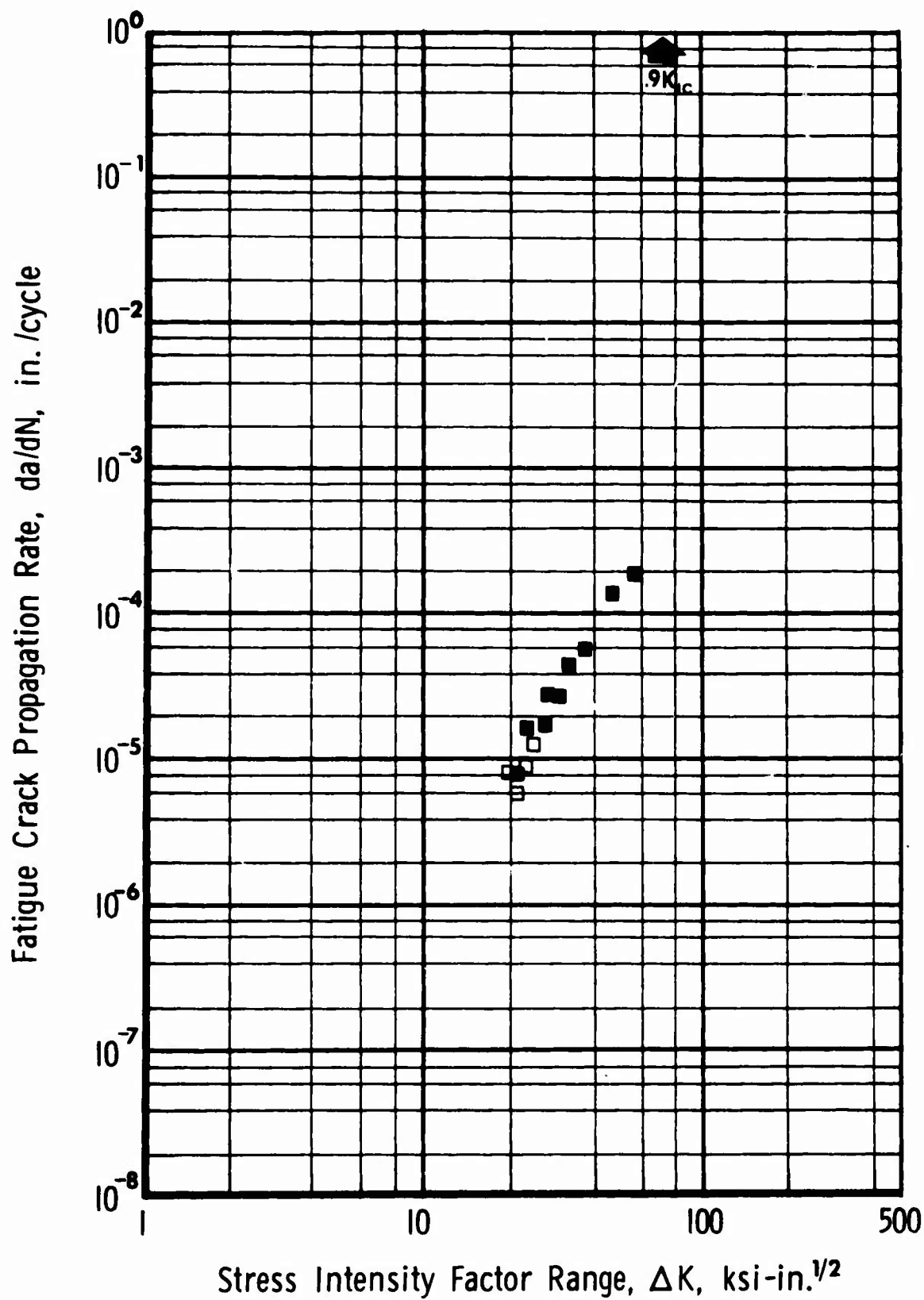
Fig. 58 Ti-6Al-4V Condition 16, 2.4-in. plate, 1775°F-½ h-Ac, 1450°F-1 h-AC.

93
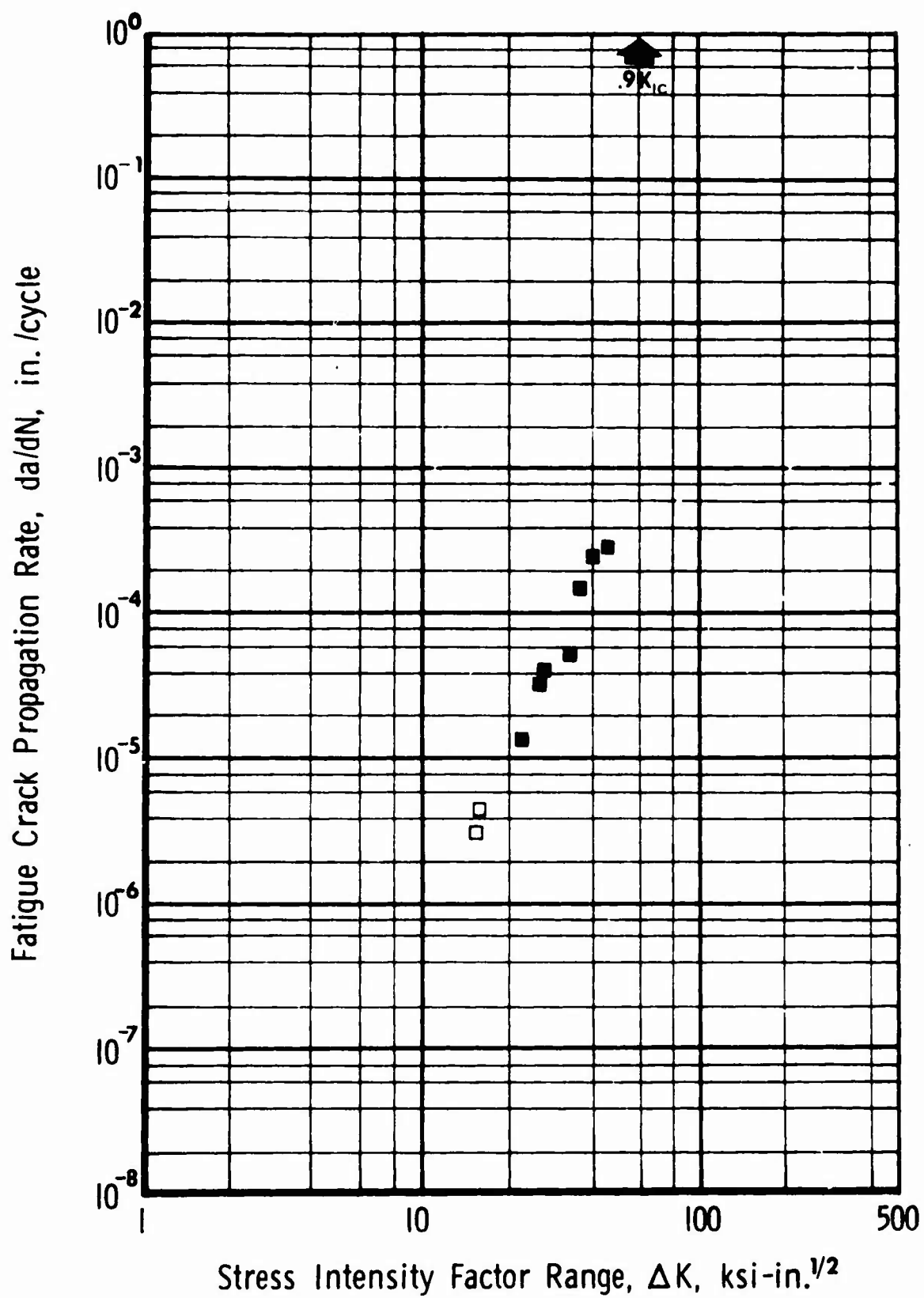
Fig. 59 Ti-6Al-4V Condition 17, 4- x 4-in. forged billet, 1775°F-½ h-AC, 1450°F-1 h-AC.
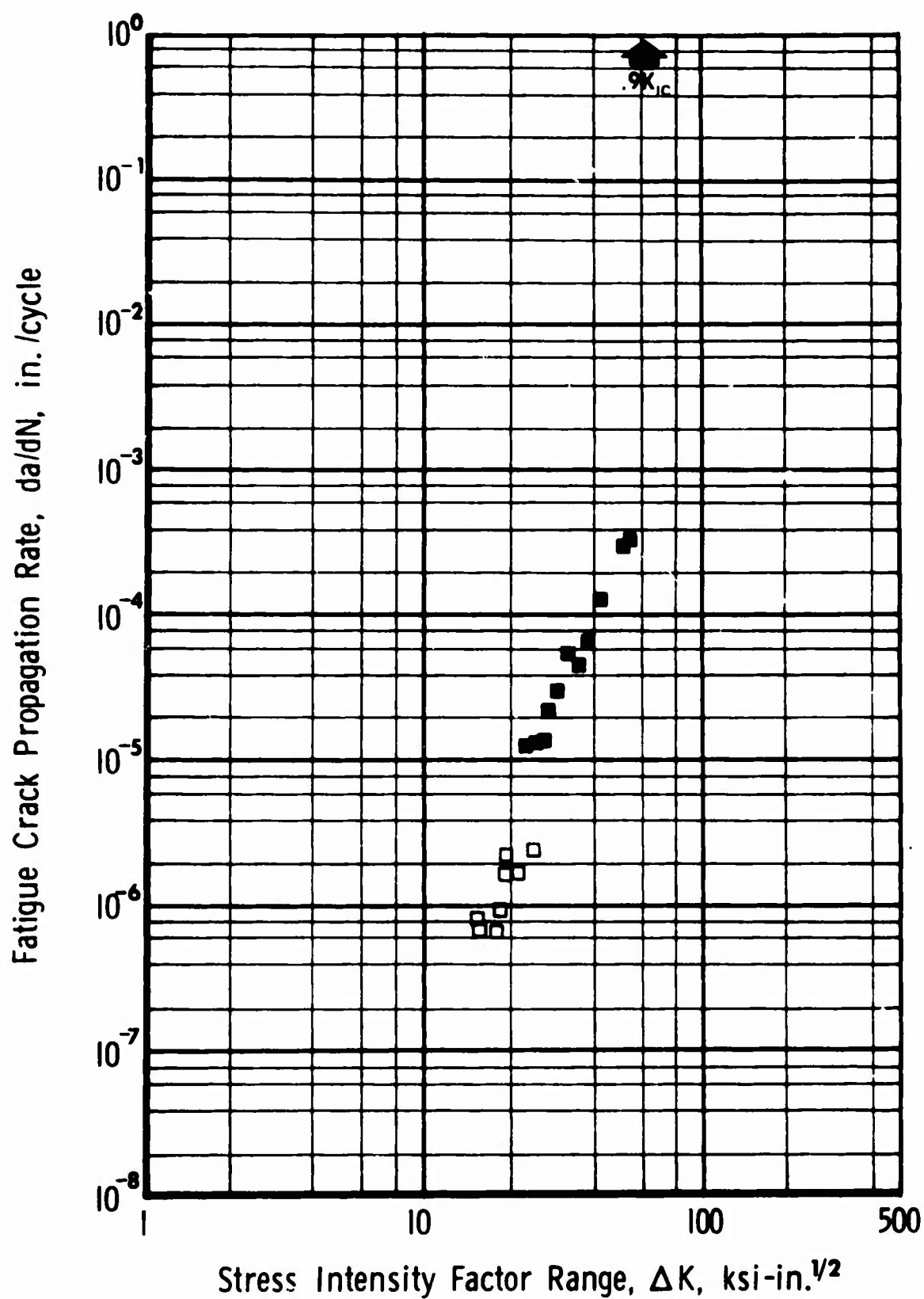
Fig. 60 Ti-6Al-4V Condition 18, 4- x 4-in. forged billet, 1750°F-2 h-AC, 1450°-1 h-AC.

95
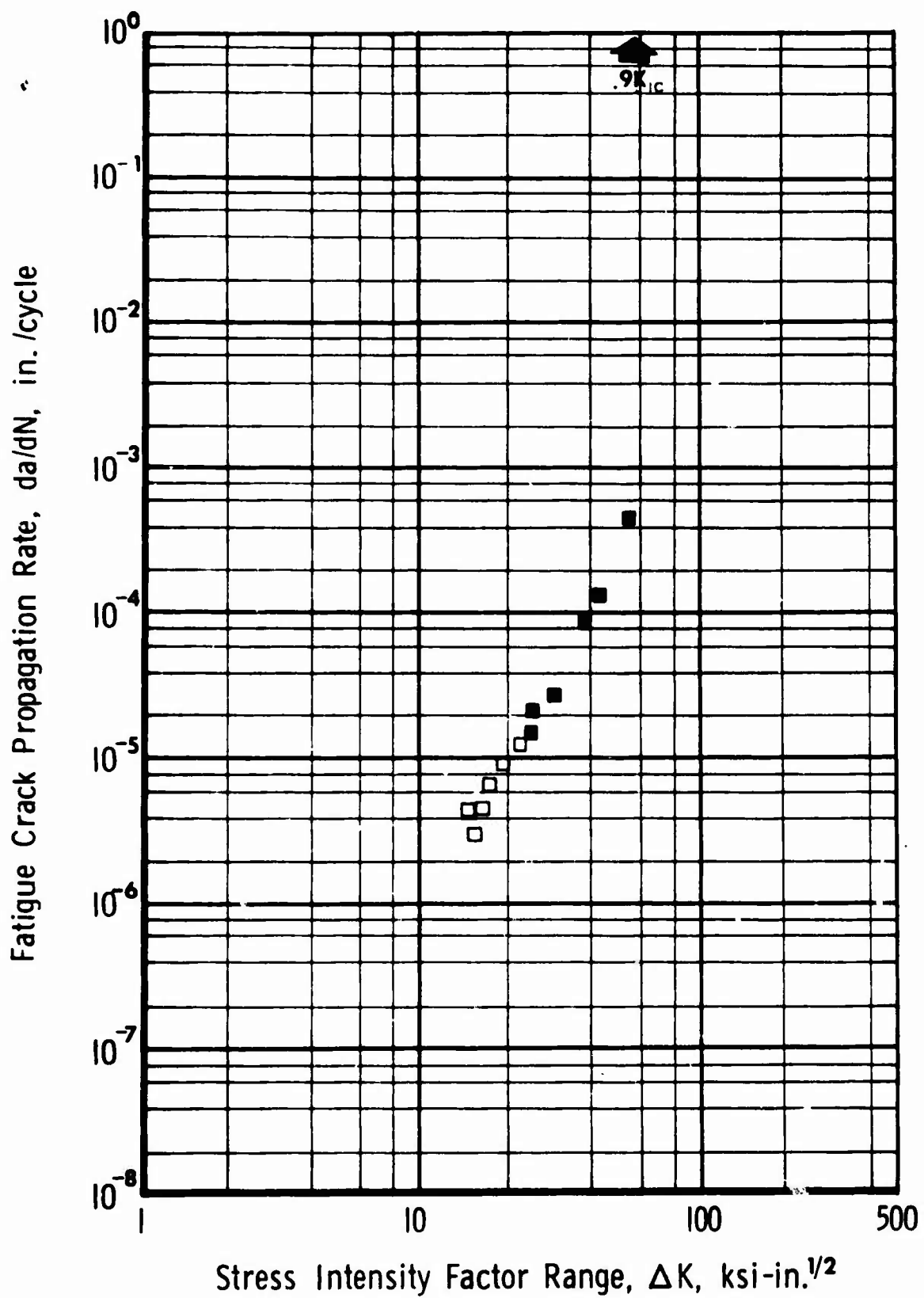
Fig. 61   Ti-6Al-4V Condition 19, 4- x 4-in. forged billet, 1750°F-2 h-AC, 1450°F-1 h-AC.
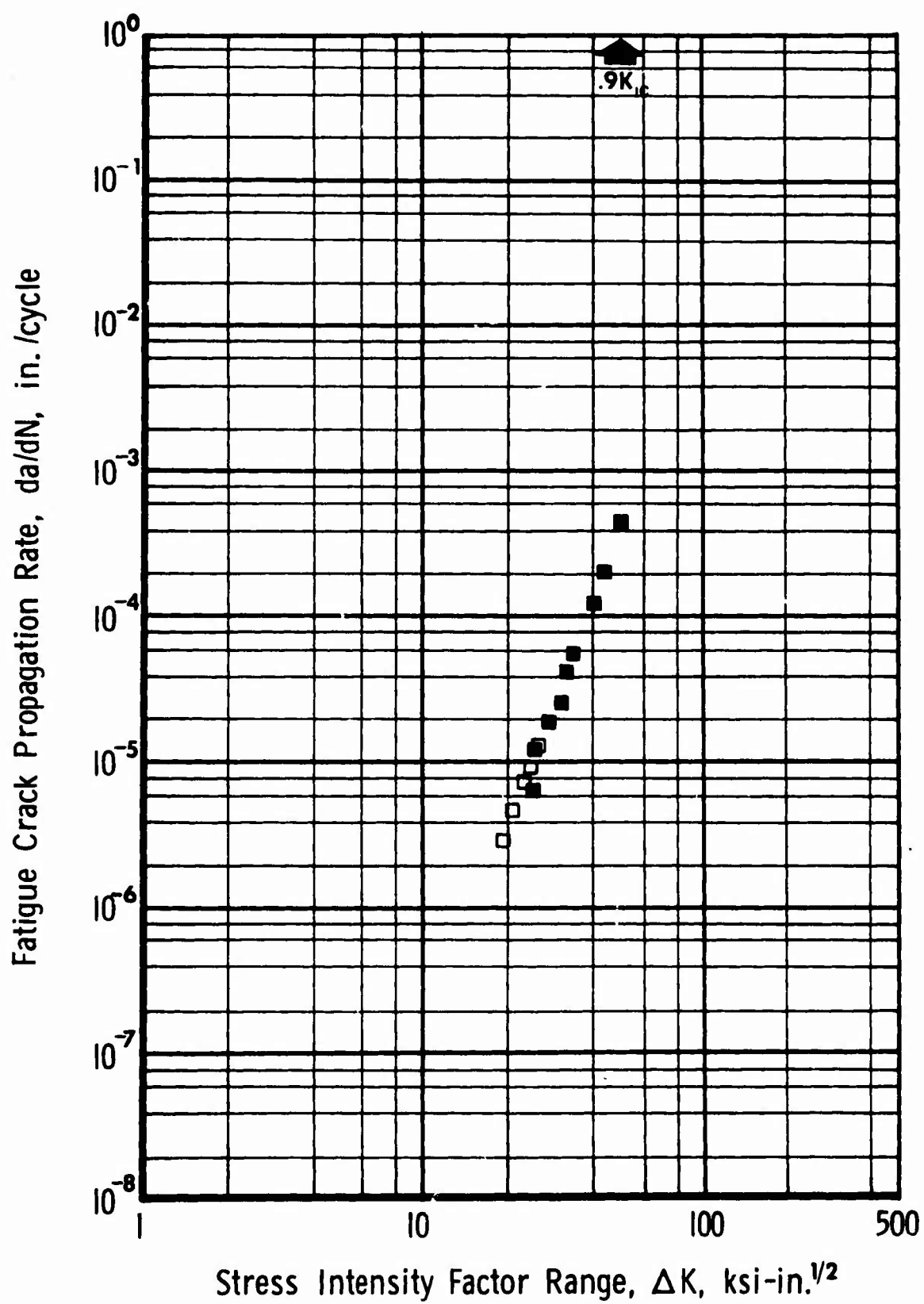
Fig. 62   Ti-6Al-4V Condition 20, 4- x 4-in. forged billet, 1750°F-½ h-WQ, 1000°F-2 h-AC.
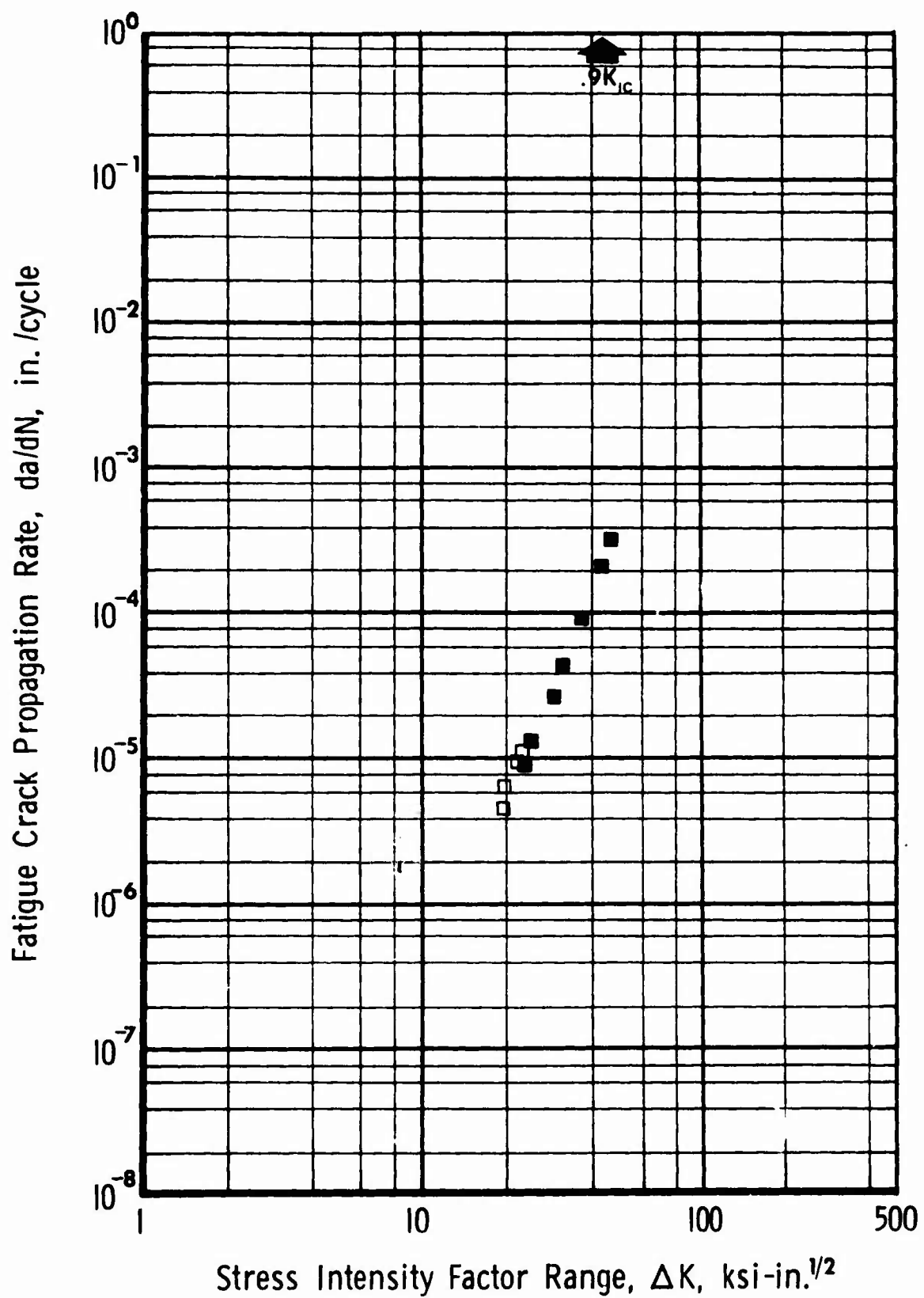
Fig. 63 Ti-6Al-4V Condition 21, 4- x 4-in. forged billet, 1750°F-2 h-WQ, 1000°F-2 h-AC.

98
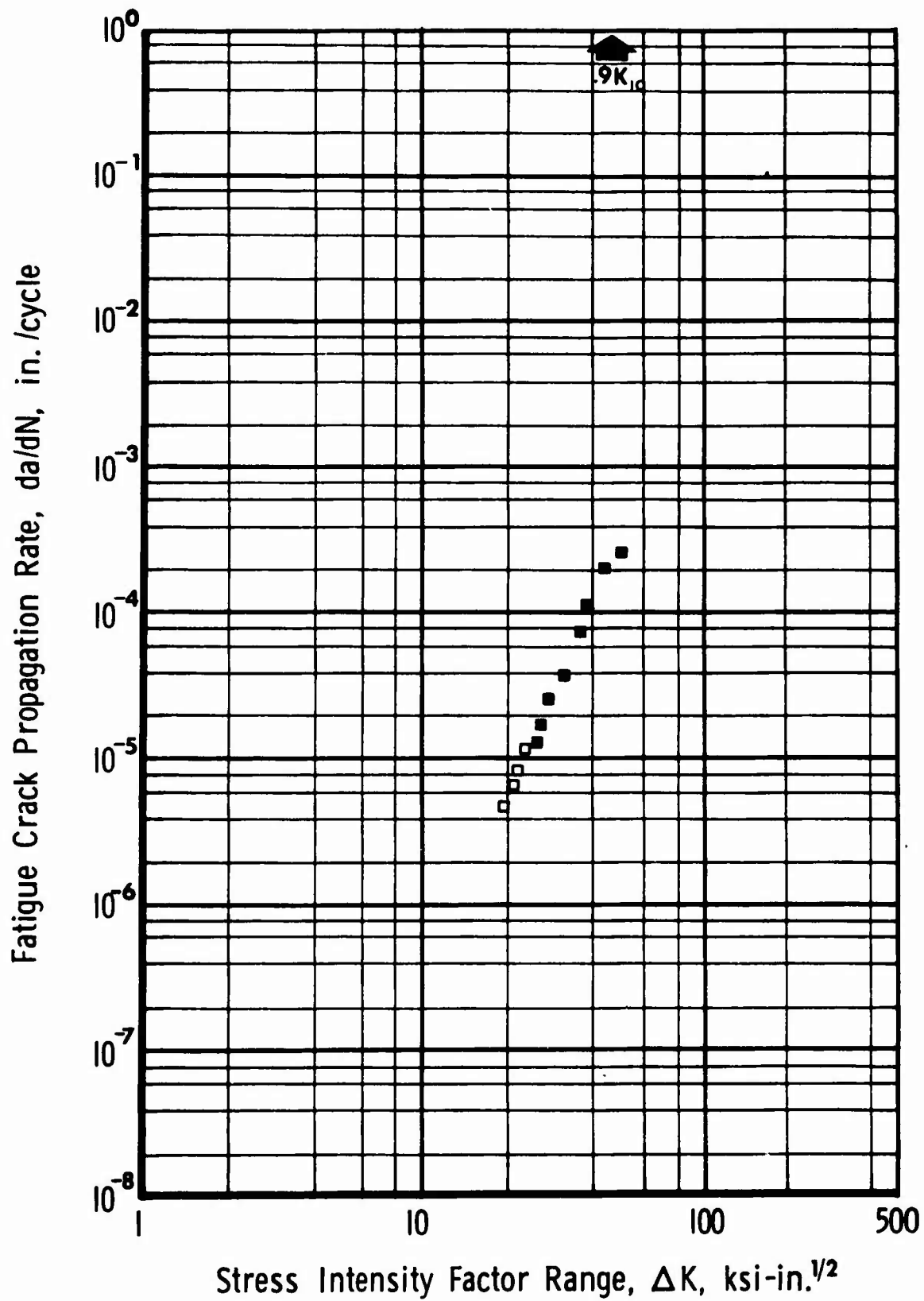
Fig. 64 Ti-6Al-4V Condition 22, 4- x 4-in. forged billet, 1750°F-4 h-WQ, 1000°F-2 h-AC.

99
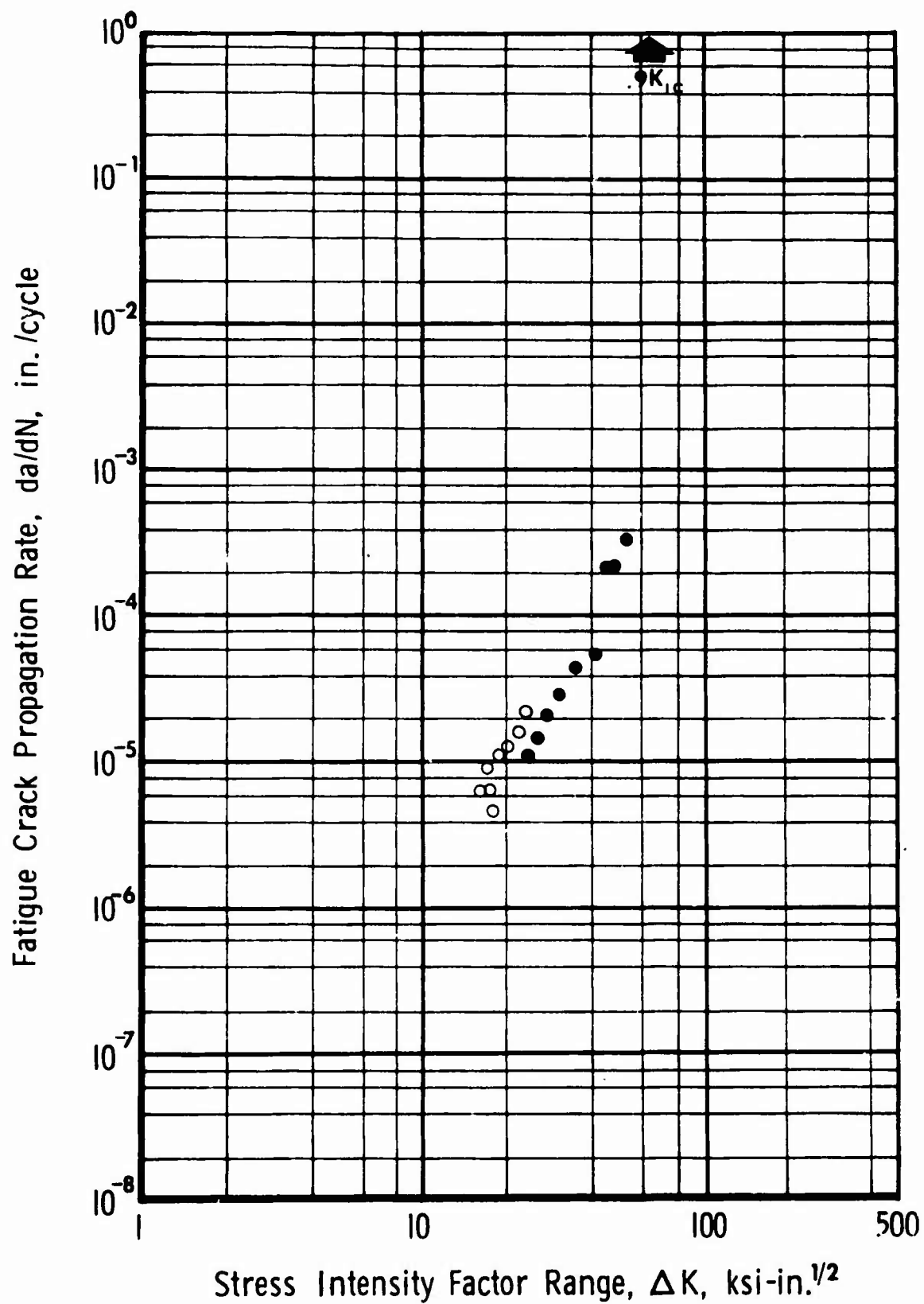
Fig. 65 Ti-6Al-4V Condition 27, 4- x 4-in. forged billet, α-segregated, equiaxed, 1775°F-$\frac{1}{2}$ h-AC, 1450°F-1 h-AC.

100
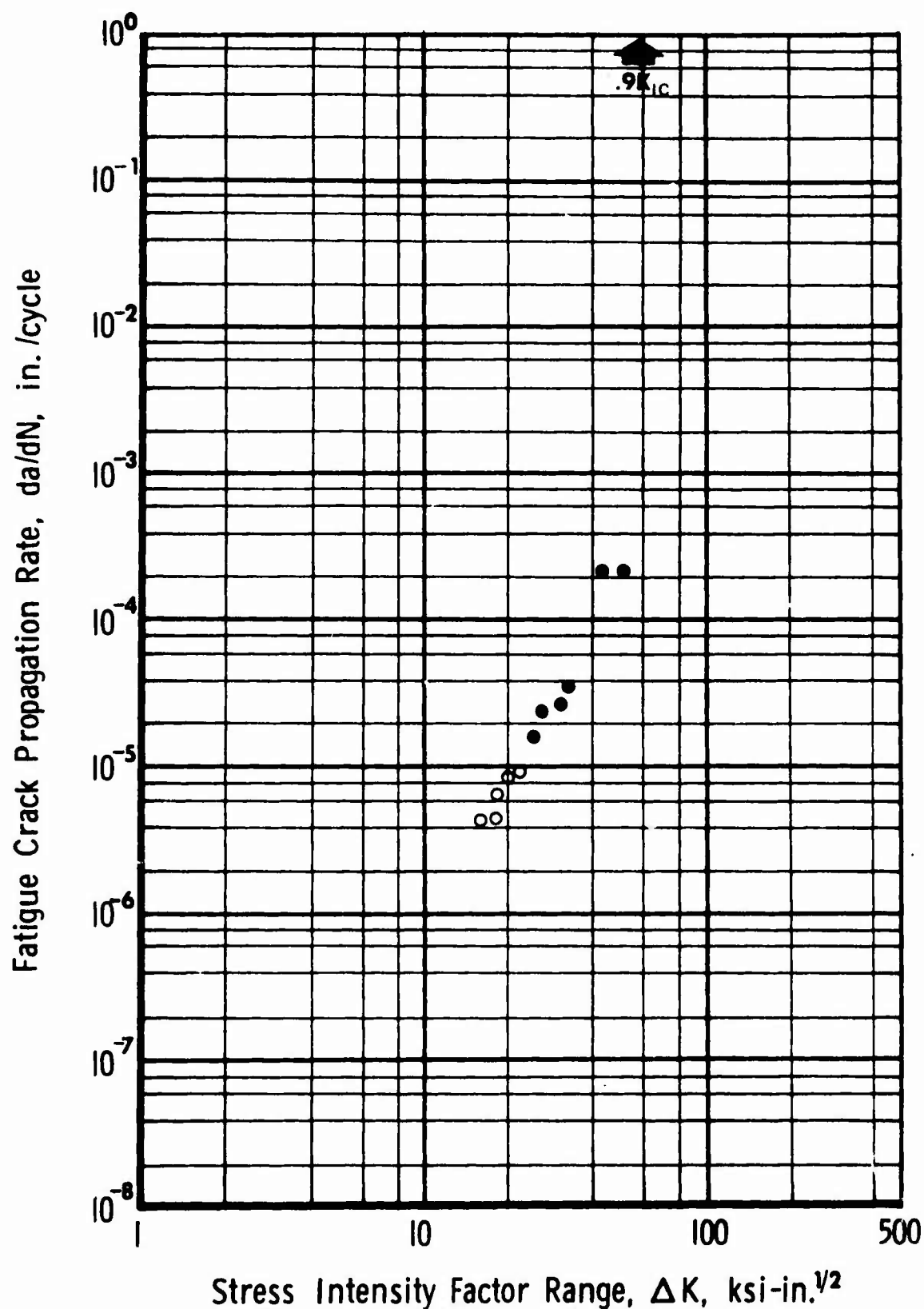
Fig. 66 Ti-6Al-4V Condition 28, 4 x 4-in. forged billet, α-segregated, equiaxed, 1750°F-$\frac{1}{2}$ h-WQ, 1000°F-2 h-AC.
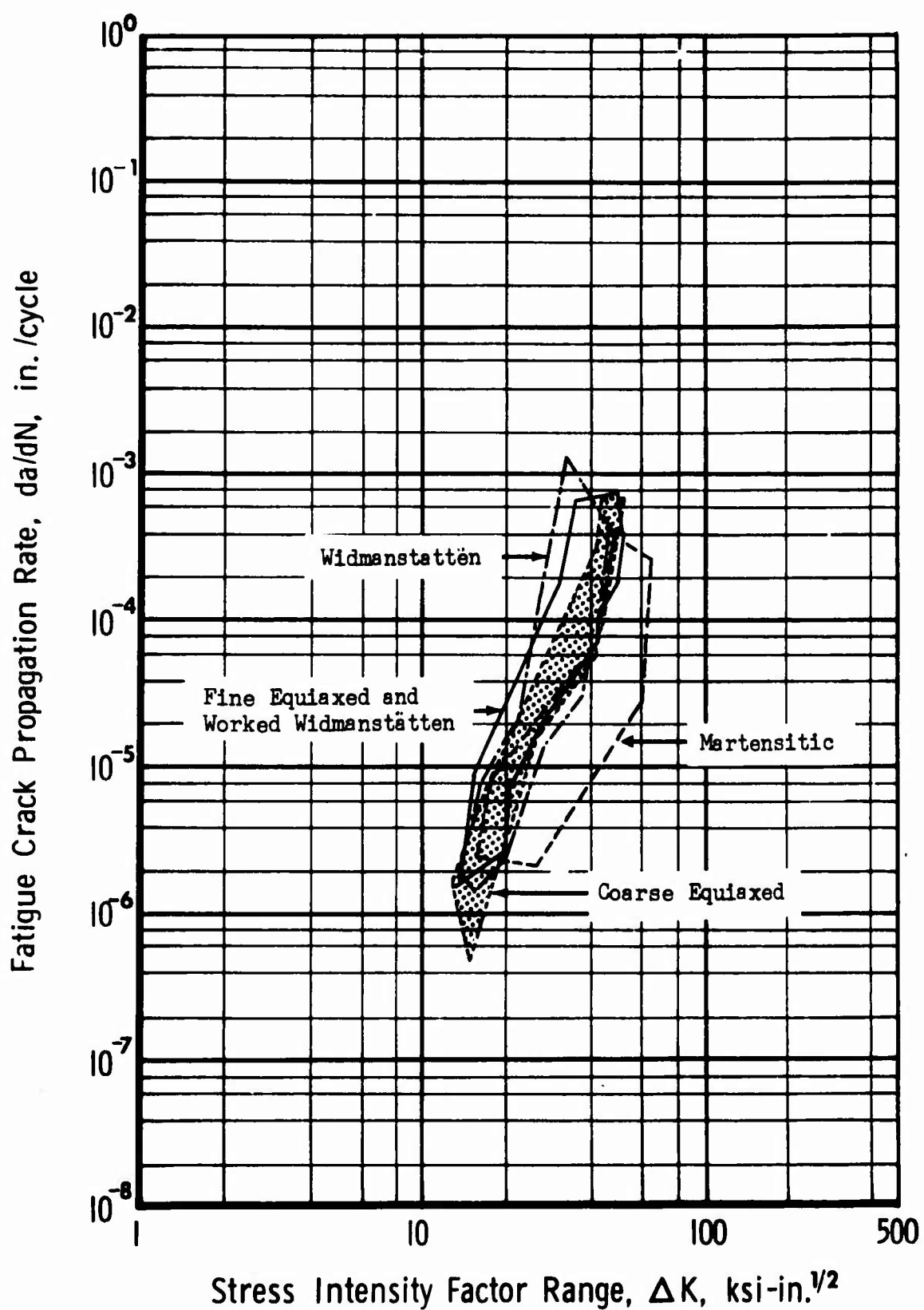
Fig. 67 Comparison of fatigue crack growth rates versus intensity
factor range for different types of Ti-6Al-4V microstructures.
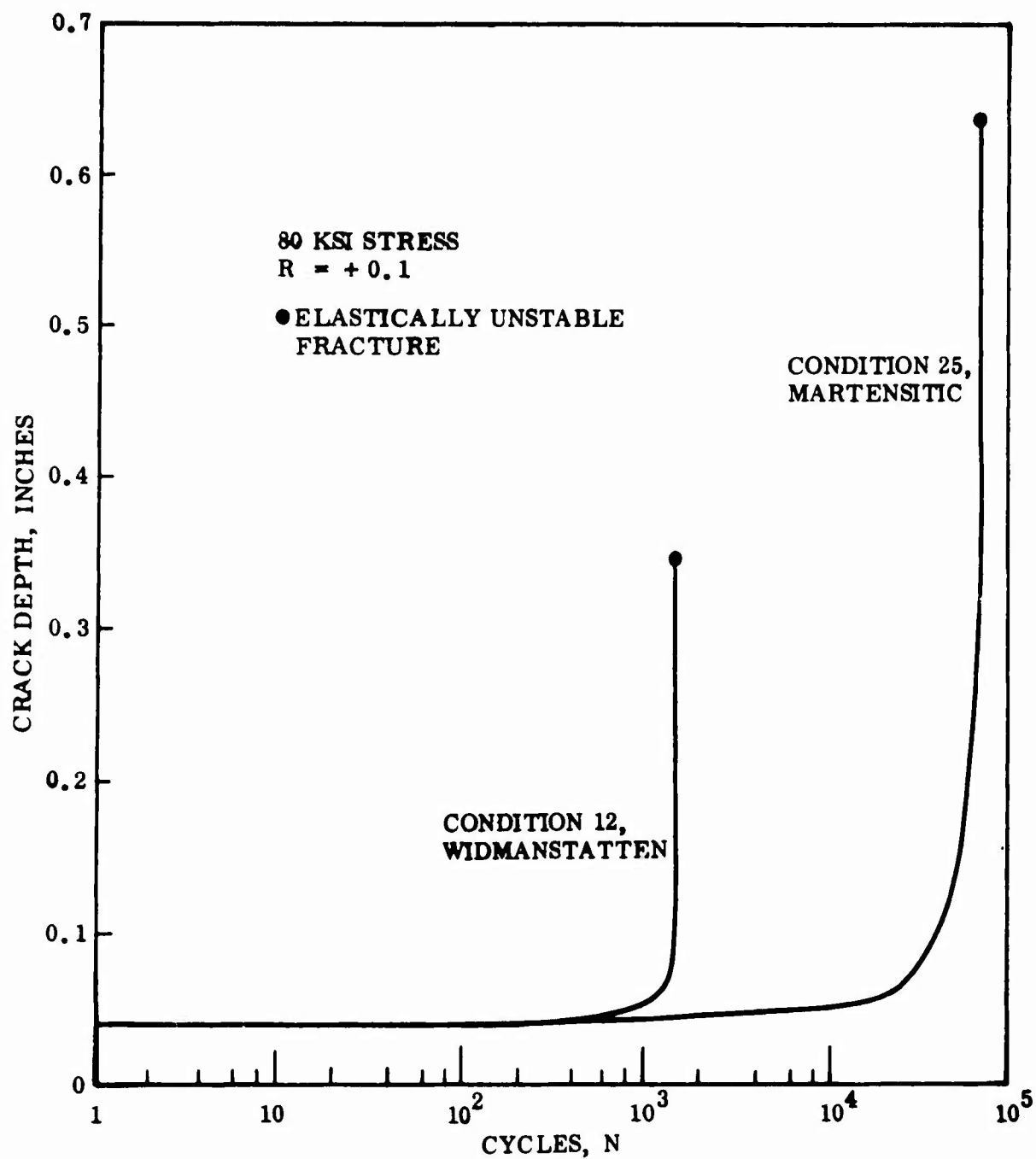
Fig. 68 Comparison of calculated fatigue crack growth for the least and
most fatigue resistant Ti-6Al-4V microstructure conditions. Semi-
circular initial surface flaw assumed, 0.040-in. deep. Sinusoidal
fatigue stress, 80 ksi max, R = +0.1.

3ICX   1400X   3ICW   1350X
            (a) Fatigue   (b) Fast Fracture
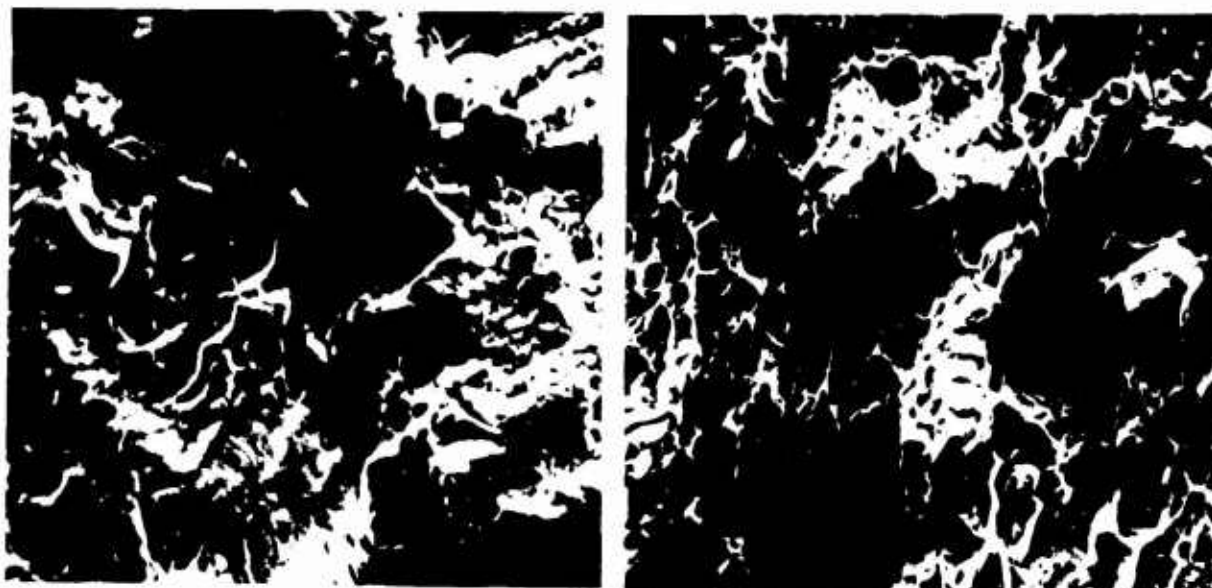
Fig. 69   SEM Fractographs of Ti-6Al-4V Condition 1, 1-in.
           plate, as received (1725°F-1h-AC; 1450°F-1h-AC).
           $K_{Ic} = 47$ ksi-in$^{\frac{1}{2}}$, $F_{ty} = 144$ ksi.

3IDH   1200X   3IDG   1200X
            (a) Fatigue   (b) Fast Fracture

Fig. 70   SEM Fractographs of Ti-6Al-4V Condition 2, 1-in.
           plate, 1775°F-$\frac{1}{2}$h-AC, 1450°F-1h-AC. $K_Q = 111$ ksi-in$^{\frac{1}{2}}$.
           $F_{ty} = 141$ ksi.

104

3ICV   1500X   3ICU   1400X
        (a) Fatigue   (b) Fast Fracture
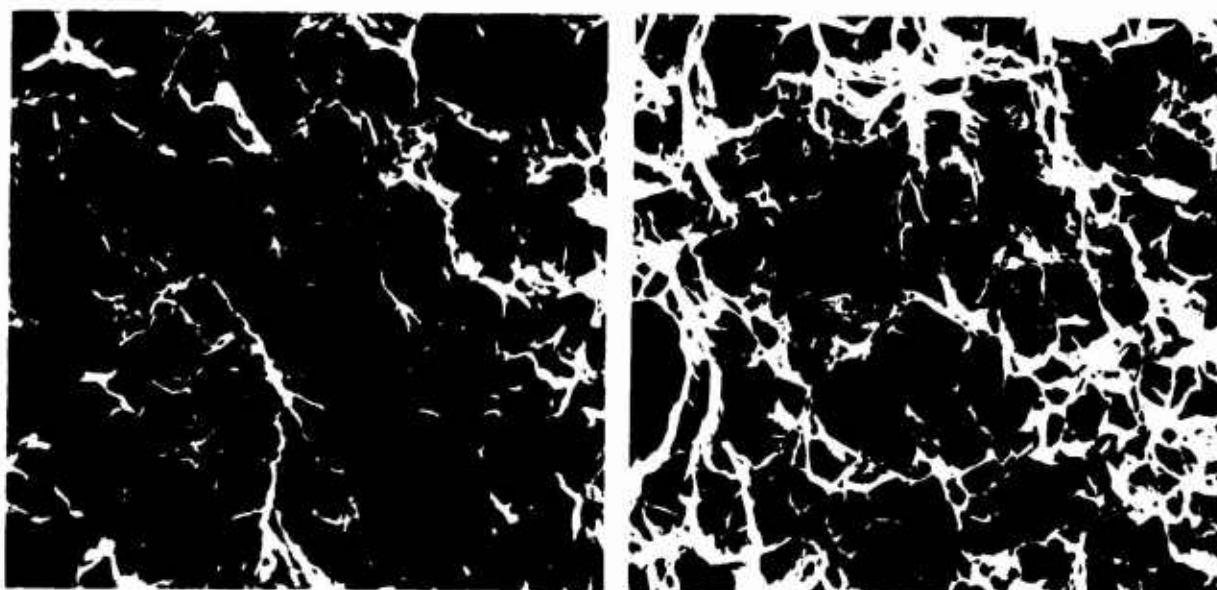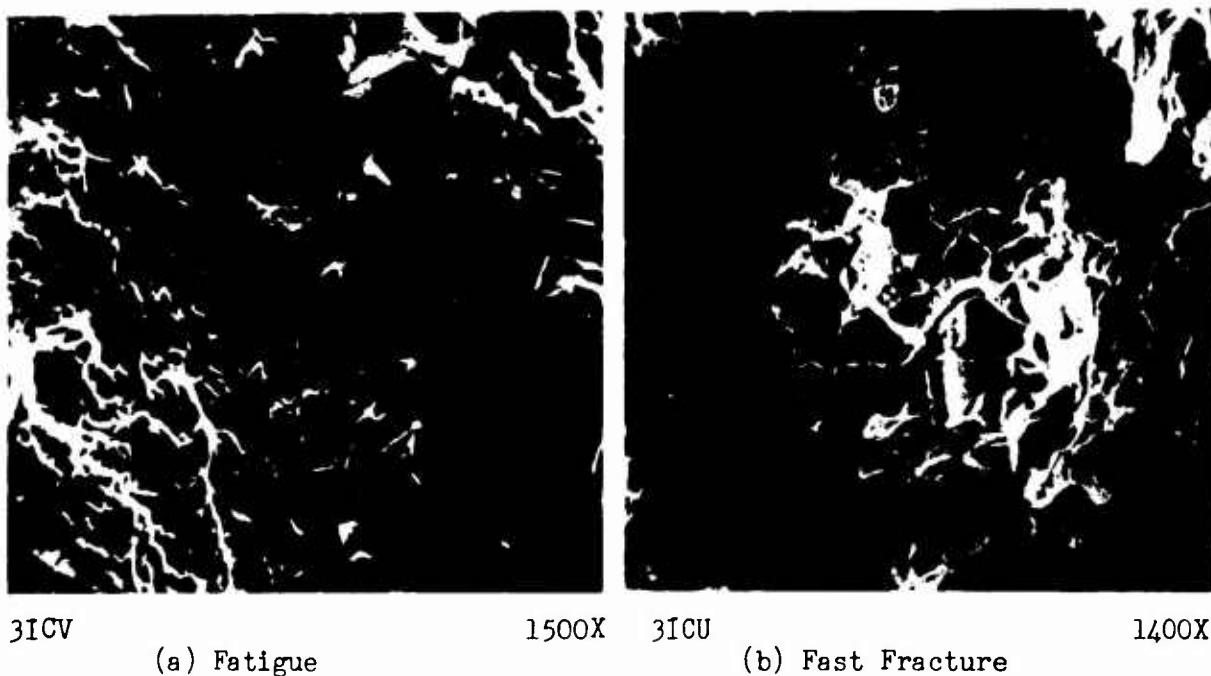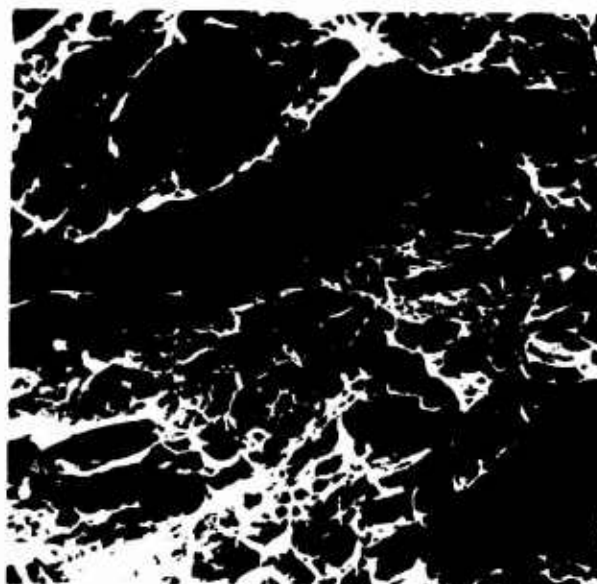
Fig. 71   SEM Fractographs of Ti-6Al-4V Condition 3, 1-in. plate,
           1750°F-1h-AC, 1450°F-1h-AC. K_{Ic} = 62 ksi-in$^{\frac{1}{2}}$, F_{ty} = 143 ksi.

3ICT   1250X   3ICS   1150X
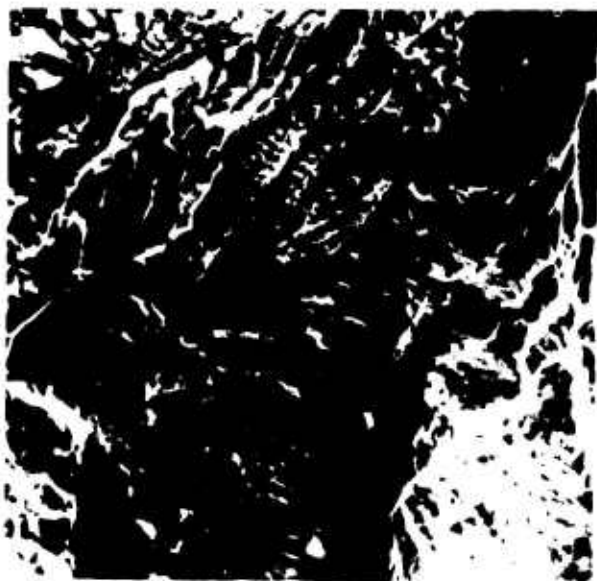   (a) Fatigue   (b) Fast Fracture
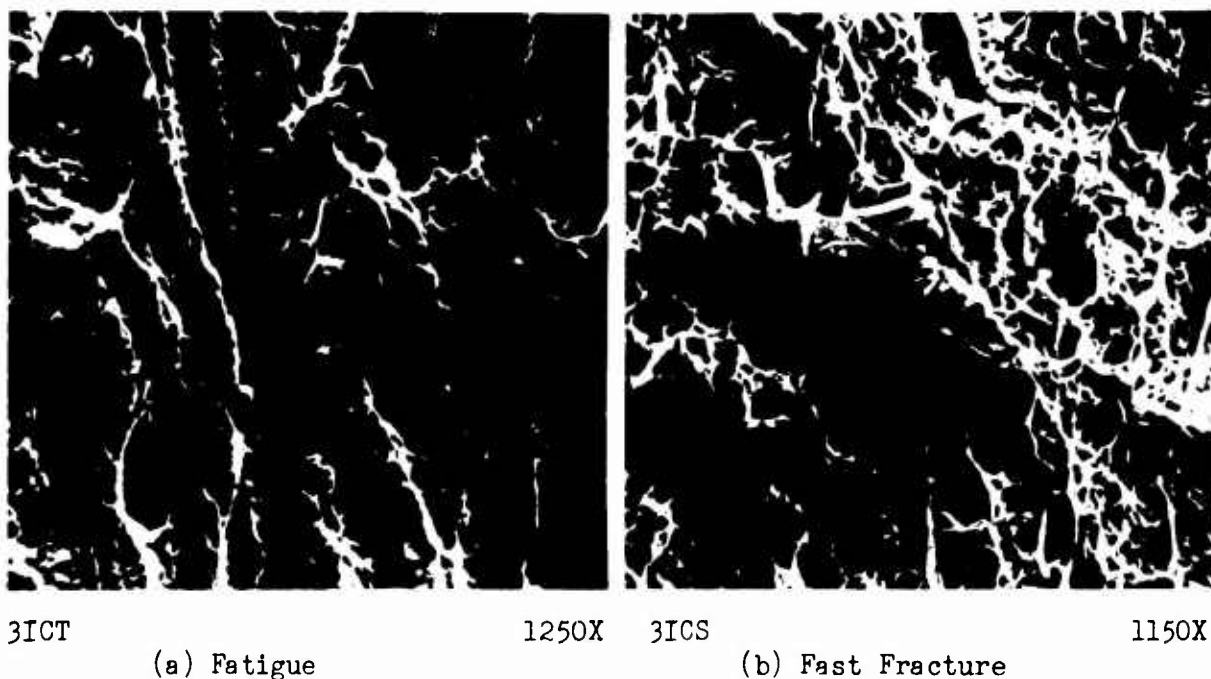
Fig. 72   SEM Fractographs of Ti-6Al-4V Condition 4, 1-in. plate,
           1750°F-½h-WQ, 1000°F-2h-AC. K_{Ic} = 48 ksi-in$^{\frac{1}{2}}$, F_{ty} = 146 ksi.
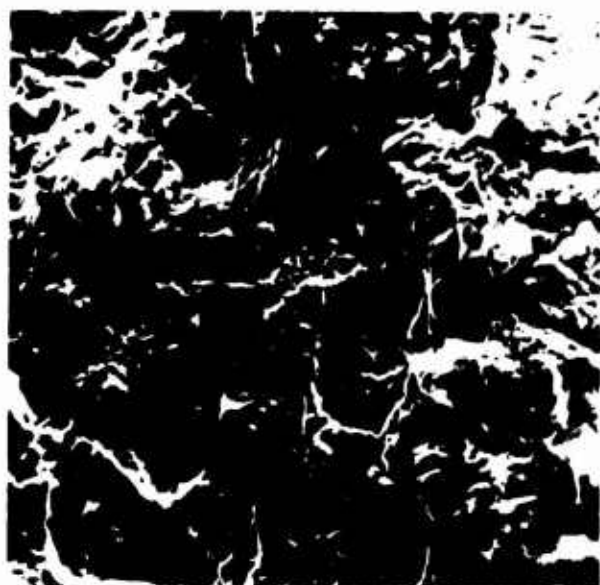
3IDB   1240X   3IDA   1150X
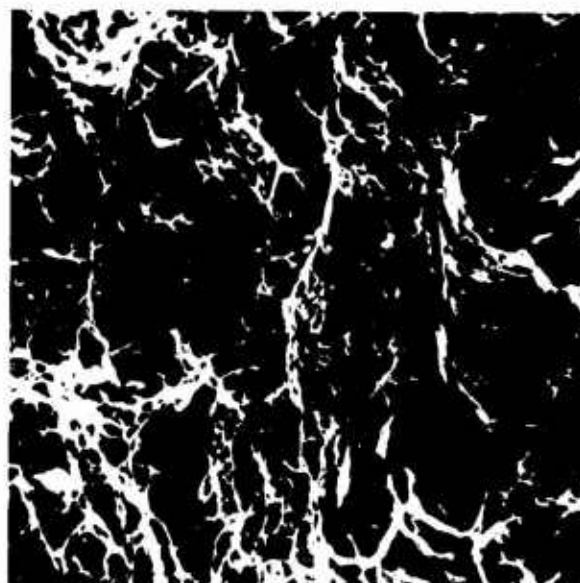
       (a) Fatigue   (b) Fast Fracture

Fig. 73 SEM Fractographs of Ti-6Al-4V Condition 5, 1-in. plate, 1750°F-2h-WQ, 1000°F-2h-AC. K_{Ic} = 51 ksi-in$^{\frac{1}{2}}$, F_{ty} = 160 ksi.
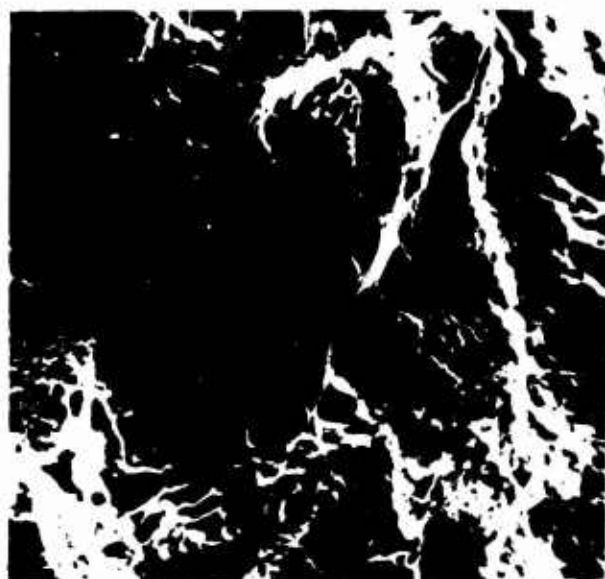
3ICR   1400X   3ICQ   1330X
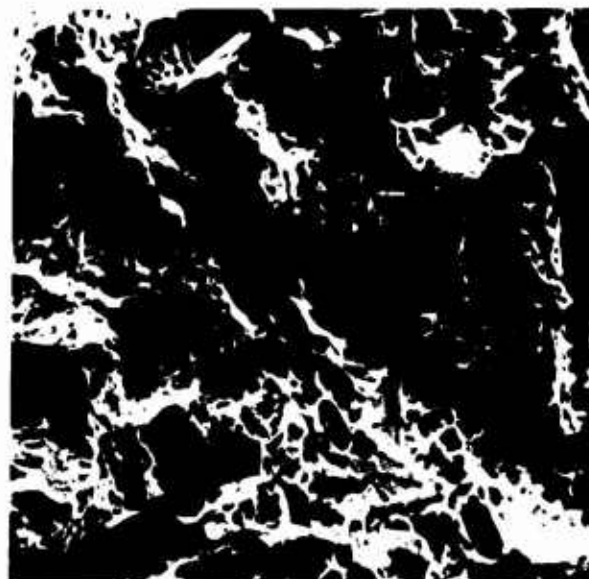
       (a) Fatigue   (b) Fast Fracture

Fig. 74 SEM Fractographs of Ti-6Al-4V Condition 6, 1-in. plate, 1750°F-4h-WQ, 1000°F-2h-AC. K_{Ic} = 49 ksi-in$^{\frac{1}{2}}$, F_{ty} = 164 ksi.

3ICN   1330X   3ICM   1250X
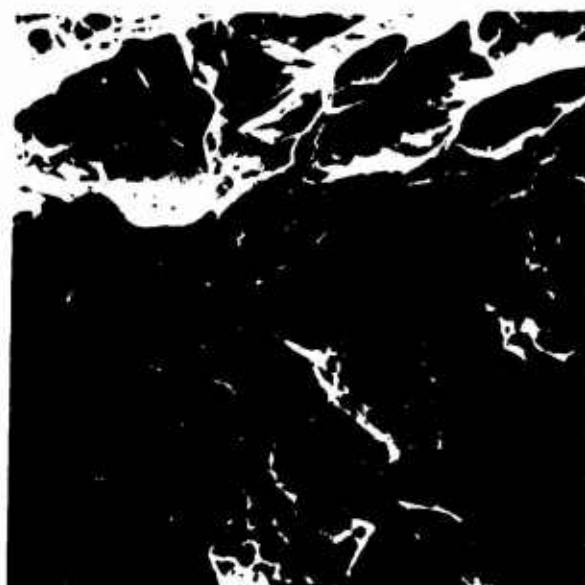
         (a) Fatigue   (b) Fast Fracture

Fig. 75   SEM Fractographs of Ti-6Al-4V Condition 7, 1-in. plate, $1850^\circ F-\frac{1}{2}h-AC$, $1775^\circ F-\frac{1}{2}h-AC$. $1450^\circ F-1h-AC$. $K_Q = 85$ ksi-in$^{\frac{1}{2}}$, $F_{ty} = 124$ ksi.
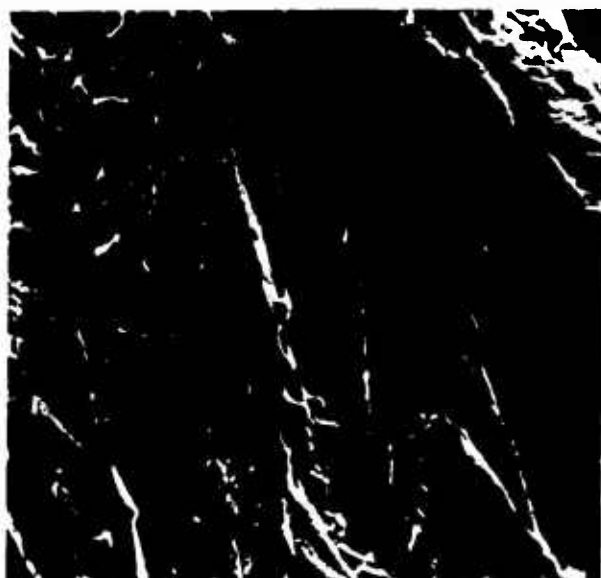
3ICZ   1230X   3ICY   1180X
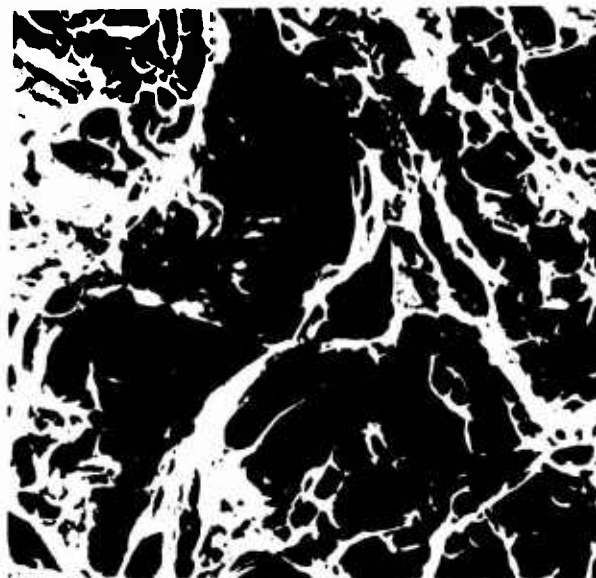
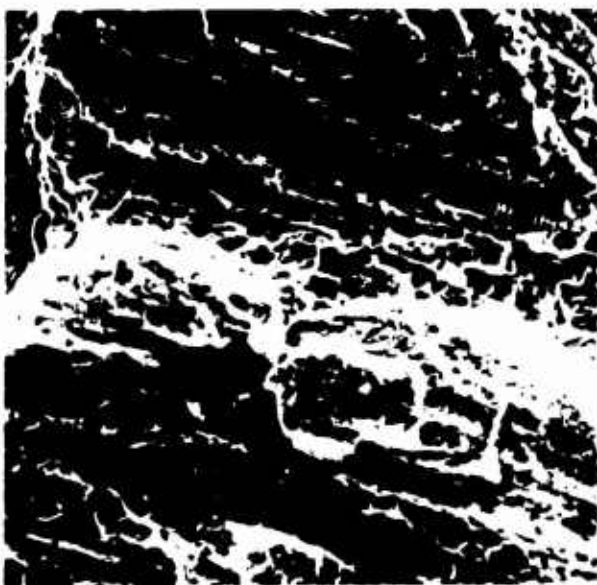   (a) Fatigue   (b) Fast Fracture

Fig. 76   SEM Fractographs of Ti-6Al-4V Condition 8, 1-in. plate, $1850^\circ F-\frac{1}{2}h-AC$, $1750^\circ F-2h-AC$, $1450^\circ F-1h-AC$. $K_Q = 86$ ksi-in$^{\frac{1}{2}}$, $F_{ty} = 127$ ksi.
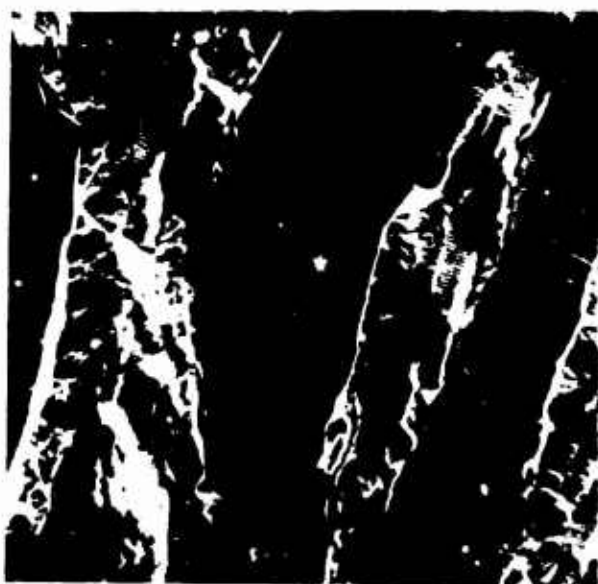
3ICL   1180X   3ICK   1040X
       (a) Fatigue   (b) Fast Fracture

Fig. 77   SEM Fractographs of Ti-6Al-4V, Condition 9, 1-in. plate, $1850^\circ F-\frac{1}{2}h-AC$, $1750^\circ F-4h-AC$, $1450^\circ F-1h-AC$. $K_{Ic} = 82$ ksi-in$^\frac{1}{2}$, $F_{ty} = 127$ ksi.

3ICJ   1270X   3ICI   1150
       (a) Fatigue   (b) Fast Fracture

Fig. 78   SEM Fractographs of Ti-6Al-4V, Condition 10, 1-in. plate, $1850^\circ F-\frac{1}{2}h-AC$, $1750^\circ F-\frac{1}{2}h-WQ$, $1000^\circ F-2h-AC$, $K_{Ic} = 67$ ksi-in$^\frac{1}{2}$, $F_{ty} = 157$ ksi.

3ICH   1270X   3ICG   1160X
              (a) Fatigue   (b) Fast Fracture
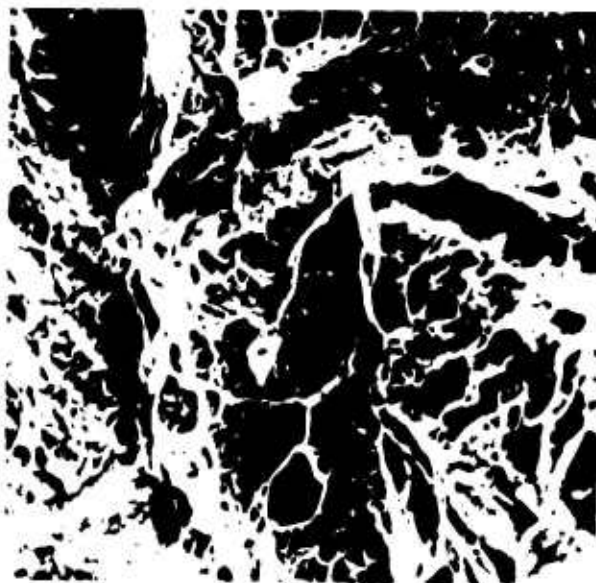
Fig. 79   SEM Fractographs of Ti-6Al-4V, Condition 11, 1-in. plate,
               $1850^{\circ}F-\frac{1}{2}h-AC$, $1750^{\circ}F-2h-WQ$, $1000^{\circ}F-2h-AC$, K_{Ic} = 58 ksi-in$^{\frac{1}{2}}$,
               F_{ty} = 159 ksi.

3ICB   1260X   3ICA   1140X
              (a) Fatigue   (b) Fast Fracture
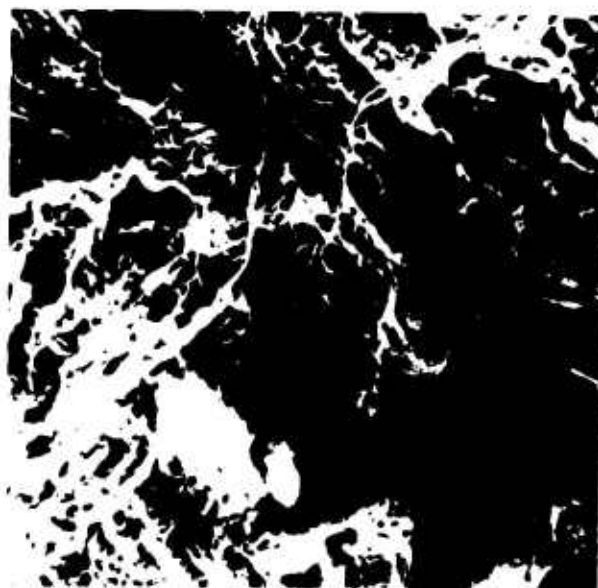
Fig. 80   SEM Fractographs of Ti-6Al-4V, Condition 12, 1-in. plate,
               $1850^{\circ}F-\frac{1}{2}h-AC$, $1750^{\circ}F-4h-WQ$, $1000^{\circ}F-2h-AC$. K_{Ic} = 59 ksi-in$^{\frac{1}{2}}$,
               F_{ty} = 160 ksi.
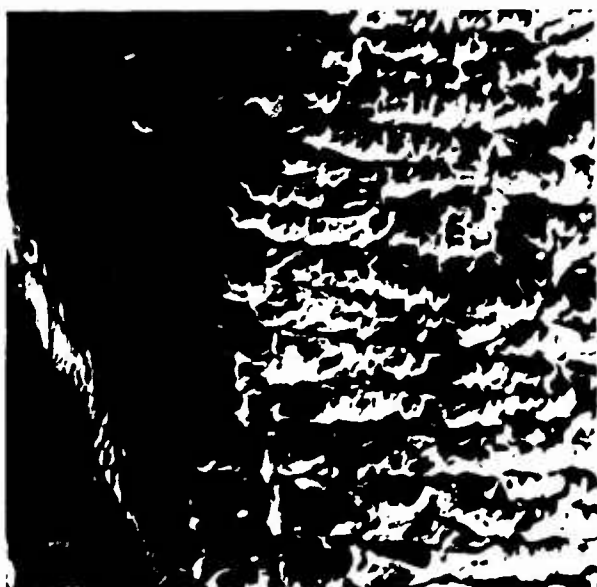
3ICD   1500X   3ICC   1480X
     (a) Fatigue   (b) Fast Fracture
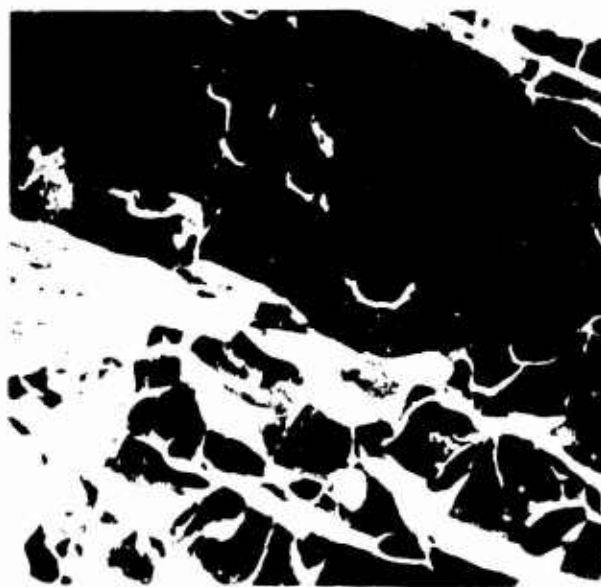
Fig. 81   SEM Fractographs of Ti-6Al-4V, Condition 13, 1-in. plate, $1875°F-\frac{1}{2}h-AC$, $1750°F-2h-AC$, $1450°F-1h-AC$. $K_Q = 87$ ksi-in$^{\frac{1}{2}}$, $F_{ty} = 125$ ksi.

3ICF   1160X   3ICE   1020X
     (a) Fatigue   (b) Fast Fracture
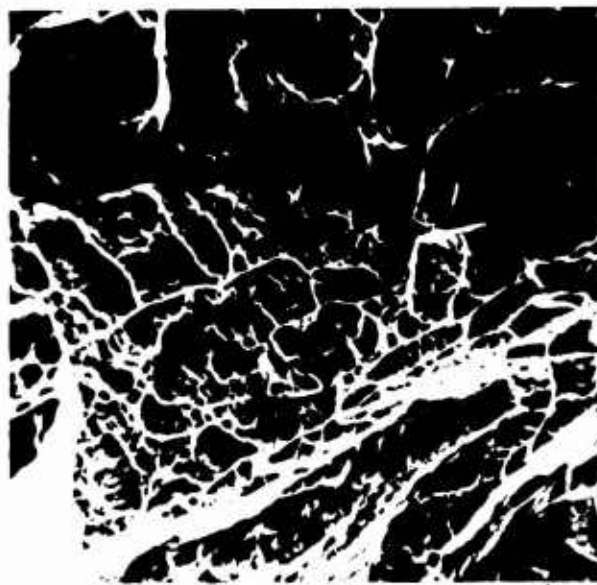
Fig. 82   SEM Fractographs of Ti-6Al-4V, Condition 14, 1-in. plate, $1875°F-\frac{1}{2}h-AC$, $1750°F-2h-WQ$, $1000°F-2h-AC$. $K_{Ic} = 71$ ksi-in$^{\frac{1}{2}}$, $F_{ty} = 156$ ksi.

110

3IEC   1380X   3IEB   1330X
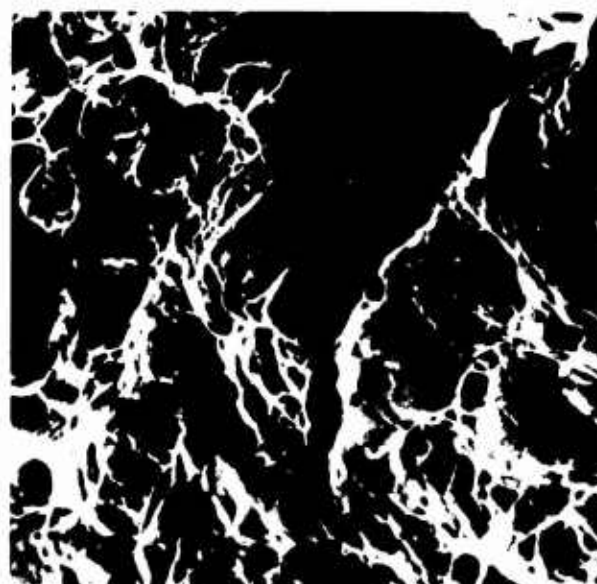
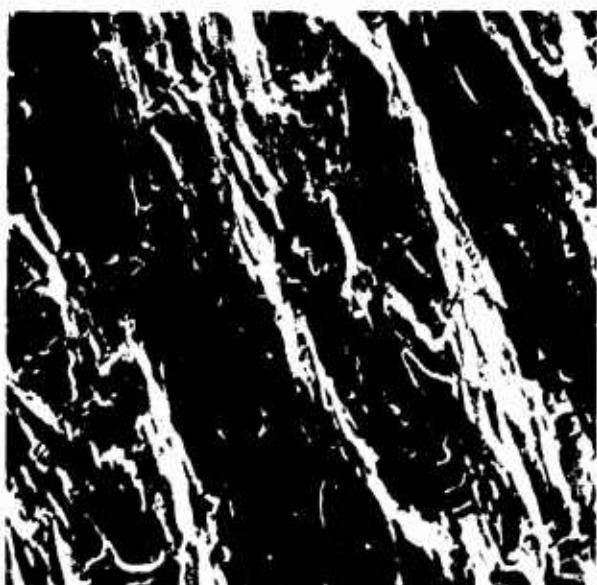   (a) Fatigue   (b) Fast Fracture

Fig. 83   SEM Fractographs of Ti-6Al-4V, Condition 23, 1-in. plate, 1850°F-$\frac{1}{2}$h-IBQ. K_{Ic} = 78 ksi-in$^{\frac{1}{2}}$, F_{ty} = 148 ksi.
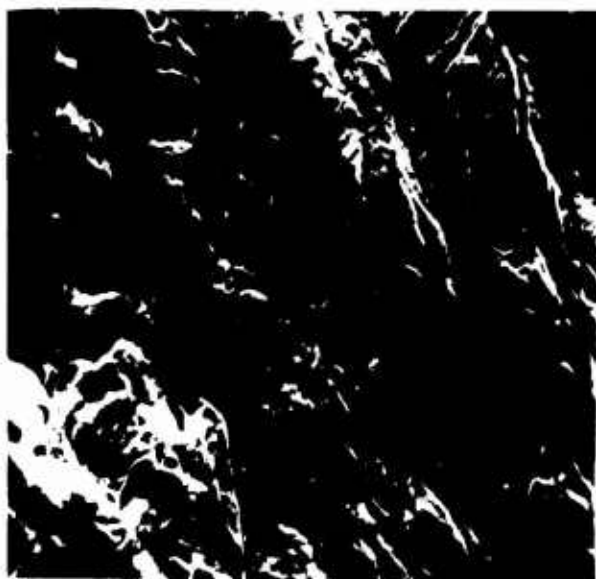
3IDM   1440X   3IDL   1380X

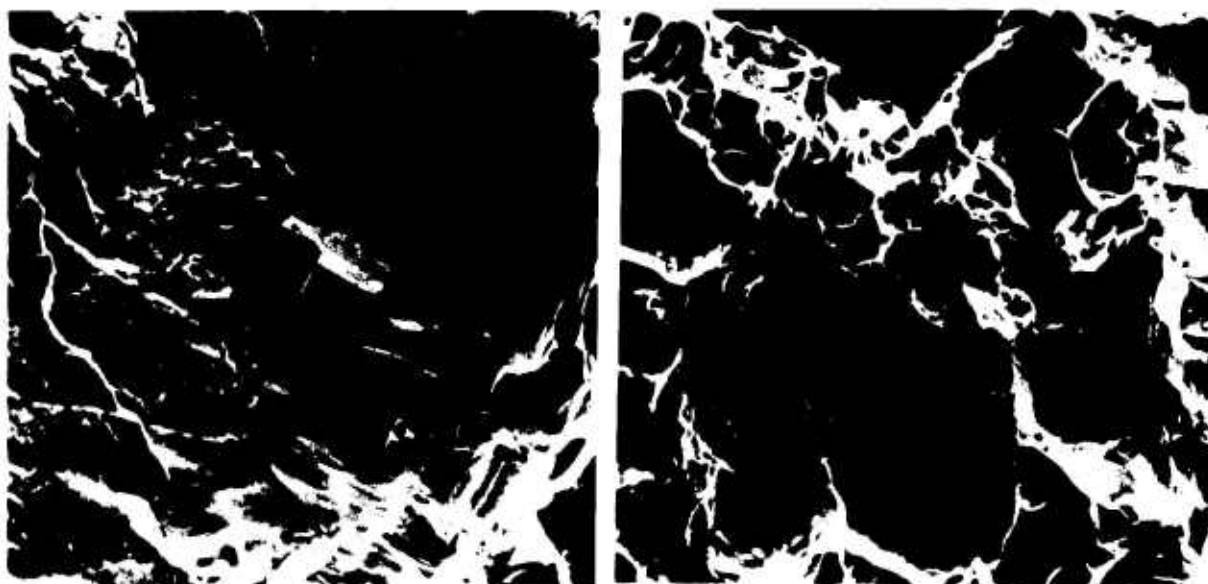   (a) Fatigue   (b) Fast Fracture

Fig. 84   SEM Fractographs of Ti-6Al-4V, Condition 24, 1-in. plate, 1850°F-$\frac{1}{2}$h-IBQ, 1450°F-1h-AC. K_{Ic} = 61 ksi-in$^{\frac{1}{2}}$, F_{ty} = 150 ksi.

111
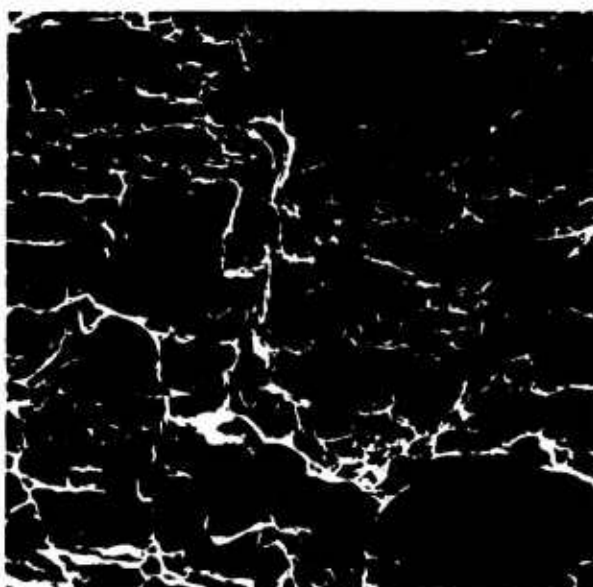
3IDT   1140X   3IDR   1000X
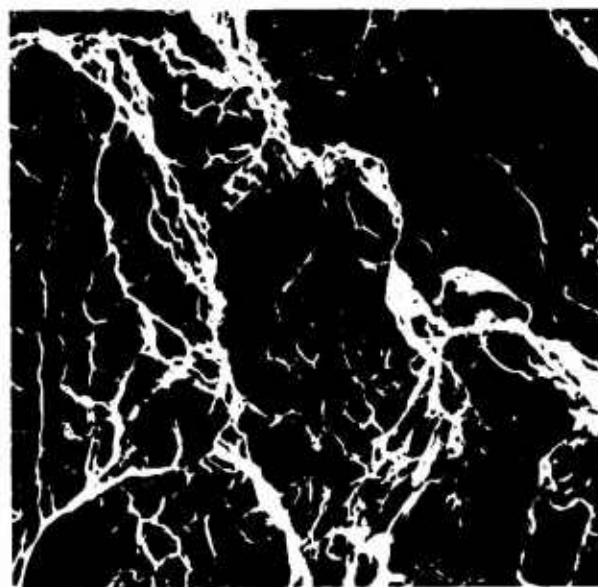
       (a) Fatigue   (b) Fast Fracture

Fig. 85   SEM Fractographs of Ti-6Al-4V, Condition 25, 1-in. plate, 1875°F-$\frac{1}{2}$h-IBQ. K_{Ic} = 80 ksi-in$^{\frac{1}{2}}$, F_{ty} = 136 ksi.

3IDD   1200X   3IDC   1080X
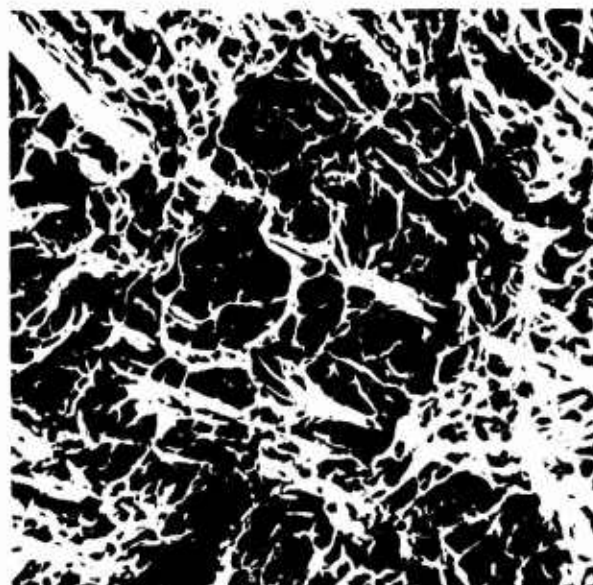
       (a) Fatigue   (b) Fast Fracture

Fig. 86   SEM Fractographs of Ti-6Al-4V, Condition 26, 1-in. plate, 1875°F-$\frac{1}{2}$h-IBQ, 1450°F-1h-AC. K_{Ic} = 66 ksi-in$^{\frac{1}{2}}$, F_{ty} = 153 ksi.

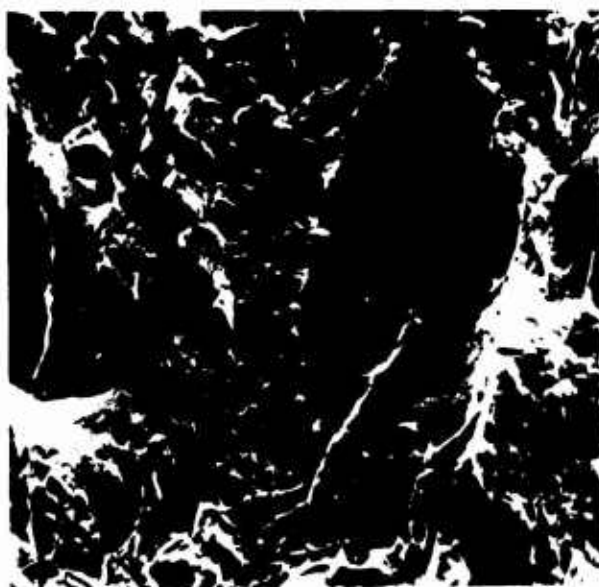3IDY   1360X   3IDX   1280X
          (a) Fatigue   (b) Fast Fracture

Fig. 87   SEM Fractographs of Ti-6Al-4V, Condition 15, 2.4-in. plate,
               as-received. K_{Ic} = 48 ksi-in$^{\frac{1}{2}}$, F_{ty} = 121 ksi.
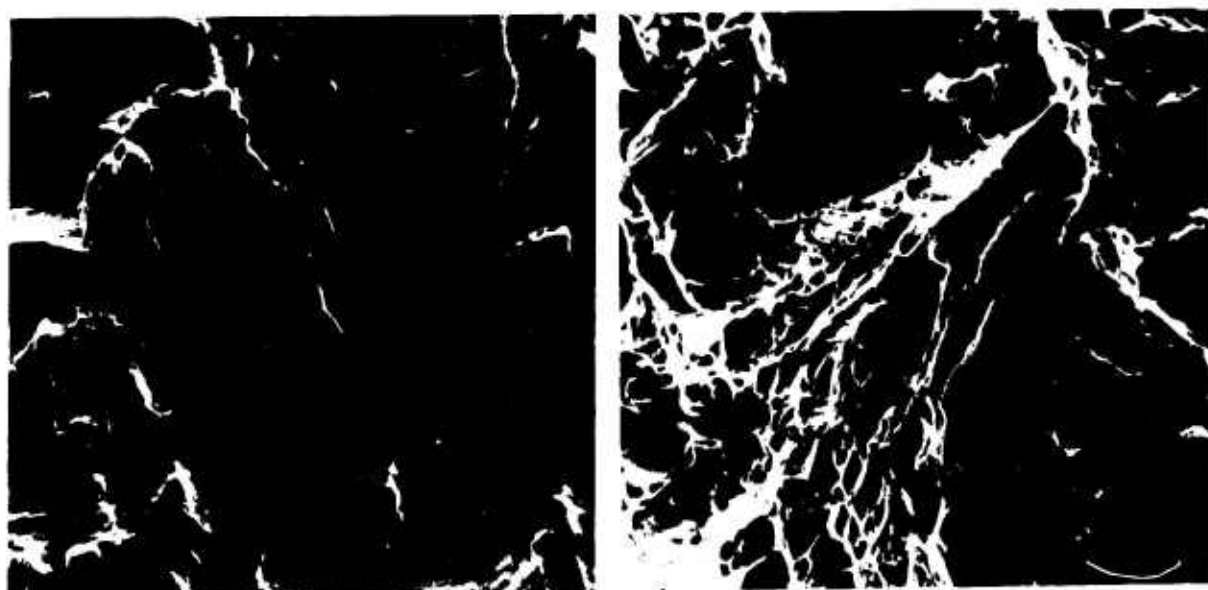
3IDV   1220X   3IDU   1120X
          (a) Fatigue   (b) Fast Fracture

Fig. 88   SEM Fractographs of Ti-6Al-4V, Condition 16, 2.4-in. plate,
               1775°F-$\frac{1}{2}$h-AC, 1450°F-1h-AC. K_{Ic} = 80 ksi, F_{ty} = 134 ksi.

113

3IEE 1160X 3IED 1040X
(a) Fatigue (b) Fast Fracture
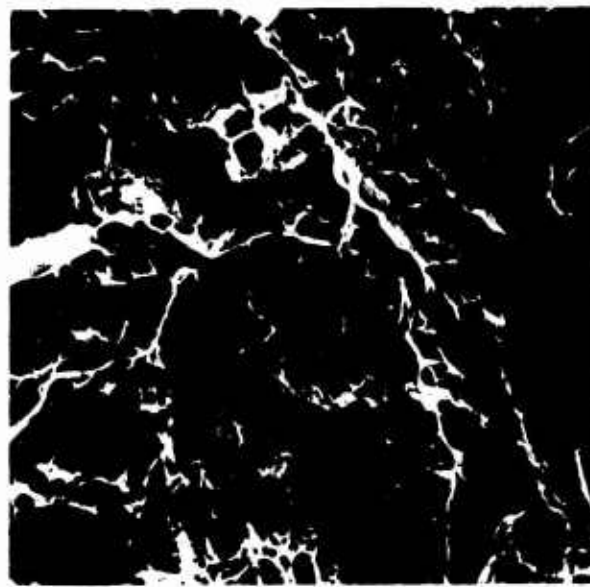
Fig. 89 SEM Fractographs of Ti-6Al-4V, Condition 17, 4- x 4-in., forged billet, $1775^{\circ}F-\frac{1}{2}h$-AC, $1450^{\circ}F$-1h-AC. K_{Ic} = 67 ksi-in$^{\frac{1}{2}}$, F_{ty} = 123 ksi.
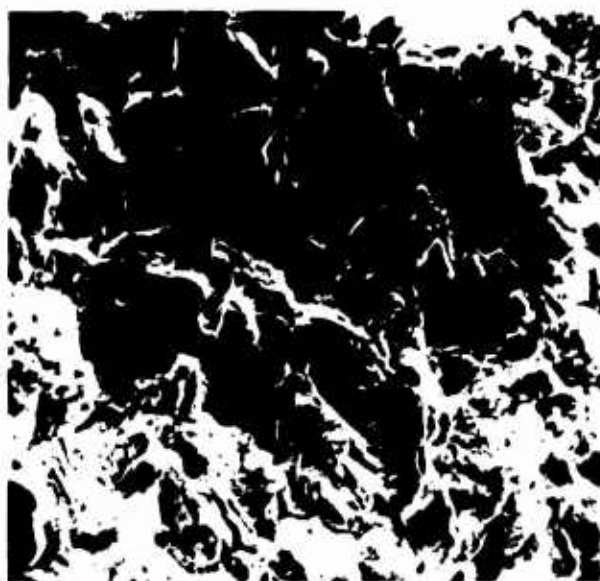
3IEG 1130X 3IEF 1070X
(a) Fatigue (b) Fast Fracture
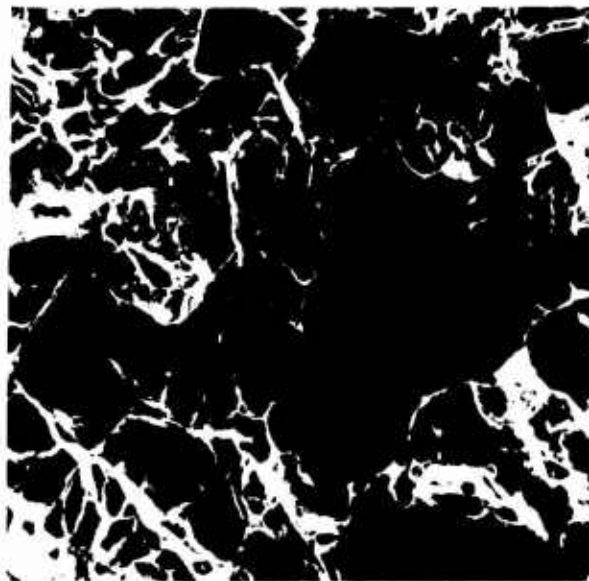
Fig. 90 SEM Fractographs of Ti-6Al-4V, Condition 18, 4- x 4-in. forged billet, $1750^{\circ}F$-2h-AC, $1450^{\circ}F$-1h-AC. K_{Ic} = 68 ksi-in$^{\frac{1}{2}}$, F_{ty} = 125 ksi.

114

3IDJ   1380X   3IDI   1320X
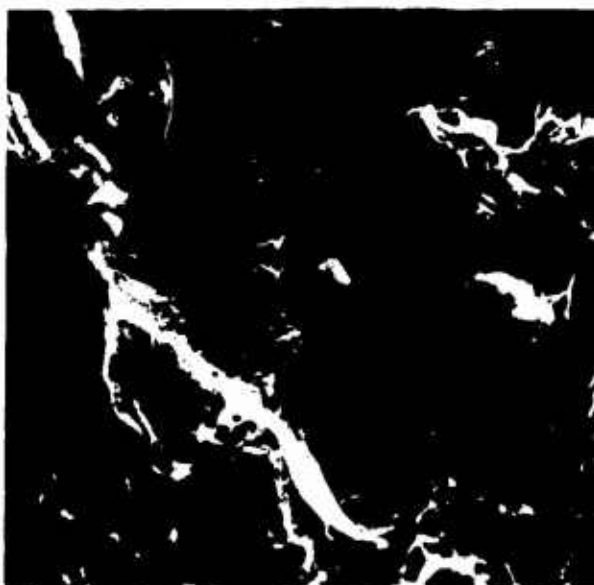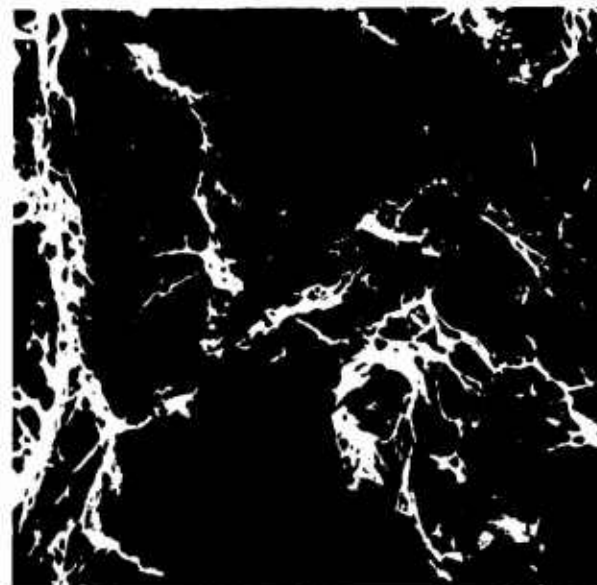   (a) Fatigue   (b) Fast Fracture

Fig. 91   SEM Fractographs of Ti-6Al-4V, Condition 19, 4- x 4-in. forged billet, 1750°F-4h-AC, 1450°F-1h-AC. K_{Ic} = 65 ksi-in$^{\frac{1}{2}}$, F_{ty} = 127 ksi.

3IEJ   1340X   3IEI   1280X
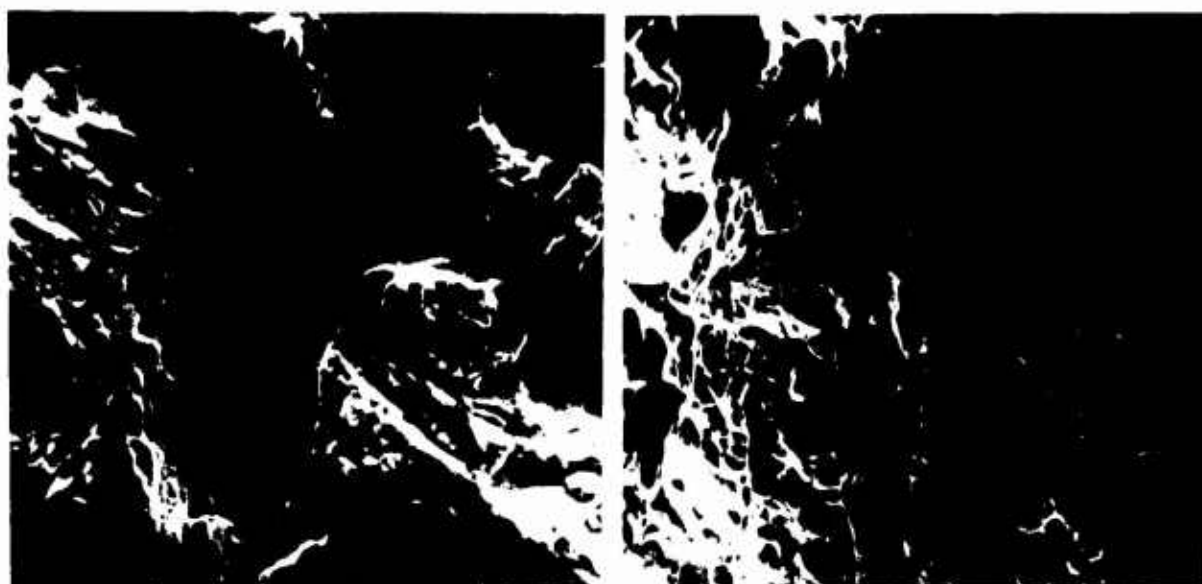   (a) Fatigue   (b) Fast Fracture

Fig. 92   SEM Fractographs of Ti-6Al-4V, Condition 20, 4- x 4-in. forged billet, 1750°F-$\frac{1}{2}$h-WQ, 1000°F-2h-AC. K_{Ic} = 56 ksi-in$^{\frac{1}{2}}$, F_{ty} = 144 ksi.

115

3IEA   1420X   3IDZ   1400X
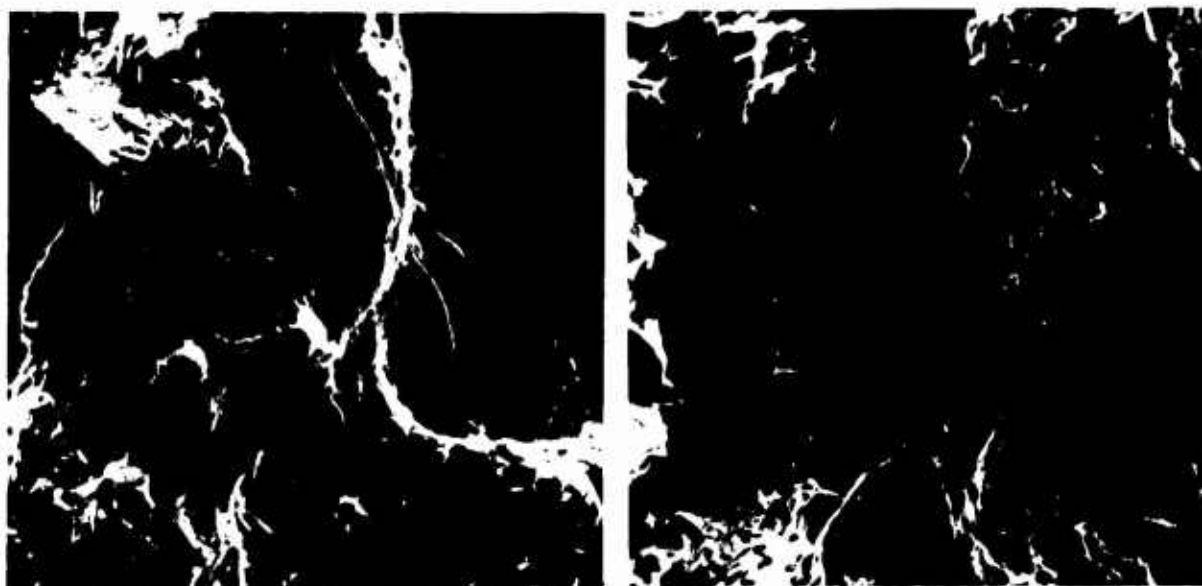   (a) Fatigue   (b) Fast Fracture

Fig. 93   SEM Fractographs of Ti-6Al-4V, Condition 21, 4- x 4-in. forged billet, 1750°F-2h-WQ, 1000°F-2h-AC. K_{Ic} = 51 ksi-in$^{\frac{1}{2}}$, F_{ty} = 147 ksi.

3IDQ   1360X   3IDP   1310X
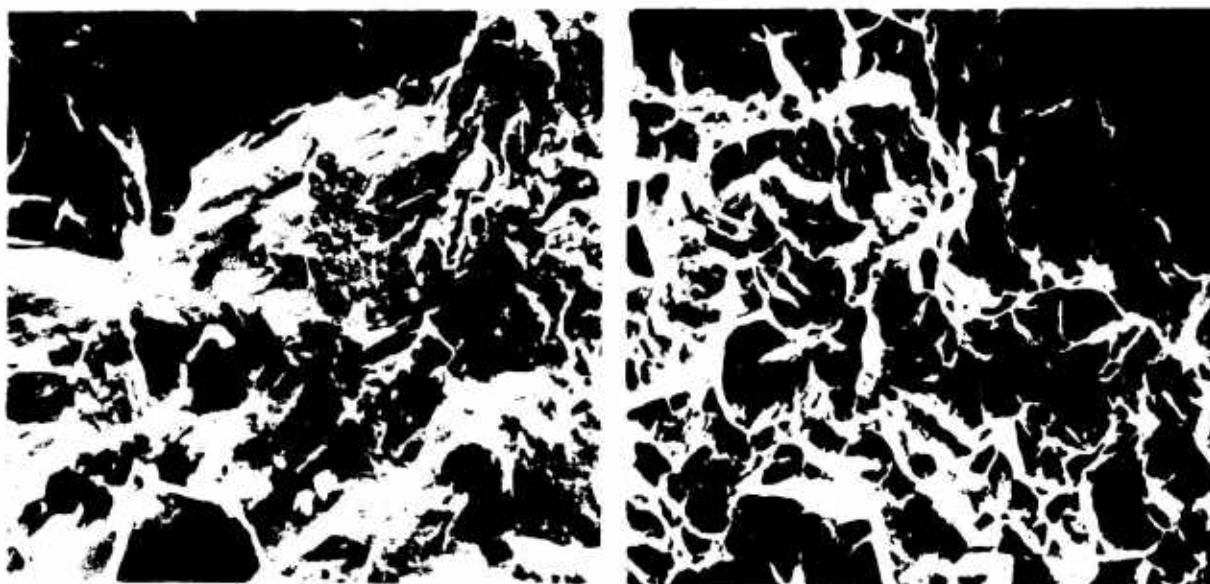   (a) Fatigue   (b) Fast Fracture

Fig. 94   SEM Fractographs of Ti-6Al-4V, Condition 22, 4- x 4-in. forged billet, 1750°F-4h-WQ, 1000°F-2h-AC. K_{Ic} = 53 ksi-in$^{\frac{1}{2}}$, F_{ty} = 144 ksi.

116

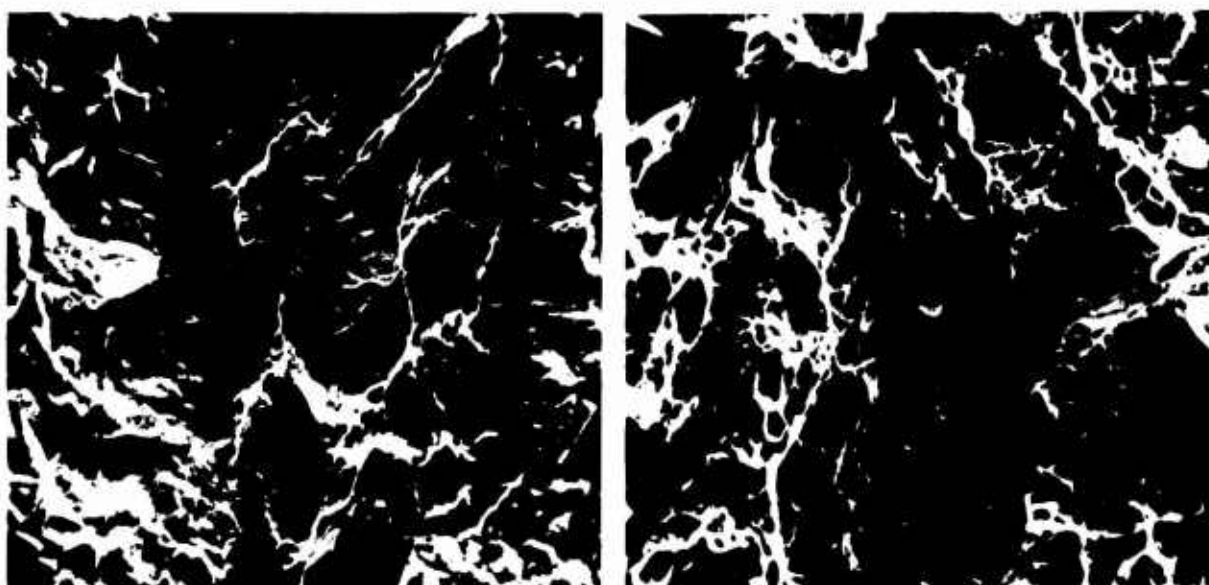3IDF   1400X   3IDE   1350X

            (a) Fatigue   (b) Fast Fracture

Fig. 95   SEM Fractographs of Ti-6Al-4V, Condition 27, 4- x 4-in. forged billet, α -segregated, equiaxed, 1775°F-½h-AC, 1450°-1h-AC. K_{Ic} = 72 ksi-in$^{\frac{1}{2}}$, F_{ty} = 130 ksi.

3IDO   1400X   3IDN   1300X

            (a) Fatigue   (b) Fast Fracture

Fig. 96   SEM Fractographs of Ti-6Al-4V, Condition 28, 4- x 4-in. forged billet, α -segregated, equiaxed, 1750°F-½h-WQ, 1000°F-2h-AC. K_{Ic} = 66 ksi-in$^{\frac{1}{2}}$, F_{ty} = 138 ksi.